Assessing the Compact Polarimetric Capabilities of the RADARSAT Constellation Mission for Monitoring Sub-Arctic Lake Ice Dynamics

by

Saba Dezyani

A thesis

presented to the University of Waterloo

in fulfillment of the

thesis requirement for the degree of

Master of Science

in

Geography

Waterloo, Ontario, Canada, 2024

© Saba Dezyani 2024

Author’s Declaration

I hereby declare that I am the sole author of this thesis. This is a true copy of the thesis, including any required final revisions, as accepted by my examiners.

I understand that my thesis may be made electronically available to the public.

Abstract

Lake ice is a significant aspect of the physical landscape at northern latitudes and plays a crucial role in regulating weather, climate, and supporting various socio-economic aspects. The sensitivity of lake ice development to air temperature makes it an effective indicator of climate change. This phenomenon not only impacts regional weather patterns but also contributes to global environmental shifts. It is important to closely observe variations in lake ice to gain insight into the potential impact that lakes might have on regional weather patterns and environmental conditions. This study focuses on monitoring lake ice dynamics using RADARSAT Constellation Mission (RCM) compact polarimetric data, employing a combination of the first difference method and compact polarimetric (CP) parameter analysis. The research centers on three Canadian sub-Arctic lakes, with a primary focus on Kluane Lake, and examines phenological transitions through changes in backscatter intensity and CP parameters such as Degree of Polarization (DoP), Circular Polarization Ratio (CPR), Relative Phase, and Alpha Angle. The results reveal that freeze-onset and melt-onset events, mapped using the first difference method, align well with validation data from Landsat thermal imagery and meteorological records, highlighting the reliability of RCM data. Additionally, CP parameter analysis provides deeper insights into ice surface and subsurface conditions. DoP and CPR captured variations in surface roughness, while Relative Phase and Alpha Angle distinguished subsurface scattering and ice-water transitions. Mid-winter stability, reflected by minimal variability in CP values across parameters, emerged as the most consistent pattern, signifying coherent solid or snow-covered ice surface. The results highlight the capacity of RCM data to capture key phenological events, demonstrating strong consistency with optical and thermal data sources. However, the research also identifies limitations related to the temporal resolution of RCM data.

Acknowledgments

I would like to sincerely thank my supervisor, Dr. Grant Gunn, for his continued guidance, support, and mentorship throughout my master's research. His thoughtful advice and encouragement have been key to my academic growth and the completion of this thesis. I am especially grateful for the opportunities he provided, including engaging in meaningful research and advancing my understanding of lake ice phenology.

I would also like to express my gratitude to Dr. Benoit Monpetit, whose valuable guidance during our discussions contributed significantly to refining the direction of my thesis. His expertise and insights were truly appreciated.

I am thankful to the Department of Geography and Environmental Management for their support and for fostering a positive academic environment. I also want to acknowledge my colleagues and friends, particularly those in the Cryosphere Research Lab.

Finally, I am deeply grateful to my family and friends for their unwavering encouragement, love, and support, which have been my greatest source of strength throughout this journey.

.

Dedication

This thesis is dedicated to Sadra, my unwavering support, and to Milan, my greatest source of inspiration.

Table of Contents

Author's Declaration ii

Abstract iii

Acknowledgments iv

Dedication v

List of Figures ix

List of Tables xv

Chapter 1 Introduction 1

1.1 Motivation 1

1.2 Research Objective 2

1.3 Thesis outline 2

Chapter 2 Background and Theory 4

2.1 Lake Ice Phenology 4

2.2 Freeze-up 5

2.3 Growth and Thickening 6

2.4 Decay 7

Chapter 3 Synthetic Aperture Radar (SAR) Applications in Lake Ice Monitoring 8

3.1 Dielectric Properties 8

3.2 Factors Affecting SAR Backscatter 11

3.2.1 Ice Structure 11

3.2.2 Sensor Properties and Incidence Angle 12

3.2.3 Snow Cover 13

3.2.4 Surface Wetness 13

3.3 Backscatter Evolution 14

3.3.1 Algorithmic Approaches for Detecting Lake Ice Phenology 16

3.4 Compact Polarimetric SAR 18

Chapter 4 Evaluating the RADARSAT Constellation Mission Compact Polarimetric Capabilities in Monitoring Sub-Arctic Lake Ice Dynamics 21

4.1 Introduction 21

4.2 Study Area 22

4.3 Data 24

4.3.1 RADARSAT Constellation Mission 24

4.3.2 Landsat Imagery 27

4.3.3 Planet Imagery 28

4.4 Methods 28

4.4.1 Study Area Selection Over Kluane Lake 29

4.4.2 Backscatter Analysis 31

4.4.3 Polarimetric Parameter Analysis 36

4.4.4 Preprocessing Landsat Images for Land Surface Temperature (LST) Calculation 41

4.5 Results 42

4.5.1 Freeze-onset Mapping Results 43

4.5.2 Melt-onset Mapping Results 46

4.5.3 Observed Trends in Compact Polarimetric (CP) Parameters During Ice Formation and Melting 57

4.6 Discussion 77

4.6.1 Backscatter Analysis and Phenological Event Detection 77

4.6.2 Compact Polarimetric Parameters and Surface Conditions 78

4.6.3 Limitations 83

4.7 – Conclusion 83

Chapter 5 Conclusion 85

5.1 Overall Summary 85
5.2 Limitations 85
5.3 Future Directions 86
References 89
Appendix A Compact Polarimetric Whisker Plots 99

List of Figures

Figure 1. Fresnel Reflection Coefficients for Horizontally Polarized Waves at the Air-Snow, Snow-Ice, and Ice-Water Interfaces at 5 GHz (C-band), as a Function of Incidence Angle. 11

Figure 2. Backscatter evolution during the spring melt over Kluane Lake in 2023, derived from RCM data and overlaid on a Google Earth satellite image. 16

Figure 3. Kluane Lake, Yukon Territory, Canada (61.276108°, -138.751161°); Study Site 1 and Study Site 2 are shown in blue and red hatched polygons (respectively). 23

Figure 4. Ryan Lake and Landing Lake, Northwest Territory, Canada 24

Figure 5. The most common polarization technique for spaceborne radar systems is linear polarization, in which the electric field of light is confined to a single plane along the direction of propagation. ... 25

Figure 6. In the compact polarization technique, light's electric field has two equal linear components perpendicular to each other. They differ in phase by $\pi/2$ (90 degrees), causing the electric field tip to rotate in a circle around the direction of propagation. The wave is termed left- or right-hand circularly polarized based on this rotation direction. 26

Figure 7. RCM images overlap across Kluane Lake 30

Figure 8. This map illustrates the frequency of RCM images across different sections of the lake. For the final analysis, a portion of the lake has been selected that contains images for at least half of the dates. 30

Figure 9. Workflow of the study area (Site 1) selection process across Kluane Lake 31

Figure 10. The time series of pixel-level backscatter values for Landing Lake from March to June 2023. This plot highlights the progression of backscatter changes over time. The figure illustrates that substantial drops in backscatter values may span several consecutive days rather than occurring within a single day. 35

Figure 11. Workflow for Identifying freeze-onset and melt-onset Dates 35

Figure 12. Spatial distribution of freeze-onset dates at Study Site 1 in Kluane Lake determined pixel by pixel using the first difference method during fall and winter 2023. 44

Figure 13. Backscatter variations at Points A and B on Kluane Lake, the map displays the spatial distribution of RCM image pixels over Kluane Lake, highlighting Points A and B. The time series graphs show the backscatter intensity at these points from October 2023 to January 2024..... 45

Figure 14. Seasonal Transition in Lake Surface Temperatures. This composite of Landsat-9 thermal band imagery showcases the shift in surface temperatures of Kluane Lake over two dates, November 29 and December 9, 2023. Study Site 1 and Study Site 2 are outlined in green and red, respectively. 46

Figure 15. Spatial distribution of melt-onset dates at Study Site 1 in Kluane Lake, determined pixel by pixel using the first difference method for spring 2023 47

Figure 16. Backscatter variations at Points C and D on Kluane Lake. The map displays the spatial distribution of backscatter intensity at Points A and B on Kluane Lake. The time series graphs illustrate backscatter intensity changes from February to May 2023. 48

Figure 17. Seasonal Transition in Lake Surface Temperatures. This series of Landsat-9 thermal images documents the progressive warming of Kluane Lake's surface during the spring melt on April 29, and May 13, 2023. Each image vividly captures the increase in temperatures across the lake, highlighting areas of significant warming that contribute to the changing ice cover dynamics during the transition from winter to spring. Study Site 1 and Study Site 2 are outlined in green and red, respectively. 49

Figure 18. Sequential Planet Images Capturing the Melt Period of Kluane Lake (16 April - 30 May), This series of Planet images illustrates the progression of ice melt on Kluane Lake during the spring of 2023. Starting on 16 April, the lake is predominantly covered in ice. By 3 May, initial melting is observed around the edges. The 11 May image shows more pronounced melting. On 24 May, ice reduction and cracks are evident. By 26 May, the lake is nearly ice-free, with only small ice fragments visible. Finally, on 30 May, Kluane Lake is completely free of ice, marking the end of the melt period. Study Site 1 and Study Site 2 are outlined in green and red, respectively. 51

Figure 19. Spatial distribution of melt-onset dates at Study Site 1 in Kluane Lake, determined pixel by pixel using the first difference method for spring 2024. 52

Figure 20. Seasonal Transition in Lake Surface Temperatures during the spring melt on April 12, and April 21, 2023..... 53

Figure 21. Spatial distribution of melt-onset dates for Landing Lake and Ryan Lake, determined pixel by pixel using the first difference method during spring 2023. The north arrow represents the true north. 54

Figure 22. Temporal Variation in Land Surface Temperatures. This series of Landsat-9 thermal band images captures the changing surface temperatures of Ryan and Lading lakes on three different dates—April 25, May 4, and May 12, 2023. The maps depict the gradual warming of the lake's surface as spring progresses, highlighting significant thermal shifts that impact the spring thaw. 56

Figure 23. Spring melt progression captured by Planet images over Ryan Lake and Landing Lake from April 24 to May 16, 2023. 57

Figure 24. Whisker plot of DoP values at Kluane Lake, Site 1 (October 2023–May 2024), shown across three incidence angles (38°, 44°, 50°) with mean daily temperatures (red dashed line), a 0°C reference line (black dash-dot), and freeze/melt-onset periods marked by vertical dashed lines. 59

Figure 25. Whisker plot of DoP values at Kluane Lake, Site 2 (October 2023–May 2024), shown across three incidence angles (27°, 44°, 50°) with mean daily temperatures (red dashed line), a 0°C reference line (black dash-dot), and freeze/melt-onset periods marked by vertical dashed lines. 59

Figure 26. CPR values at Kluane Lake, Site 1 (October 2023–May 2024), shown for incidence angles of 38°, 44°, and 50°, with mean daily temperature (red dashed line) and freeze/melt-onset periods marked by vertical dashed lines. 61

Figure 27. Temporal variation of the interquartile range (IQR) for the CPR at Kluane Lake, Site 1 (October 2023–May 2024), calculated across three incidence angles (38°, 44°, and 50°)..... 61

Figure 28. CPR values at Kluane Lake, Site 2 (October 2023–May 2024), shown for incidence angles of 27°, 44°, and 50°, with mean daily temperature (red dashed line) and freeze/melt-onset periods marked by vertical dashed lines. 62

Figure 29. Temporal variation of the interquartile range (IQR) for the CPR at Kluane Lake, Site 2 (October 2023–May 2024), calculated across three incidence angles (27°, 44°, and 50°)..... 62

Figure 30. Planet satellite imagery of Study Site 2, Kluane Lake captured on key dates during the ice formation and melting periods. October 3, 2023, showing an ice-free lake surface prior to freeze-up; February 2, 2024, displaying the lake in mid-winter with full ice cover; April 19, 2024, illustrating the lake during late winter; and May 16, 2024, showing the onset of ice melt with visible cracks and open water patches. Study Site 1 and Study Site 2 are outlined in green and red, respectively. 64

Figure 31. CPR values at Study Site 1, Kluane Lake, for key dates during the ice cycle. Images display CPR values on October 3, 2023, showing ice-free conditions; December 2, 2023, with increased CPR variability during the initial freeze-up phase; February 3, 2024, depicting stable low CPR values during

full ice cover; and May 9, 2024, illustrating heterogeneous CPR patterns as ice melt begins, with both high and low values indicating mixed ice-water surfaces. 65

Figure 32. CPR values at Study Site 2, Kluane Lake, for key dates during the ice cycle. October 3, 2023, representing ice-free conditions; December 2, 2023, showing increased CPR variability during the freeze-onset phase; February 2, 2024, depicting relatively low CPR values as the lake is fully frozen, and May 24, 2024, illustrating a mixed pattern of high and low CPR values as ice melt begins, creating heterogeneous surface conditions. 66

Figure 33. Whisker Plot of Relative Phase Difference (δ) at Study Site 1, Kluane Lake, from October 2023 to May 2024. This plot shows δ values at incidence angles of 38°, 44°, and 50°, overlaid with mean daily temperature (red dashed line) and a 0°C reference line. Freeze-onset and melt-onset periods, calculated using the First Difference method, are marked with vertical dashed lines. 68

Figure 34.Temporal variation of the interquartile range (IQR) for the Relative Phase at Kluane Lake, Site 1 (October 2023–May 2024), calculated for incidence angles 38°, 44°, and 50°, with vertical dashed lines indicating freeze-onset and melt-onset periods. 69

Figure 35. Whisker Plot of Relative Phase Difference (δ) at Study Site 2, Kluane Lake, from October 2023 to May 2024. This plot shows δ values at incidence angles of 27°, 44°, and 50° with mean daily temperature and a 0°C line. Freeze-onset and melt-onset periods, calculated using the First Difference method, are marked with vertical dashed lines. 69

Figure 36. Temporal variation of the interquartile range (IQR) for the Relative Phase at Kluane Lake, Site 2 (October 2023–May 2024), calculated for incidence angles 27°, 44°, and 50°, with vertical dashed lines indicating freeze-onset and melt-onset date range. 70

Figure 37. Spatial Distribution of Relative Phase (δ) at Study Site 1, Kluane Lake, from October 2023 to May 2024. 70

Figure 38. Spatial Distribution of Relative Phase (δ) at Study Site 2, Kluane Lake, from October 2023 to May 2024. 71

Figure 39. Whisker Plot of Alpha Angle (α) at Study Site 1, Kluane Lake, from October 2023 to May 2024. This plot shows alpha values in degrees across incidence angles (38°, 44°, and 50°), with mean daily temperature (red dashed line) and a 0°C reference line. Vertical dashed lines mark the freeze-onset and melt-onset date ranges. 72

Figure 40. Temporal variation of the interquartile range (IQR) for the Alpha Angle at Kluane Lake, Site 1 (October 2023–May 2024), calculated for incidence angles 38°, 44°, and 50°, with vertical dashed lines indicating freeze-onset and melt-onset date ranges. 73

Figure 41. Whisker Plot of Alpha Angle (α) at Study Site 2, Kluane Lake, from October 2023 to May 2024. This plot presents alpha values with incidence angles (27°, 44°, and 50°), mean daily temperature, and freeze/melt-onset date ranges. 74

Figure 42. Temporal variation of the interquartile range (IQR) for the Alpha Angle at Kluane Lake, Site 2 (October 2023–May 2024), calculated for incidence angles 27°, 44°, and 50°, with vertical dashed lines indicating freeze-onset and melt-onset date ranges. 74

Figure 43. Alpha Angle Values in Degree for Study Site 1, Kluane Lake, from October 2023 to May 2024. 75

Figure 44. Alpha Values in Degrees for Study Site 2, Kluane Lake, from October 2023 to May 2024. 76

Figure 45. Whisker Plot of Conformity Coefficient at Study Site 1, Kluane Lake, from October 2023 to May 2024..... 99

Figure 46. Whisker Plot of Conformity Coefficient at Study Site 2, Kluane Lake, from October 2023 to May 2024..... 100

Figure 47. Whisker Plot of Degree of Circularity at Study Site 1, Kluane Lake, from October 2023 to May 2024..... 100

Figure 48. Whisker Plot of Degree of Circularity at Study Site 2, Kluane Lake, from October 2023 to May 2024..... 101

Figure 49. Whisker Plot of Degree of Ellipticity at Study Site 1, Kluane Lake, from October 2023 to May 2024..... 101

Figure 50. Whisker Plot of Degree of Ellipticity at Study Site 2, Kluane Lake, from October 2023 to May 2024..... 102

Figure 51. Whisker Plot of Linear Polarization Ratio at Study Site 1, Kluane Lake, from October 2023 to May 2024..... 102

Figure 52. Whisker Plot of Linear Polarization Ratio at Study Site 2, Kluane Lake, from October 2023 to May 2024..... 103

Figure 53. Whisker Plot of Degree of Depolarization at Study Site 1, Kluane Lake, from October 2023 to May 2024..... 103

Figure 54. Whisker Plot of Degree of Depolarization at Study Site 2, Kluane Lake, from October 2023 to May 2024..... 104

Figure 55. Whisker Plot of S0 at Study Site 1, Kluane Lake, from October 2023 to May 2024. 104

Figure 56. Whisker Plot of Stoke Parameter S0 at Study Site 2, Kluane Lake, from October 2023 to May 2024..... 105

Figure 57. Whisker Plot of Stoke Parameter S1 at Study Site 1, Kluane Lake, from October 2023 to May 2024..... 105

Figure 58. Whisker Plot of Stoke Parameter S1 at Study Site 2, Kluane Lake, from October 2023 to May 2024..... 106

Figure 59. Whisker Plot of Stoke Parameter S2 at Study Site 1, Kluane Lake, from October 2023 to May 2024..... 106

Figure 60. Whisker Plot of Stoke Parameter S2 at Study Site 2, Kluane Lake, from October 2023 to May 2024..... 107

Figure 61. Whisker Plot of Stoke Parameter S3 at Study Site 1, Kluane Lake, from October 2023 to May 2024..... 107

Figure 62. Whisker Plot of Stoke Parameter S3 at Study Site 2, Kluane Lake, from October 2023 to May 2024..... 108

List of Tables

Table 1. The diversity of SAR systems for lake ice research (Murfitt & Duguay, 2021) 26

Table 2. Final data structure matrix 34

Table 3. Percentage of frozen pixels at Study Site 1 in Kluane Lake During Winter 2023, based on the first difference method 44

Table 4. Percentage of melted pixels over spring 2023 for Kluane Lake selected area based on the first difference method 47

Table 5. Percentage of melted pixels over spring 2023 for Landing Lake and Ryan Lake based on the first difference method 55

Chapter 1
Introduction

1.1 Motivation

Lakes cover about 2% of Earth's land surface, mainly in the Northern Hemisphere where they can occupy 15-40% of the landscape (Duguay et al., 2003). Lake ice plays an important role in regulating weather and climate in northern latitudes by impacting temperature fluctuations. Its sensitivity to air temperature makes it an effective indicator of climate change. The Global Climate Observing System (GCOS) recognizes lake ice thickness and cover as essential climate proxies (ECVs) (Brown & Duguay, 2010). Recent observations and projected climate changes suggest shorter ice seasons and thinner ice covers in the Northern Hemisphere, highlighting the sensitivity of lake ice to air temperature Magnuson et al., 2000). Recent long-term trends showed a significant shift in lake ice phenology across the Northern Hemisphere, including a delay in freeze-up times by approximately 1.5 days per decade (Hewitt, 2019), while ice breakup trends for 152 Northern Hemisphere lakes from 1951 to 2014, showed a median trend of ice breakup occurring 1.2 days earlier per decade (Lopez et al., 2019).

The intricate relationship between lake ice conditions and climate variability is further highlighted by the significant social and cultural implications for indigenous communities and local ecosystems. (Golden et al., 2015). The shorter ice cover duration in the Northern Hemisphere has affected a variety of ice-related recreations, such as ice hockey, ice skating, fishing tournaments, and spiritual ceremonies (Knoll et al., 2019). Additionally, a reduction in the ice season length may adversely affect subsistence activities as well as the accessibility and connectivity of remote First Nations communities (Woolway et al., 2022; Mullan et al., 2017). It is predicted that the time when the ice is thick enough for activities like transportation, ice fishing, and recreation will decrease with global warming (Woolway et al., 2022). This impacts significantly northern communities, in terms of winter ice roads that provide cost-effective transport of goods and services to remote regions.

Beyond its social significance, changing lake ice conditions have profound ecological and environmental impacts, influencing water quality, freshwater ecology, fish distributions, behaviors, and biogeochemical processes. Warmer temperatures have reduced the number of cold-stenothermal fish species, such as the Arctic charr, while increasing the number of eurythermal species like carp. These shifts in fish populations may change the size, structure, life history, and overall dynamics of lake ecosystems (Adrian et al., 2016). Furthermore, lakes with shorter ice cover and more melt events may have less nitrate accumulation and higher peak nitrate concentrations, influencing the lake's nutrient

cycle and phytoplankton growth (Kincaid et al., 2022). Therefore, careful observation of lake ice changes is key to understanding potential impacts on regional weather patterns and environmental conditions.

Despite the importance of lake ice monitoring, in-situ observations in Canada have declined over the past three decades, making satellite imagery increasingly vital for studying lake ice phenology (Murfitt & Duguay, 2020). Satellite data provide consistent, high-resolution observations, especially for remote regions, enabling researchers to monitor complex dynamics such as freeze-up and break-up dates and ice cover duration (Duguay et al., 2014). This study evaluates the potential of RADARSAT Constellation Mission (RCM) compact polarimetry to accurately determine freeze and melt timings and monitor ice conditions throughout the ice cycle in sub-Arctic lakes in Canada by analyzing backscatter intensity and compact polarimetric parameters.

1.2 Research Objective

This study aims to determine the freeze and melt timings of lake ice in three selected lakes in Canada's sub-Arctic regions, where ground observations are limited. Specifically, the objectives of this research are to 1) utilize RADARSAT Constellation Mission (RCM) images, with a particular focus on compact polarimetry data using the innovative circular polarization method, to monitor lake ice changes throughout the ice cycle. Changes in microwave backscatter intensity and the first difference method will be employed to detect variations between datasets and to extract ice events from RCM acquisitions. 2) To evaluate the ability of compact polarimetric parameters—such as Degree of Polarization (DoP), Circular Polarization Ratio (CPR), Relative Phase, and Alpha Angle—to provide additional insights into ice surface conditions during freeze-onset and melt-onset periods. 3) To validate the accuracy of RCM in retrieving lake ice phenology events, the results will be compared with data from multiple sources, including Landsat Land Surface Temperature (LST) maps, Planet imagery, and meteorological data from weather stations. Through this study, we anticipate gaining a nuanced understanding of the strengths and potential limitations of RCM's compact polarimetry in capturing lake ice phenology across sub-Arctic lakes in Canada with diverse morphometric characteristics.

1.3 Thesis outline

Chapter 2 provides a detailed explanation of the seasonal cycle of lake ice, focusing on the freeze-up and break-up processes. It explores the effect of climatic factors such as temperature, solar radiation,

and lake morphometry on these cycles and discusses the thermodynamic principles that regulate lake ice behavior, highlighting the energy exchanges between the lake, ice, and atmosphere.

Chapter 3 outlines the application of synthetic aperture radar (SAR) in monitoring lake ice, emphasizing the importance of SAR's ability to detect differences in radar return signals during freeze-up and break-up events. It highlights how this contrast is influenced by sensor parameters—such as frequency and incidence angle—and by the physical properties of lake ice, including ice structure, snow cover, and surface wetness.

Chapter 4 presents the methodology and results of using RCM compact polarimetric data to monitor lake ice phenology at Kluane Lake and other sub-Arctic lakes in Canada. It details the acquisition and processing of RCM compact polarimetric images, the application of the first difference method for backscatter analysis, and the use of compact polarimetric parameters such as Degree of Polarization, Circular Polarization Ratio, Relative Phase, and Alpha Angle to examine ice conditions. The chapter discusses key findings, including the identification of ice phenological events, and validates results using Landsat imagery, meteorological data, and planet imagery.

Chapter 5 summarizes the main findings, highlighting the contributions to understanding lake ice dynamics in sub-Arctic regions. It outlines the limitations encountered during the research and recommends future research studies to improve lake ice monitoring and prediction using compact polarimetry and other SAR data sources.

Chapter 2
Background and Theory

2.1 Lake Ice Phenology

"Lake ice phenology" refers to the seasonal cycle of lake ice formation and melting, including the periods of freezing and thawing, as well as the overall length of time the ice remains on the lake. In this cycle 'freeze-up' and 'break-up' terms encompass a series of ongoing processes, while ‘freeze-onset’ and ‘melt-onset’ represent specific dates on the calendar (Duguay et al., 2014). These events provide valuable information about the changing environment, serving as key indicators for understanding environmental shifts caused by climatic changes, particularly in high-latitude regions.

The development of lake ice is primarily influenced by climatic variables, particularly air temperature, but it is also governed by fundamental physical laws. According to the first law of thermodynamics, energy cannot be created or destroyed in an isolated system; it can only be transferred or transformed. This principle is crucial in understanding lake ice behavior, as it means that the exchange of energy between the atmosphere, water, and ice drives changes in the ice cover, whether it is forming, thickening, or melting (Williams, 1965). Understanding this balance of energy is key to interpreting the phases of lake ice development and the role of both climatic and non-climatic factors (Brown & Duguay, 2010).

The main factor influencing the timing of ice phenology events is air temperature. Since most lakes are in regions experiencing winter air temperatures below 0°C, ice cover is frequent, making the relationship between temperature and ice phenology a critical area of study. Early studies indicated that monitoring the temperature before these events is useful to predict the timing of these events. However, the link between temperature and ice phenology events is more complicated and latitude causes a nonlinear relationship (Weyhenmeyer et al., 2004). Other climatic factors influencing ice phenology include snow accumulation, wind, and solar radiation, which complicate the freeze-up/break-up processes (Duguay et al., 2006; Brown & Duguay, 2010).

Beyond climatic factors, the shape and characteristics of a lake, known as lake morphometry, play an essential role in lake ice cover. Wind exposure, water flow, and temperature are influenced by the lake's shape, especially its depth. For instance, lake depth has an important effect on heat storage, impacting the time required for cooling and freezing (Brown & Duguay, 2010). Additionally, lakes

located in higher elevations tend to have longer ice cover seasons. The inflow of water into a lake also contributes to ice formation and melting, as it introduces warmth and potential currents, either delaying ice development or causing earlier melt and break-up (Williams, 1965; Brown & Duguay, 2010).

2.2 Freeze-up

The onset of ice formation in lakes is a complex process influenced by a variety of thermal and dynamic interactions. This process begins as surface temperatures of the lake drop below the freezing point, leading to the development of ice cover on the water's surface. As lakes cool during the autumn and early winter months, the process of freeze-up begins when the surface water temperature drops below 4°C, the point of maximum density for freshwater (Jeffries et al., 2013). At this stage, a stable, lighter layer of water at the surface, which keeps losing heat until it reaches the freezing point, leading to the initial ice formation, known as ice skim. (Jeffries et al., 2013). This ice skim marks the first visible stage of the lake's transition into its winter state. The characteristics of the forming ice, including its texture and crystallography, are influenced by several factors such as wind, wave action, and meteorological conditions during the initial freezing phase.

Several factors contribute to this process. Summer and fall temperatures, as well as the amount of solar radiation absorbed during the ice-free months, are the main factors in the freeze-up process Ragotzkie, 1978). The amount of heat stored in the lake during these months, affected by the lake's size, depth, and geographic location, significantly impacts the timing of freeze-up. In particular, anomalous climatic events, such as El Niño (Rouse et al., 2000), can lead to higher air temperatures and delayed freeze-up due to increased evaporation rates and prolonged heat storage within the lake (Brown & Duguay, 2010).

Moreover, the interaction between the lake's thermal response and its physical environment, such as wind action and the lake's morphometry, determines the onset of ice formation (Jeffries et al., 2013). In larger lakes, the process is more dynamic, with ice cover formation being influenced by factors such as fetch, lake depth, and volume. These factors contribute to the variability in the timing and nature of ice formation across different lakes (Jeffries et al., 2013; Ragotzkie, 1978).

As the freeze-up continues, the nature of the ice formed varies, with clear, black ice, known as congelation ice, typically forming first. This is followed by the formation of snow ice, a result of flooding and freezing of overlying snow or direct snowfall during the initial freeze-up (Jeffries et al., 2013). The formation of these ice types depends on the lake's morphology and prevailing weather

conditions, with black ice more prevalent in central areas and snow ice forming predominantly along the shorelines due to wind-driven snow accumulation (Bengtsson, 1986).

The final stage of the freeze-up process fundamentally changes the thermal dynamics of the lake. Once fully ice-covered, the lake's heat exchange with the atmosphere is significantly reduced, concentrating primarily on the ice surface (Ragotzkie, 1978). Additionally, the subsequent snowfall on the ice cover further insulates the lake, lowering heat loss and allowing the water beneath the ice to warm gradually. This warming, combined with solar radiation that penetrates the ice, contributes to the gradual thickening of the ice cover over time (Ragotzkie, 1978).

2.3 Growth and Thickening

Lake ice growth and thickening is a complex process influenced by a wide range of factors, including temperature gradients, snow cover, cloud presence, and the physical characteristics of the lake (Adams, 1976; Jeffries et al., 2013). As winter progresses, snowfall becomes a significant factor in the development of lake ice. Initially, snow can accelerate the cooling of the lake's surface, promoting ice formation. However, once established, a snow layer acts as an insulator due to its lower thermal conductivity compared to ice. This insulating effect plays a crucial role as the freeze-up phase transitions into the ice growth stage, influencing how the lake ice thickens throughout the winter months. The insulation provided by the snow slows down heat transfer from the water to the atmosphere, which in turn decelerates the ice-thickening process beneath the snow layer (Adams, 1976; Brown & Duguay, 2010).

Cloud cover introduces another layer of complexity to this process. Clouds can reflect solar energy away from the ice, reducing warming, and trapping emitted longwave radiation from the ice surface, potentially warming it (Wang & Key, 2005). Thus, cloud presence indirectly affects the rate of ice growth, further highlighting the intricate relationship between atmospheric conditions and lake ice dynamics. This balance is particularly delicate in high-latitude regions where polar darkness dominates (Curry et al., 1993). During these periods, the energy balance of the ice is largely controlled by longwave radiation fluxes, with clear skies typically leading to more significant ice growth due to increased radiative cooling (Brown & Duguay, 2010).

In addition to these external factors, the lake's inherent physical properties, such as its inflow and outflow dynamics, significantly contribute to the ice-thickening process. Dynamic water bodies with significant inflows and outflows can maintain areas of open water, known as polynyas, throughout the

winter (Jeffries et al., 2013). These areas are critical for heat and mass exchange between the water body and the atmosphere and can influence the overall stability and thickness of the ice cover (Jeffries et al., 2013).

2.4 Decay

The melting process of lake ice, often referred to as ice break-up, is a dynamic period where the ice transitions from a solid state back into water, marking the end of the ice season. This transition is primarily driven by rising temperatures in the spring, as the ice begins to absorb more heat from the atmosphere. This heat gain is the primary driver of ice decay, initiating melting at the surface, bottom, and lateral edges of the ice pack ; Heron & Woo, 1994). As the ice approaches the isothermal point of 0°C, the thermodynamic decay of lake ice becomes more nuanced, with the top and bottom surfaces melting simultaneously (Jeffries et al., 2013).

Initially, during the melt season, snow cover acts as a protective layer over the ice, reflecting much of the incoming solar radiation due to its high albedo, thereby slowing the melting process (Michel et al., 1986). However, as temperatures continue to rise, the snow transitions from being a protective layer to an agent of change, warming the ice surface and expediting the break-up process (Brown & Duguay, 2010). Concurrently, the ice's internal structure is altered, with changes in the orientation and integrity of ice crystals making the ice more fragile and prone to disintegration under external force (Ashton, 1986).

Wind also plays a critical role during this stage, particularly when the ice is already weakened by thermal processes. It can exert significant mechanical force on the ice, causing it to fracture into smaller fragments. This fragmentation process is significant because it increases the ice's surface area exposed to the elements, thereby accelerating melting as more ice comes into direct contact with warm air and water (Williams, 1965; Ashton, 1986). Additionally, the inflow of warmer water from sources like rivers or runoff can erode the ice at its peripheries and from beneath, further compromising the stability of the ice cover. Together, these processes—driven by wind and warm water inflows—highlight the interconnected and multifaceted nature of ice decay dynamics during the melt season (Williams, 1965; Brown & Duguay, 2010).

Chapter 3

Synthetic Aperture Radar (SAR) Applications in Lake Ice Monitoring

In recent decades, remote sensing technologies have become critical tools for observing lake ice dynamics, especially as ground-based measurements have decreased since the 1980s (Lenormand et al., 2002). Satellite remote sensing technology, with its high temporal and spatial resolution products, has become essential for monitoring lake ice properties (Duguay et al., 2015; Murfitt & Duguay, 2021), particularly in regions where traditional monitoring methods are constrained by geographical and climatic challenges. Recent studies utilizing these technologies have provided critical insights into the temporal and spatial variability of lake ice cover, particularly during the critical periods of freeze-up and break-up (Geldsetzer et al., 2010; Howell et al., 2009).

Three main types of remote sensing systems are commonly used to monitor lake ice phenology: active microwave, passive microwave, and optical sensors. Each has its own advantages and limitations when it comes to capturing ice dynamics (Duguay et al., 2015). Among these, radar-based techniques, particularly Synthetic Aperture Radar (SAR), stand out due to their ability to capture data regardless of weather or lighting conditions. This advantage makes SAR an invaluable tool in regions experiencing polar darkness, where optical sensors become less reliable (Brown & Duguay, 2012). Its ability to detect backscatter intensities and polarizations has made it possible to achieve high classification accuracies in distinguishing between ice and open water.

While SAR technology provides crucial data for lake ice monitoring, accurately interpreting this data requires an understanding of several key factors. In the following sections, we will examine how the dielectric properties of ice, its structure (including thickness and air bubbles), and sensor characteristics like frequency and incidence angle influence SAR backscatter. We will also explore the effects of snow cover and surface wetness, particularly during freeze-up and melt, to improve the reliability of SAR data in monitoring lake ice dynamics.

3.1 Dielectric Properties

To accurately interpret SAR data, it is essential to understand how lake ice interacts with electromagnetic waves, a key aspect of remote sensing technology and interpreting radar data. The dielectric properties of ice, mainly its relative permittivity, are significant factors that impact the backscatter characteristics observed in SAR imaging. These properties not only reflect the ice's physical

state and composition but also influence the radar waves' penetration depth and scattering behaviors, crucial for monitoring lake ice variation through remote sensing.

Dielectrics are materials that act as electrical insulators, meaning they do not conduct electricity but can support an electrostatic field. When an external electric field is applied to a dielectric material, it becomes polarized, separating its positive and negative charges. This polarization creates an internal electric field that opposes the external field (Evans, 1965). The extent to which a dielectric can be polarized is described by its permittivity (ε), which is a measure of the material's ability to store electrical energy in an electric field (Gunn, 2015; Evans, 1965).

Relative permittivity, or the dielectric constant, is the ratio of a material's permittivity to that of a vacuum. The Debye equation (Debye, 1929) is useful for understanding how permittivity evolves with frequency, particularly in polar substances like water. Equation 1 models dielectric relaxation, where the ability of dipoles within the material to align with an electric field decreases at higher frequencies:

$$\varepsilon(\omega) = \varepsilon_\infty + \frac{\varepsilon_s - \varepsilon_\infty}{1 + i\omega\tau} \qquad (1)$$

Where $\varepsilon(\omega)$ is the complex permittivity of the material at angular frequency ω, ε_s is the static permittivity at zero frequency, $\boldsymbol{\varepsilon}_\infty$ is the permittivity at infinite frequency (i.e., the permittivity when the frequency is so high that dipole orientation cannot follow the oscillating field), i is the imaginary unit, ω is the angular frequency of the applied electric field, defined as 2π times the frequency, and τ is the relaxation time, representing the average time it takes for polar molecules in the material to reorient themselves in response to the electric field (Debye, 1929).

Ice and water exhibit significantly different permittivity profiles, which is crucial for radar interaction. Liquid water has a high relative permittivity, around 90 at C-band frequencies (~5 GHz), but it decreases with frequency, with values near 20 at Ku-band (~17 GHz). In contrast, solid-phase water (ice) has a much lower dielectric constant, approximately 3.17, which remains relatively stable across microwave frequencies (G. E. Gunn et al., 2018). The presence of liquid water within snow or ice increases the overall permittivity, dramatically altering radar backscatter and highlighting areas of melting or liquid water inclusions (Ellison et al., 1996).

The dielectric properties of ice are influenced by factors such as air bubbles or impurities. The effective permittivity of ice with air bubbles can be modeled using mixing formulas, which account for the fraction of air inclusions. Even small amounts of inclusions can substantially modify the dielectric

properties, altering radar signal behavior. At the ice-water interface, the difference in dielectric properties leads to nearly specular reflection. This behavior can be quantified using Fresnel reflection coefficients for horizontally and vertically polarized waves (Ulaby et al., 1986):

For horizontally polarized waves, the reflection coefficient $R_{\perp}$ is:

$$R_{\perp} = \frac{\varepsilon^*_{ice}\cos\theta_1 - \varepsilon^*_{air}\cos\theta_2}{\varepsilon^*_{ice}\cos\theta_1 + \varepsilon^*_{air}\cos\theta_2} \quad (2)$$

For vertically polarized waves, the reflection coefficient $R_{\parallel}$ is:

$$R_{\parallel} = \frac{\varepsilon^*_{air}\cos\theta_1 - \varepsilon^*_{ice}\cos\theta_2}{\varepsilon^*_{ice}\cos\theta_1 + \varepsilon^*_{ice}\cos\theta_2} \quad (3)$$

The interaction between SAR waves and lake ice is primarily determined by the dielectric contrast between different media (air, ice, water). This contrast dictates reflection and transmission at the boundaries between these media. When radar waves encounter a high contrast in permittivity, such as between ice and water, strong backscatter is often observed, particularly as surface bounce in radar data. This dielectric contrast is important for understanding scattering mechanisms in lake ice because the high permittivity of water results in stronger reflections compared to ice's lower permittivity (Evans, 1965; Gunn et al., 2018).

To visualize this behavior, Figure 1 illustrates the reflection coefficients for horizontally polarized waves at the air-snow, snow-ice, and ice-water interfaces as a function of incidence angle at C-band (5.4 GHz). The plot clearly demonstrates the differences in reflectance between these interfaces:

Ice-Water Interface: The reflection coefficient remains high (above 0.9) across all incidence angles, highlighting the significant dielectric contrast between ice ($\varepsilon \approx 3.17$) and water ($\varepsilon \approx 90$), which causes strong reflections and is consistent with SAR observations of melting ice.

Snow-Ice Interface: A moderate reflection coefficient (from 0.2 to 0.3), gradually decreasing with higher incidence angles, is observed. This is due to the smaller dielectric difference between snow ($\varepsilon \approx 1.5$) and ice ($\varepsilon \approx 3.17$), leading to less pronounced reflection.

Air-Snow Interface: The air-snow interface shows the lowest reflection coefficient across all incidence angles, consistent with the minimal dielectric contrast between air ($\varepsilon \approx 1$) and snow ($\varepsilon \approx 1.5$).

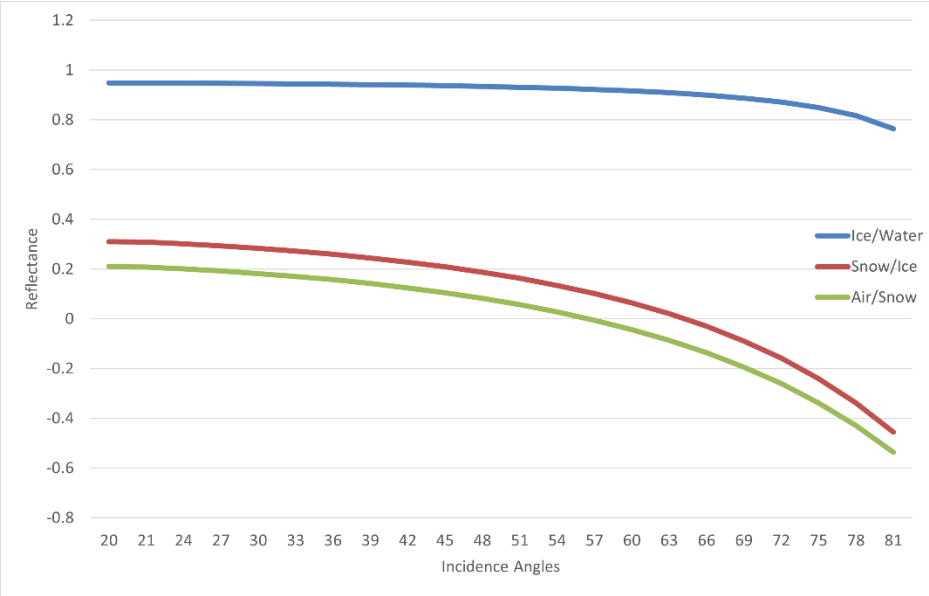


Figure 1. Fresnel Reflection Coefficients for Horizontally Polarized Waves at the Air-Snow, Snow-Ice, and Ice-Water Interfaces at 5 GHz (C-band), as a Function of Incidence Angle.

3.2 Factors Affecting SAR Backscatter

Given the complexity of ice properties, various environmental factors influence SAR backscatter from lake ice, including the structure of the ice, snow cover, and surface wetness. These factors play a crucial role in shaping the radar signal's interaction with the ice and its subsurface layers. For example, the presence of bubbles within the ice contributes to higher backscatter, while smooth, newly formed ice tends to have lower backscatter values.

3.2.1 Ice Structure

Lake ice structure, particularly its clarity and the presence of air bubbles, plays a significant role in determining the backscatter intensity observed in SAR imagery. Clear ice, often found in deeper lakes where the gas content of the water does not reach nucleation levels, results in minimal backscatter and appears darker in radar imagery (Duguay et al., 2002; Morris et al., 1995; Jeffries et al., 1994). In contrast, thick ice from shallow lakes on the North Slope of Alaska exhibits strong backscatter, hypothesized to be the result of double-bounce reflections (Morris et al., 1995). This process occurs when radar signals reflect off vertically oriented tubular bubbles in the ice, then off the ice-water interface, where a significant dielectric contrast enhances the radar return (Duguay et al., 2002). The

double-bounce mechanism could be effective in returning a substantial portion of the incident radar energy to the satellite, rendering the floating ice bright in radar images.

Furthermore, the development of tubular bubbles within the ice significantly influences the radar backscatter, especially for floating ice. Conversely, ice that grounds on the lake bed shows markedly lower backscatter due to the reduced dielectric contrast between the ice and sediments, resulting in signal loss when the ice adheres to the lake bed (Weeks et al., 1978; Jeffries et al., 1994). As winter progresses and the ice thickens, the area of ice with strong backscatter decreases, while the area with low backscatter, representing grounded ice, expands. This dynamic shift occurs as an increasing proportion of ice becomes grounded within the winter season (Jeffries et al., 1994; Weeks et al., 1978). Recent studies using polarimetric decomposition have indicated that the dominant source of backscatter from floating lake ice is from single-bounce response from the roughness at the ice-water interface (Atwood et al., 2015; Gunn et al., 2018). The roughness at the ice-water interface is caused by a dual influence of variable ice thicknesses from the insular capacity of variable snow depth on the lake, and the roughness created by bubbles resting at the ice-water interface (G. E. Gunn et al., 2018). The roughness parameter has been shown to be the most sensitive to variability in modeled backscatter from ice covered lakes using dense media radiative transfer models like the Snow Microwave Radiative Transfer model (SMRT) (Picard et al., 2013; Murfitt et al., 2023). Direct measurements of roughness at the ice-water interface have yet to be quantified in the field.

In summary, the structural characteristics of lake ice, including its clarity and the presence of tubular bubbles, significantly influence radar backscatter. The interaction of radar signals with these structural features, through mechanisms such as double-bounce reflection and dielectric contrasts, plays a critical role in determining the backscatter intensity observed in SAR imagery. These insights are essential for interpreting radar images of lake ice and understanding the processes governing ice growth and decay.

3.2.2 Sensor Properties and Incidence Angle

Apart from ice structure, SAR backscatter is also sensitive to the geometric configuration between the radar and the target surface, as well as to sensor properties such as frequency, polarization, resolution, and the sensor's noise floor (Skrunes et al., 2012). The incidence angle, defined as the angle between the incident radar beam and the normal to the target surface, has a significant impact on the microwave backscatter observed from lake ice surfaces.

Research indicates that backscatter intensity tends to decrease with increasing incidence angles, as shown in a study by Mahmud et al. (2018) using C-band and L-band SAR over Arctic sea ice. For the L-band, FYI showed a mean incidence angle dependency of -0.21 dB/1°, and MYI had -0.30 dB/1°, while C-band data exhibited dependencies of -0.22 dB/1° for FYI and -0.16 dB/1° for MYI. Duguay et al. (2002) also observed that higher incidence angles generally led to increased backscatter from floating lake ice, while lower angles yielded reduced backscatter. Such variations are influenced by the ice's physical properties, particularly its bubble content. (Duguay et al., 2002).

3.2.3 Snow Cover

Snow cover is another critical factor that significantly impacts SAR backscatter intensity from lake ice, with characteristics such as depth, density, and wetness affecting ice growth rates and altering its dielectric properties (Dabboor & Shokr, 2021). Particularly at longer wavelengths such as C-band (5 GHz) or L-band (23 GHz), snow cover plays an indirect role in affecting radar backscatter, especially during the ice growth phase. The insulating properties of snow can lead to reduced ice growth rates under thicker snow cover, thereby influencing the ice's dielectric properties (G. E. Gunn et al., 2018).

During the break-up season, however, melting snow on the ice surface can decrease backscatter intensity due to increased absorption and scattering of the radar signal by the wet snow layer (Morris et al., 1995). This effect is especially noticeable when the snow cover melts and exposes the underlying ice to direct solar radiation, accelerating melt processes and further decreasing backscatter intensity (Gunn et al., 2018; Morris et al., 1995).

3.2.4 Surface Wetness

Finally, as the ice begins to melt in spring, the presence of wet snow and meltwater on the ice surface plays a critical role in changing the radar signal's interaction with the ice. The increased moisture leads to greater absorption of the radar signal, resulting in a general decrease in backscatter intensity (Jeffries et al., 1994).

Moreover, as the melt season advances, the ice's granular structure becomes more pronounced due to the percolation of meltwater, which refreezes and forms highly reflective layers when temperatures drop again. This cyclical process of thawing and refreezing contributes to fluctuations in backscatter values (Morris et al., 1995). The dynamics of surface wetness, influenced by climatic conditions, cause significant day-to-day variations in backscatter signals during transition seasons, which is crucial for

accurately timing the onset of melt and the eventual timing of when the water is completely free of ice (Morris et al., 1995).

3.3 Backscatter Evolution

The evolution of SAR backscatter throughout the lake ice cycle provides valuable insights into the physical changes occurring in the ice and its environment. At the start of winter, when a thin, smooth ice layer forms, backscatter intensities remain low due to specular reflection, as the radar signal is directed away from the receiver (Duguay et al., 2002; Morris et al., 1995; Jeffries et al., 1994).

As the ice thickens throughout winter, especially in shallow lakes, backscatter intensities increase (Morris et al., 1995). This rise is primarily driven by the roughened ice-water interface and the scattering effect of air bubbles within the ice (Duguay et al., 2002). As the ice grows, the number of bubbles increases, scattering the radar signal in multiple directions and enhancing the radar return. Dabboor and Shokr (2021) emphasize that the increased density of air bubbles and a rougher ice-water interface contribute to higher backscatter due to enhanced volume scattering. As the ice continues to thicken, backscattering coefficient parameters such as σ^0_{RH}, σ^0_{RV}, and σ^0_{RR} are theorized to show a linear increase corresponding to this growth in bubble density (Dabboor & Shokr, 2021).

However, ice deformation features, like cracks and ridges, can lead to localized reductions in backscatter intensity (Hall et al., 1994). While these features may initially generate strong backscatter due to their complex surfaces, they can subsequently cause a temporary decrease in overall backscatter as water rises through the cracks, wetting the surrounding snowpack or forming snow ice, which absorbs the radar signal more effectively (Duguay et al., 2002; Hall et al., 1994). Moreover, another source of decrease in backscatter intensity, particularly in Arctic and subArctic regions, is attributed to the ice freezing to the bed. This phenomenon occurs due to the low contrast in dielectric constants between the lake ice and the lake bed sediments (3.2.1), leading to increased radar signal absorption (Duguay et al., 2002).

As ice reaches its maximum thickness, typically by late March, backscatter intensities tend to plateau. This saturation effect indicates that beyond a certain point, additional thickness or bubble inclusions have minimal impact on the backscatter signal (Duguay et al., 2002).

During the spring thaw, backscatter patterns change significantly due to rising temperatures. The melting of ice and snow cover alters their physical properties, affecting their interaction with radar

signals (Morris et al., 1995). Backscatter values, which peaked during winter, decline sharply as liquid water absorbs radar signals more effectively than ice, leading to reduced backscatter. The smoother ice surface during melting further enhances specular reflection away from the radar receiver (Morris et al., 1995; Duguay et al., 2002). Figure 2 illustrates these changes over Kluane Lake (Yukon Territory (YT)) during the spring melt, showing a sharp decrease in backscatter as the transition from ice-covered to thawed conditions occurs. The most significant declines are observed by May 7 and May 19 , 2023, when the presence of liquid water absorbs radar signals more effectively.

In summary, understanding the dynamic evolution of backscatter intensity during the lake ice cycle reveals the intricate relationship between ice growth, structural changes, and environmental conditions, which all influence radar signals (Duguay et al., 2002). Key factors such as ice thickness, air bubbles, and surface conditions shape the radar backscatter profile (Morris et al., 1995). This understanding is essential for accurately interpreting radar imagery of ice-covered lakes and provides valuable insights into ice growth patterns and broader climate implications.

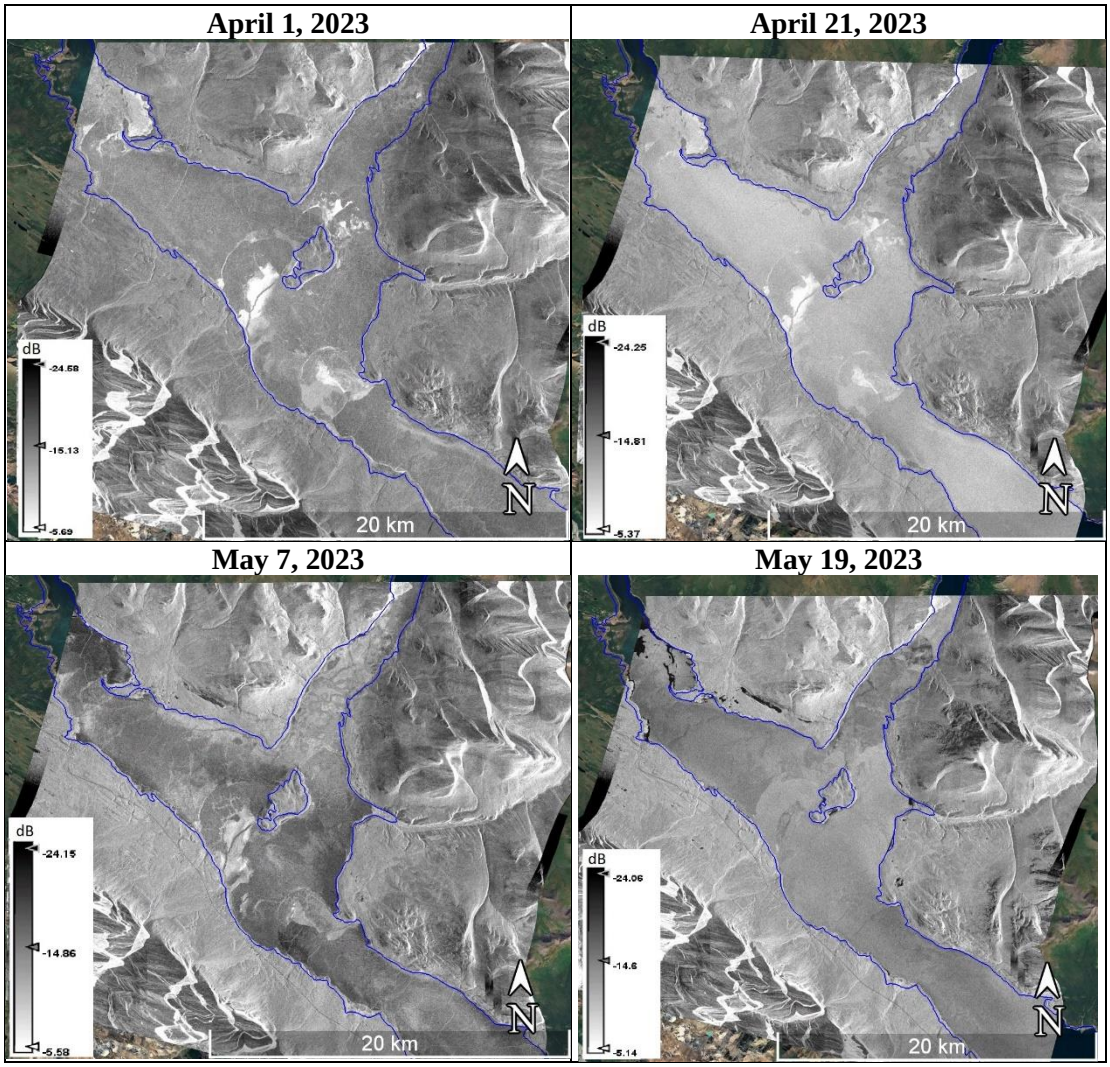


Figure 2. Backscatter evolution during the spring melt over Kluane Lake in 2023, derived from RCM data and overlaid on a Google Earth satellite image.

3.3.1 Algorithmic Approaches for Detecting Lake Ice Phenology

The evolution of backscatter during the lake ice cycle is marked by distinct patterns, including two key drops in backscatter: one during freeze-onset and another during melt-onset. These changes in backscatter have been investigated with SAR systems at different frequencies such as C-band (Jeffries et al., 1996; Geldsetzer et al., 2010; Surdu et al., 2015; Murfitt et al., 2018; Murfitt & Duguay, 2020) or Ku-band (Howell et al., 2009), as well as at different latitudes including Central Ontario (Murfitt et al., 2018), Arctic and sub-Arctic Lakes in Canada (Duguay et al., 2002; Geldsetzer et al., 2010; Surdu

et al., 2015; Murfitt & Duguay, 2020), and Alaska (Jeffries et al., 1994; Surdu et al., 2015) . These studies have demonstrated the effectiveness of SAR in capturing the complex dynamics of lake-ice phenology across various regions and environmental conditions.

One of the most widely used methods for detecting backscatter changes in lake ice monitoring is the threshold-based algorithm. This approach applies predefined thresholds to backscatter values to identify significant changes that correspond to key ice phenology events. For example, studies by Geldsetzer et al., (2010) used backscatter coefficients (σ°) from HH and HV polarizations of RADARSAT-2 imagery over the shallow, freshwater lakes in the Old Crow Flats (YT), Canada. A considerable decrease in HH backscatter was observed when the mean daily air temperature rose above 0°C, marking melt onset due to microwave absorption by the wet snow cover. This method proved highly effective, showing an accuracy rate of over 81% before the ice breakup, and between 66% and 97% during the breakup period. This general application of tracking backscatter evolution with thresholds to identify phenological events was also applied with success by Surdu et al., (2015) and Murfitt (2018) similarly utilizing a considerable drop in backscatter to represent the timing of melt-onset, and an overall rise in backscatter representing freeze-onset. Consistent across all studies utilizing a threshold-based approach, extracting the timing of freeze-onset presented greater difficulty compared to melt-onset, with mean absolute errors of up to 26 days for Surdu et al., (2015) and 2.5 – 10 days for Murfitt et al., (2018). Conversely, much lower mean absolute errors were reported for melt-onset (6 and 1.5 – 7.1 days, respectively).

While the threshold-based approach provided valuable insights into lake ice phenology, its over-sensitivity to minor and short-term backscatter changes poses a limitation (Murfitt et al., 2018). Additionally, there are certain limitations, particularly concerning the potential for high temporal and inter-lake variability in backscatter, wind effects on HH backscatter, and the challenge of distinguishing between melt ponds and open water during the initial stages of lake ice breakup (Geldsetzer et al., 2010). Moreover, these methods can be constrained by temporal gaps in Synthetic Aperture Radar (SAR) acquisitions, which can lead to inaccuracies in identifying ice phenology events (Murfitt & Duguay, 2020). This limitation results from the threshold-based approach's reliance on the detection of significant changes in the backscatter signal, which might be masked or interpreted incorrectly when successive SAR images are unavailable, especially during times of rapid ice formation or melt (Murfitt & Duguay, 2020).

Murfitt and Duguay (2020) further refined these approaches by investigating Lake Hazen's ice phenology using Sentinel-1 SAR imagery at C-band, in HH polarization, from 2015 to 2018. Two methods were applied: the first difference method and the Otsu segmentation method. The first difference method identifies ice-on and ice-off events by calculating pixel-by-pixel changes in backscatter intensity between consecutive SAR images, effectively capturing abrupt transitions during phenological events. On the other hand, the Otsu segmentation method uses a histogram-based approach to determine an optimal threshold that segments SAR images into two classes—ice and water—by maximizing the variance between them. The Otsu method provided smoother classifications, while the first difference method excelled in capturing localized ice dynamics. Validation against visual interpretations of Sentinel-1 images showed mean errors of 3–10 days for the first difference method and 2–10 days for the Otsu method. Together, these methods highlighted the potential of high-density SAR imagery for reliable lake ice monitoring in the Arctic.

Before the launch of RCM, Van Der Sanden & Geldsetzer, (2015) provided important information into CP's use for lake ice breakup monitoring, offering a glimpse into the future applications of RCM CP data. The study developed a CP-based approach, CP_LakeIceBC, for classifying breaking ice and open water, achieving classification accuracies ranging from 73.2% to 99.1% for breaking ice and 60.8% to 99.5% for open water. Drawing from previous research that mainly used HH or HV polarization from RADARSAT-2 or Sentinel-1 and simulated CP data to monitor lake ice, this thesis research presents a differencing method by using compact polarimetry (CP) data from RCM. This approach aims to understand the strength and potential limitation of the compact polarimetry of RCM in capturing lake ice phenology over subArctic lakes in Canada and the identification of key lake ice events.

3.4 Compact Polarimetric SAR

Compact polarimetric (CP) synthetic aperture radar (SAR) has become an essential tool in cryospheric research, particularly for monitoring the seasonal dynamics of lake, sea, and river ice. Unlike traditional dual-polarized or fully polarimetric (FP) SAR systems, CP SAR offers a practical balance between comprehensive target characterization and wide-area coverage (Raney, 2007). The RADARSAT Constellation Mission (RCM) has played a pivotal role in advancing this technology, providing operational CP SAR data to address diverse environmental monitoring needs (Charbonneau et al., 2010).

The key feature of CP SAR is its hybrid-polarity architecture, which transmits circular polarization and receives orthogonal linear polarizations. This setup allows the derivation of key polarimetric parameters, such as the Stokes vector components (Raney et al., 2021), which provide insights into the scattering mechanisms within different ice types. CP SAR technology offers polarization modes such as RH (Right Circular Transmit, Horizontal Receive), RV (Right Circular Transmit, Vertical Receive), RR (Right Circular Transmit, Right Circular Receive), and RL (Right Circular Transmit, Left Circular Receive).

The RH and RV polarizations are key components of the compact polarimetric (CP) SAR architecture used in RCM. These two modes are critical for capturing the linear polarization components of the backscattered signal in hybrid-polarity SAR systems. The combination of RH and RV polarizations enables the extraction of Stokes parameters, which form the foundation for deriving polarimetric features like the degree of polarization and the circular polarization ratio (Geldsetzer et al., 2024).

RR polarization is particularly sensitive to coherent volume scattering, making it effective for detecting stable ice layers and vertically aligned ice crystals, typically found in consolidated ice structures. Conversely, RL polarization excels at capturing depolarization effects (Raney, 2007), which are more prevalent in heterogeneous ice conditions during transitional phases such as freeze-onset and melt-onset (Geldsetzer et al., 2024). These modes have the potential to enhance the understanding of ice processes by capturing complex scattering mechanisms linked to internal ice properties, including the infiltration of meltwater and the formation of slush layers.

The growing body of research utilizing Compact Polarimetric (CP) SAR highlights the value of polarimetric parameters in tracking key ice transitions. Parameters such as the circular polarization ratio (CPR) and degree of polarization (DoP) have proven particularly useful in detecting surface roughness variations, identifying ice-water interfaces, and tracking internal changes within ice layers (Charbonneau et al., 2010). CPR has been used to distinguish between smooth surfaces like open water and rougher ice surfaces (Geldsetzer et al., 2024), while DoP provides insights into the dominance of specific scattering mechanisms in different ice conditions (Dabboor & Shokr, 2021).

These capabilities have been further demonstrated in sea ice research, where CP SAR has been effective in detecting seasonal transitions such as freeze-up, breakup, and changes in ice thickness (Zhang et al., 2016; Nasonova et al., 2018). Research by Geldsetzer et al. (2015) showed that by capturing both surface roughness and internal structural changes, CP SAR parameters can help

identify stable ice layers during freeze-up and meltwater infiltration during the onset of melting. This ability to track both surface scattering and subsurface changes makes CP SAR a powerful tool for monitoring ice phenology across various cryospheric environments.

These studies, while focused on sea ice, have laid the groundwork for extending CP SAR techniques to freshwater lake ice, where similar scattering mechanisms are observed. However, lake ice dynamics present distinct challenges, including shallower water bodies, greater variability in snow cover, and higher sensitivity to atmospheric conditions, which influence the radar's interaction with the ice surface and subsurface layers. The ability of CP SAR to detect subsurface features, such as air bubble density within the ice, has proven particularly valuable in lake ice studies, providing critical insights into freeze-onset, melt-onset, and mid-season transitions (Dabboor & Shokr, 2021).

This study employed the Right Circular Transmit, Vertical Receive (RV) polarization mode in the first difference method to remain consistent with previous studies on lake ice phenology, which have predominantly used backscatter intensity in linear received polarization modes (HH and HV). The decision to use RV polarization mode ensured comparability with prior research methodologies, while the analysis of four key Compact Polarimetric (CP) parameters—circular polarization ratio (CPR), degree of polarization (DoP), Alpha Angle, and Relative Phase—allowed for a more detailed examination of lake ice transitions. Each of these parameters captured different aspects of ice scattering behavior, providing insights into both surface roughness variations and subsurface changes during critical phases such as freeze-onset and melt-onset.

Chapter 4

Evaluating the RADARSAT Constellation Mission Compact Polarimetric Capabilities in Monitoring Sub-Arctic Lake Ice Dynamics

4.1 Introduction

Lake ice is an important component of the cryosphere, influencing local weather, climate, and providing nutrient cycling and habitat within various ecosystems. Monitoring lake ice phenology, including the timing of freeze-up and break-up events, provides valuable insights into climate variability and change (Ménard et al., 2002; Howell et al., 2009). Accurate lake ice monitoring helps to understand the impacts of temperature fluctuations on ice dynamics, which is crucial for hydrological studies, climate change modeling, and the management of freshwater resources (Duguay et al., 2006).

In recent years, remote sensing technology, particularly Synthetic Aperture Radar (SAR), has significantly advanced our ability to monitor lake ice phenology. SAR's ability to acquire data regardless of weather conditions or daylight, combined with its sensitivity to the structural properties of ice, makes it an invaluable tool for tracking freeze-up and break-up events. SAR backscatter evolution throughout the ice cycle provides valuable indicators of ice growth (Jeffries et al., 1994; Duguay et al., 2002).

While SAR backscatter has been highly effective in capturing the overall dynamics of lake ice (Duguay et al., 2002; Geldsetzer et al., 2010; Surdu et al., 2015; Murfitt & Duguay, 2020; Murfitt et al., 2018; Howell et al., 2009), extracting CP variables provides the potential for a more nuanced understanding of specific ice stages, particularly during transitions like freezing and melting. CP parameters offer additional insights into the physical and dielectric properties of ice, complementing the backscatter data by distinguishing between different scattering mechanisms (Dabboor & Shokr, 2021). This integration enhances our ability to accurately monitor lake ice phenology and capture subtle changes that may be less visible through backscatter alone. This additional information is critical for differentiating between ice types, such as smooth new ice, rougher mature ice, and the complex ice-water interactions present during the melt season.

This study builds on previous efforts to monitor lake ice using SAR by exploring the utility of compact polarimetric (CP) data from RADARSAT Constellation Mission (RCM). Through backscatter analysis and studying the sensitivity of CP variables, this research seeks to evaluate how well RCM can

capture the nuances of lake ice phenology in sub-Arctic lakes in Canada. By analyzing CP data, the study aims to identify the key phenological events—such as the onset of freezing and melting—and assess the strengths and limitations of RCM compact polarimetry in detecting these events under different environmental conditions. This is the first study that the authors are aware of to observe ice phenology using RCM CP parameters.

4.2 Study Area

This study focuses on three distinct sub-Arctic lakes in Canada, each chosen for their unique morphometric or geographical characteristics which provide a diverse context for understanding the variable responses of lake ice to climatic conditions and assessing lake ice phenology using RADARSAT Constellation Mission (RCM) data. The selection of these lakes allows for a detailed examination of how regional differences affect lake ice dynamics and helps to understand the behavior of lake ice in sub-Arctic regions.

Kluane Lake, Yukon Territory: The first selected study area for this research is Lhù'ààn Mân (Kluane Lake), situated in the southwestern Yukon Territory (61.283°N, 138.75°W), spans an area of 408 km² and has a maximum length of 71.6 km and a mean depth of 31 m (Figure 3). The lake's deepest point reaches approximately 91 m (Asselstine et al., 2013). Historically, Kluane Lake received its waters from the A'ay Chu (Slims River), originating from Kaskawulsh Glacier meltwater. Recent glacier retreat attributed to climate change, have redirected this meltwater to the Kaskawulsh River, highlighting the tangible effects of climate change on geomorphology and hydrology and the importance of studying the lake. Changes in the ice cover duration, water levels, and glacial melt inputs are closely monitored to assess the effects of warming temperatures.

In Kluane Lake, two study sites were selected to maximize temporal resolution from the available acquisitions. In Study Site 1, backscatter analysis was conducted for the overlap area of two orbits of RCM acquisitions for two melt periods (spring 2023 and spring 2024) and one freeze period (fall to winter 2023). Additionally, compact polarimetric parameter analysis was performed from October 2023 to May 2024. In Study Site 2, compact polarimetric parameter analysis was also conducted for the same period (October 2023 to May 2024). Although backscatter analysis was carried out for Study Site 2 as well, the results are not discussed in this study due to the lower temporal resolution.

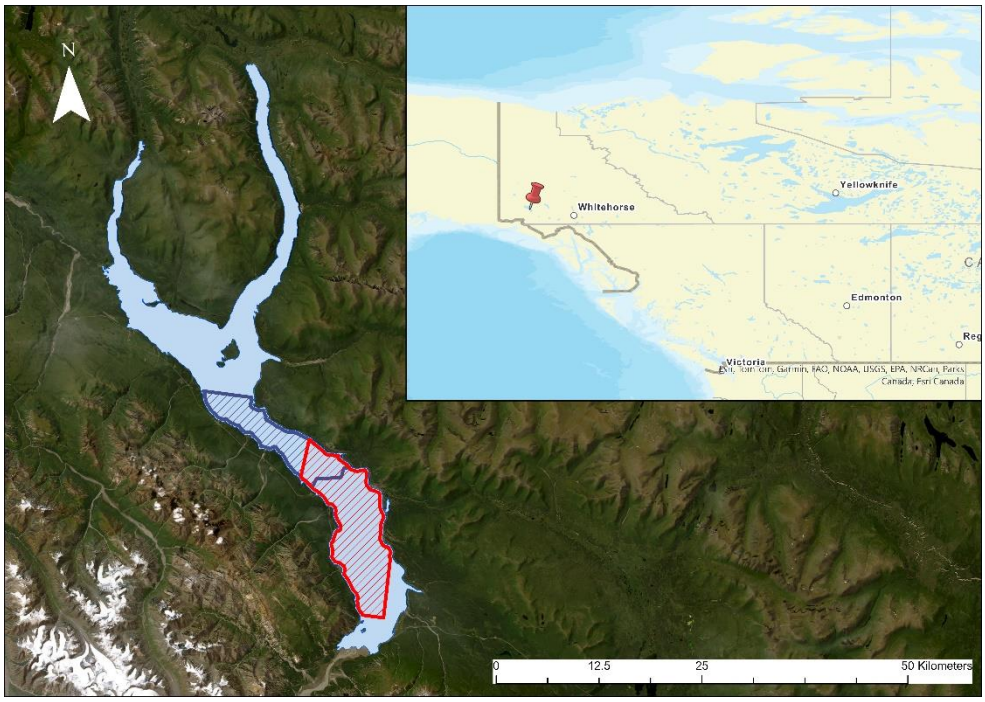


Figure 3. Kluane Lake, Yukon Territory, Canada (61.276108°, -138.751161°); Study Site 1 and Study Site 2 are shown in blue and red hatched polygons (respectively).

Ryan Lake and Landing Lake, Northwest Territories: Ryan and Landing lakes, located in the Northwest Territories near the Yellowknife region (Figure 4), offer distinctive contrasts in morphometry and depth when retrieving ice phenology from small lakes in sub-Arctic freshwater ecosystems. Ryan Lake (62.585°N, 114.367°W), with its considerable depth of 91 meters, contrasts noticeably with the shallower Landing Lake (62.559°N, 114.411°W), which has an average depth of just 4.3 meters. Despite these differences in depth, both lakes have similar surface areas and share a common annual cycle of freezing from October to April. This makes them excellent subjects for the study of ice phenology, particularly the patterns of freeze-up and break-up extracted from RCM.

These lakes are situated within the Baker Creek Research Watershed and play a crucial role in the local hydrology and are key sites for environmental monitoring (Spence & Hedstrom, 2018). The presence of permafrost and a variety of soil types contributes to complex hydrological dynamics, which are captured through extensive data collection efforts, including hydrometeorological and streamflow measurements at various points around the lakes. Monitoring efforts at Ryan and Landing Lake are integral to understanding broader environmental trends within the watershed (Spence & Hedstrom, 2018). Data from climate towers and other sensors around Landing Lake, for instance, help researchers

track changes in meteorological conditions and their impacts on the watershed's ecology and hydrology. Similarly, Ryan Lake's deeper waters offer a comparative depth for studying how lake stratification and water column dynamics in sub-Arctic lakes respond to seasonal and interannual climatic variations (Spence & Hedstrom, 2018).

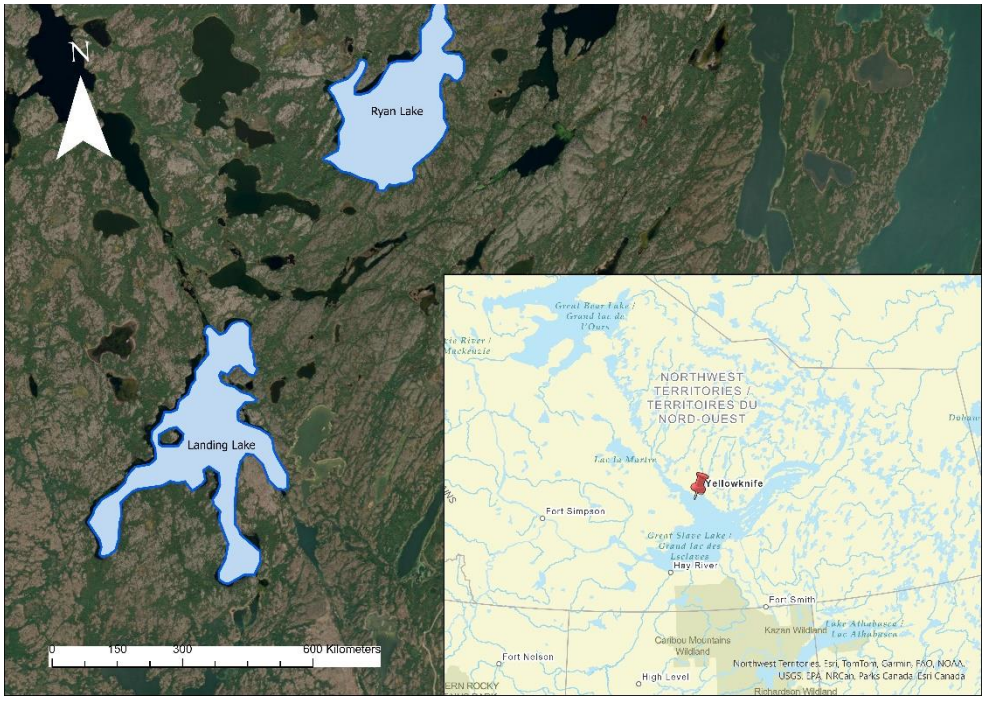


Figure 4. Ryan Lake and Landing Lake, Northwest Territory, Canada

4.3 Data

4.3.1 RADARSAT Constellation Mission

The RADARSAT Constellation Mission (RCM) consists of three identical satellites, each 32 minutes apart at an altitude of 600 km, providing efficient daily coverage of Canada and 90% of the world's surface. Each satellite is equipped with a Synthetic Aperture Radar (SAR) and an Automatic Identification System (AIS) for ships. While similar to RADARSAT-2, the RCM SAR system features a C-Band antenna with a 100 MHz bandwidth and four regular polarization modes (Figure 5). A significant improvement is the introduction of circularly polarized transmissions for higher-order polarimetric modes, offering enhanced polarization isolation. Compact polarimetry (CP), where the signal is transmitted as circular polarization (Right or Left, Figure 6) and received as linear (Horizontal or Vertical), retains phase information and balances swath coverage with polarimetric capabilities,

making it ideal for various remote sensing applications, including soil moisture estimation, crop identification, ship detection, and sea-ice classification (Charbonneau et al., 2010). CP-SAR is particularly valuable for lake ice monitoring, providing enhanced target information and broader spatial coverage than conventional systems, making it an efficient tool for data collection and detailed target characterization (Dabboor & Shokr, 2021). This study uses high to very high-resolution (16 to 5m) RCM images acquired in compact polarimetry as the primary data source.

Murfitt and Duguay (2021) conducted a 30-year review of lake ice studies in 2021, describing the various synthetic aperture radar (SAR) satellite sensors utilized in such studies spanning from 1971 to 2020. Table 1 shows the diversity of frequency, polarization, spatial and temporal resolution of these sensors as well as their operating period. Numerous studies have used RADARSAT-2 images to study lake ice phenology (Howell et al., 2020; Murfitt et al., 2018; Hoekstra et al., 2020; Surdu et al., 2015), but considering that the RCM was launched in 2019, there have been limited studies using RCM imagery in compact polarimetry to monitor lake ice thickness, and none for the timing of phenological events.

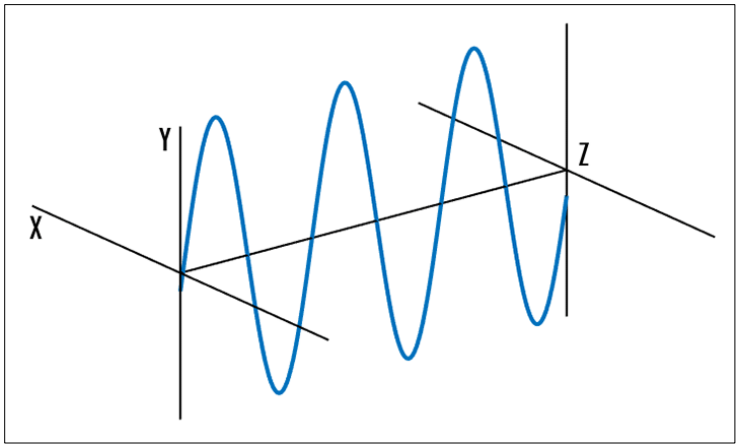


Figure 5. The most common polarization technique for spaceborne radar systems is linear polarization, in which the electric field of light is confined to a single plane along the direction of propagation.

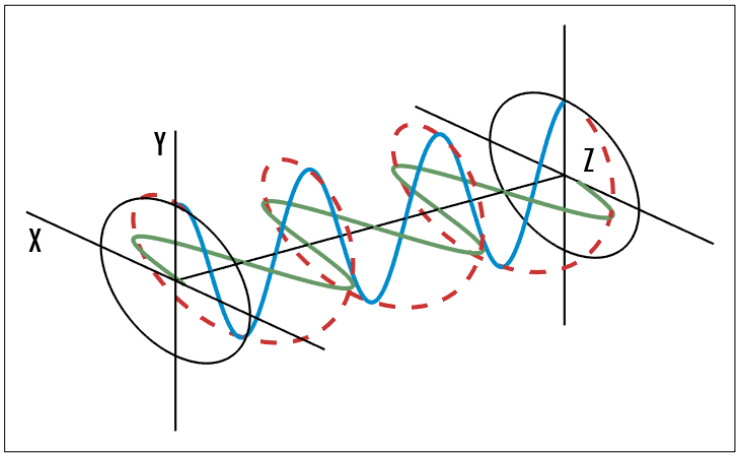


Figure 6. In the compact polarization technique, light's electric field has two equal linear components perpendicular to each other. They differ in phase by π/2 (90 degrees), causing the electric field tip to rotate in a circle around the direction of propagation. The wave is termed left- or right-hand circularly polarized based on this rotation direction.

Table 1. The diversity of SAR systems for lake ice research (Murfitt & Duguay, 2021)

Missions		Operating Period	Band	Polarizations	Repeat Cycle (days)	Pixel Spacing (m)
European Space Agency	ERS-1	1991–2000	C-band	VV	35	12.5
	ERS-2	1995–2011	C-band	VV	35	12.5
	ENVISAT ASAR	2002–2012	C-band	VV + HH/HH + HV/VV + VH	35	12.5–1000
	Sentinel-1	2014–present	C-band	HH + HV/VV + VH	12	1.5–49
Canadian Space Agency	RADARSAT-1	1995–2013	C-band	HH	24	4.6–50
	RADARSAT-2	2007–present	C-band	Fully Polarimetric	24	0.5–50
	RADARSAT Constellation Mission	2019–present	C-band	Fully Polarimetric /Circular Polarization	4	1–100
German Aerospace Center	TerraSAR-X	2007–present	X-band	Fully Polarimetric	11	0.2–15
	TanDEM-X	2010–present	X-band	Fully Polarimetric	11	0.2–15

Japan Aerospace Exploration Agency	JERS-1	1992–1998	L-band	HH	44	18
	PALSAR	2006–2011	L-band	Fully Polarimetric	46	6.25–500
	PALSAR-2	2014–present	L-band	Fully Polarimetric /Circular Polarization	14	1–300
Italian Space Agency	COSMO-SkyMed	2007–present	X-band	HH/VV/HV/VH	16	1–100
NASA	SeaSat	June 1978–Oct. 1978	L-band	HH	17	25
Argentina National Space	SAOCOM-1	2018–present	L-band	HH + HV/VV + VH	16	10–100

4.3.2 Landsat Imagery

Landsat-9, the latest satellite in the Landsat series, was launched by NASA and the United States Geological Survey (USGS) on September 27, 2021. It continues the mission of its predecessors by providing critical Earth observation data, essential for environmental monitoring, climate change studies, and resource management. Among its advanced sensors, the Thermal Infrared Sensor 2 (TIRS-2) plays an important role in capturing thermal data, specifically through its thermal bands 10 and 11 (Sobrino et al., 2004).

The TIRS-2 on Landsat-9 includes two thermal bands designed to measure Earth's surface temperature with high precision. These bands operate in the thermal infrared part of the electromagnetic spectrum, crucial for detecting heat energy emitted by the surface. Band 10 captures thermal infrared radiation within the wavelength range of 10.60 to 11.19 micrometers. Band 11 captures thermal infrared radiation within the wavelength range of 11.50 to 12.51 micrometers. These bands are particularly useful for applications requiring surface temperature measurements, such as monitoring water bodies, assessing vegetation health, and studying urban heat islands.

The accuracy and reliability of lake ice phenology retrievals from RCM can be evaluated by comparing land surface temperature (LST) data derived from Landsat-9's thermal bands. In this study, thermal infrared data from Landsat-9 are preprocessed including radiometric calibration, atmospheric

correction, and the calculation of land surface emissivity. Radiometric calibration is the initial step in preprocessing thermal infrared data. It involves converting the raw digital numbers (DN) from the satellite sensor into radiance values. These radiance values are then transformed into brightness temperatures, which represent the temperature of the Earth's surface as seen by the satellite sensor (Chander et al., 2009).

Atmospheric correction is crucial for removing the effects of atmospheric gases and aerosols that may change the thermal infrared signals received by the satellite. This correction process ensures that the radiance values represent the true surface temperature by accounting for atmospheric interference. Emissivity is a measure of a surface's ability to emit thermal radiation and is essential for accurately determining land surface temperature (LST) (Sobrino et al., 2004). For Landsat-9, Band 10 is often used for emissivity calculations due to its high sensitivity in the thermal infrared range.

4.3.3 Planet Imagery

Planet is a leading provider of high-frequency satellite imagery and geospatial solutions. The company's fleet of small, agile satellites, known as Dove satellites, captures high-resolution images of the entire Earth on a daily basis. The Planet platform provides users with access to a vast archive of imagery, enabling the analysis of changes over time with high temporal and spatial resolution. The imagery is available through Planet's Explorer web interface. In this study, Planet's optical satellite images were used to validate the results obtained from RCM data during the melt period. Due to polar darkness in the Arctic and sub-Arctic regions, optical imagery is limited during winter. However, the high spatial resolution and daily revisit capability of Planet satellites provide a reliable way to cross-verify the accuracy of ice phenological dates detected in the study area. The calibration of Planet reflectance information is less reliable than that of Landsat, so Planet optical acquisitions are used as a qualitative sanity check in addition to LST from Landsat-9.

4.4 Methods

The methodologies applied in this research are divided into two main categories: backscatter analysis and CP parameter analysis. Backscatter analysis uses data from the 2023 break-up and freeze-up periods as well as the 2024 break-up, while polarimetric parameter analysis is based on data from the 2023 freeze-up and the 2024 melt season. Before discussing the details of each method, it is important to note that the selection of the study area in both periods was based on achieving the highest possible

temporal resolution from the available imagery. The approach used for selecting the study area for backscatter analysis is outlined in detail in the following section.

4.4.1 Study Area Selection Over Kluane Lake

The RADARSAT Constellation Mission (RCM) data provides high spatial resolution, but its temporal resolution is limited in specific areas due to the scope of RCM data coverage (Standard Coverage Maps). This limitation highlights the importance of using all available data to ensure comprehensive analysis. Images of Landing and Ryan Lakes fully capture these lakes' areas, but for the much larger Kluane Lake, the coverage is uneven, with images overlapping as shown in Figure 7.

Two distinct study sites were selected in Kluane Lake. The first site focused on analyzing backscatter data from the 2023 thaw and freeze periods and the 2024 melt season, alongside compact polarimetric parameter analysis. The second site focused on compact polarimetric parameter analysis, incorporating freeze data from 2023 and melt data from 2024. To optimize the use of the overlaid images, a point-based method was used in selecting the first study site. In this method, sample points with the highest frequency of available images were selected, rather than using the raster data directly. For the second site, the common region that appeared consistently across the largest number of acquisitions was selected. This strategy ensures that each site is analyzed with the most reliable data coverage available.

The method applied to the first study site of Kluane Lake focused on specific segments of each dataset. A 5-meter grid was established across the lake, and raster images were organized based on their availability. Sampling was conducted from all available RCM datasets at each grid point. Data tables cataloged the sampled values at each point for every date. When multiple datasets overlapped on a specific point and day, the values acquired on the same dates were averaged.

Additionally, a column indicating the count of unique data entries per point was included. The compiled data was then structured into a shapefile, categorized by the frequency of data availability, focusing on points where more than 50% of the data was accessible (Figure 8). This allowed for the delineation of areas most consistently represented in the datasets. The workflow for the first study area selection process across Kluane Lake is outlined in the flowchart presented in Figure 9.

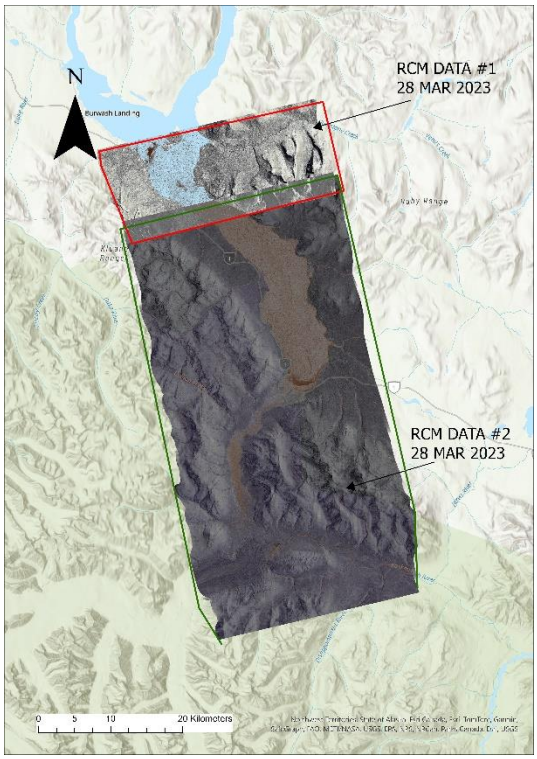


Figure 7. RCM images overlap across Kluane Lake

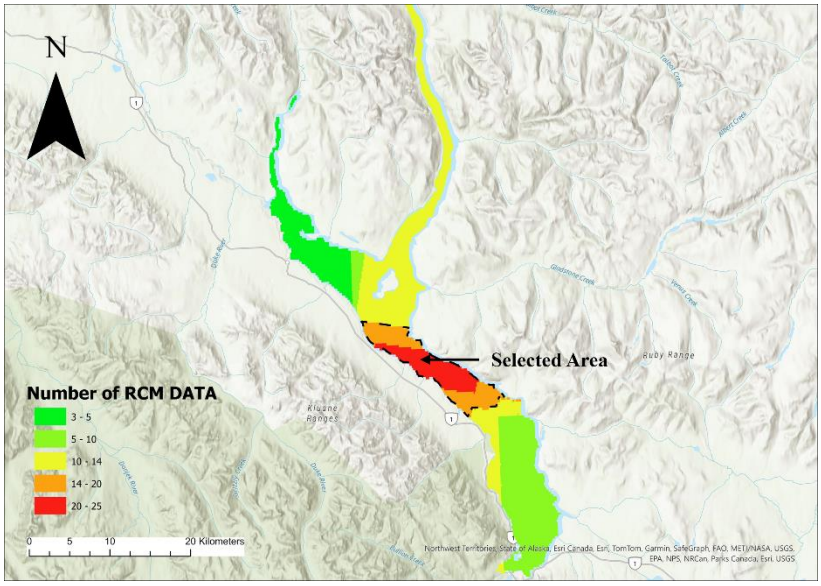


Figure 8. This map illustrates the frequency of RCM images across different sections of the lake. For the final analysis, a portion of the lake has been selected that contains images for at least half of the dates.

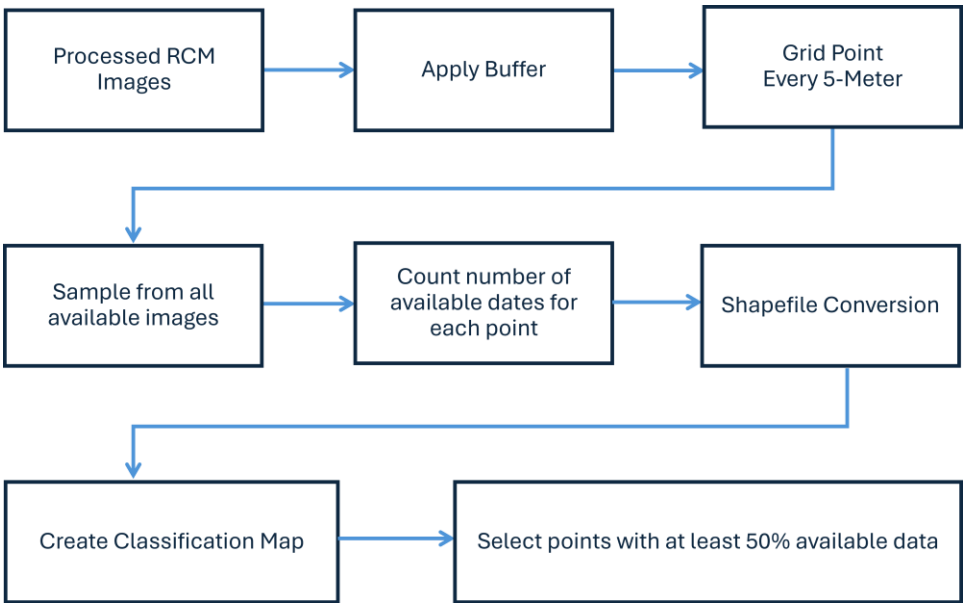


Figure 9. Workflow of the study area (Site 1) selection process across Kluane Lake

4.4.2 Backscatter Analysis

4.4.2.1 Preprocess Steps of Backscatter Analysis

For the first study area in Kluane Lake, RCM images were collected over three periods from Natural Resources Canada's Earth Observation Data Management System (EODMS, http://www.eodms-sgdot.nrcan-rncan.gc.ca). A total of 34 acquisitions were obtained between January and June 2023, 11 between September 2023 and January 2024, and 16 acquisitions between March and May 2024. These images were captured in Stripmap mode, providing a high spatial resolution of 5 meters in compact polarization mode. For Ryan Lake and Landing Lake, a total of 15 RCM Single Look Complex (SLC) acquisitions were collected from January to June 2023. These images were also captured in Stripmap mode at 16 meters resolution at C-band (5.405 GHz) compact polarization.

During preprocessing, backscatter intensity values were derived from the RCV polarization mode (Right Circular Transmit, Vertical Receive), which measures radar backscatter in response to circularly polarized signals transmitted and vertically polarized signals received. The raw RCM images were processed using the Graph Builder tool on the Sentinel Application Platform (SNAP). The primary preprocessing step involved radiometric calibration to ensure that the SAR images' pixel values

accurately reflected radar backscatter from the surface. The pixel values were retained as digital numbers (DN) without conversion to decibel power.

A multilooking process was then applied to reduce noise or "speckle" by averaging neighboring pixels (Geldsetzer et al., 2010). In addition, speckle filtering was performed using a Lee Sigma filter, which assessed pixel relationships to edge orientations using a 5 × 5 window and a 3 × 3 target window. To align all images accurately, terrain correction was executed using the GETASSE30 Elevation Model, which is a composite of four different DEM datasets: SRTM30, ACE, Mean Sea Surface (MSS) data, and the EGM96 ellipsoid. The integrated GETASSE30 dataset provides a representation of Earth's topography and sea surface elevation relative to the WGS84 ellipsoid at 30 arc-second resolution.

In the subsequent stages of preprocessing, angular dependence was mitigated by normalizing the backscatter values using Band-Math in SNAP. Cosine correction, a method based on Lambert's law of optics, is among the earliest and most widely used normalization techniques. According to Mladenova et al., (2013), the measured backscatter, denoted as $\sigma^o_{\theta_i}$, is related to the square of the cosine of the incidence angle:

$$\sigma^o_{\theta_i} = \sigma^o_0 \, cos^n(\theta_i) \qquad (4)$$

Where $n = 2$, θ_i represents the local incidence angle, and σ^o_0 is the backscatter independent of this angle. The final stage of image preprocessing involves converting the digital numbers (DN) to sigma-naught in decibels (dB):

$$Sigma0_RCV_dB = 10 * log_{10}(Sigma0_RCV) \qquad (5)$$

$$Sigma0_RCH_dB = 10 * log_{10}(Sigma0_RCH) \qquad (6)$$

Where $Sigma0_RCV$ or $Sigma0_RCH$ represents the pixel value in raw digital numbers and $Sigma0_RCV_dB$ or $Sigma0_RCH_dB$ represent the pixel value of the RCM image after converting to sigma-naught.

An inward buffer of 150 meters was applied to the Ryan and Landing Lakes polygons, and a 300-meter inward buffer was used for the Kluane Lake polygon to mitigate the potential influence of shoreline effects. All RCM images used for studying Ryan and Landing Lakes covered their entire areas; however, this was not the case for Kluane Lake due to its size.

4.4.2.2 First Difference Method

The first difference method is used to identify the occurrence of lake ice phenology events. This approach involves comparing two successive images by subtracting the backscatter values of the corresponding pixels (Murfitt & Duguay, 2020). Traditional methods involve the subtraction of consecutive rasters for implementing the first difference method. In this study, a multidimensional matrix was used for analyzing backscatter evolution to maximize data usage. The methodology begins with the creation of grid points that maintain spatial distances equal to the RCM's ground sample distance (GSD), with one point for every 5 meters. Sample points were created over Landing and Ryan Lakes and the selected area of Kluane Lake.

All preprocessed RCM data, including backscatter values in decibels (dB), are arranged as a data source. A matrix is then constructed, where each row represents a point, and the first three columns represent the Point ID, Longitude, and Latitude. Each RCM image's backscatter value is added as a column, representing specific points.

Radar signals include a certain amount of inherent noise, known as the Noise Equivalent Sigma Zero (NESZ). The NESZ is the radar backscatter level below which the radar system can't distinguish signal from noise. For RCM 5 m and 16 m resolution, the NESZ is around -19 and -25 dB respectively (Technical characteristics | Canadian Space Agency (asc-csa.gc.ca)). Since, the NESZ can interfere with detecting subtle changes in ice conditions, pixels with backscatter values below -30 dB are set to a value of 0. This serves to flag these pixels so they can be excluded from the analysis (Murfitt & Duguay, 2020).

To accurately capture variations in backscatter and reduce noise, overlapping RCM data points (pixels) observed on the same day were averaged to provide a single backscatter value for each date. The values were checked, and the non-zero average was calculated for the backscatter value of the relevant point. A matrix was constructed where each row represented a unique point and each column represented a date, except for the first three columns which contained the point ID, longitude, and latitude (Table 2).

Table 2. Final data structure matrix

Point ID	Longitude	Latitude	Date (1)	...	Date (n)
Point _1					
...					
Point_n					

To identify the significant drops in expected dates, a matrix was developed to compute differences in backscatter values in temporal order. Zero values were eliminated from the differences to enhance accuracy. The resulting matrix had one fewer column than the original date sample matrix. Any difference where either backscatter value was zero was assigned a value of zero, effectively excluding those amounts from further analysis. This ensured that noise or erroneous data did not affect the results.

Significant drops in backscatter values might not occur within a single day but instead span several consecutive days. The time series of backscatter is segmented according to the direction of the gradient, with each segment encompassing a continuous series of either decreases or increases (Figure 10). The last date of each segment is then chosen to represent that segment, capturing substantial changes in backscatter changes over time.

Backscatter differences between every two successive images are calculated cumulatively in either an ascending or descending segment. Then the largest decreases during the freeze-up and break-up periods over Kluane Lake selected area, Ryan Lake and Landing Lake are selected to create a final matrix that includes the first three columns and the first difference-determined date. This matrix is then converted to a shapefile with point geometry and subsequently transformed into a raster with a pixel resolution of 5 meters, where each pixel represents the determined date. Due to the noise, adjacent pixels in the raster may display varying dates. A 9*9 majority filter is applied to address this, selecting the most frequent date within the kernel to smooth the final results. Figure 11 illustrates the process for identifying freeze-onset and melt-onset dates using RCM images.

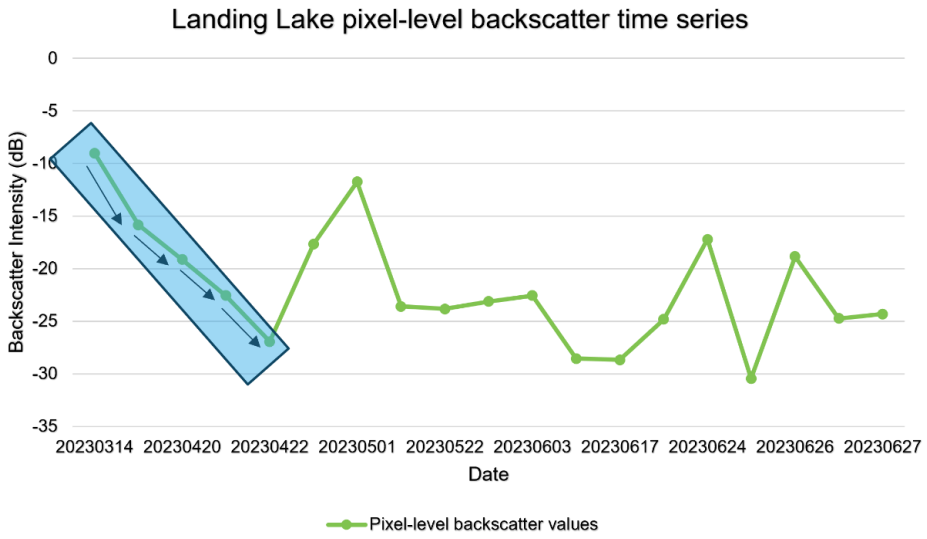


Figure 10. The time series of pixel-level backscatter values for Landing Lake from March to June 2023. This plot highlights the progression of backscatter changes over time. The figure illustrates that substantial drops in backscatter values may span several consecutive days rather than occurring within a single day.

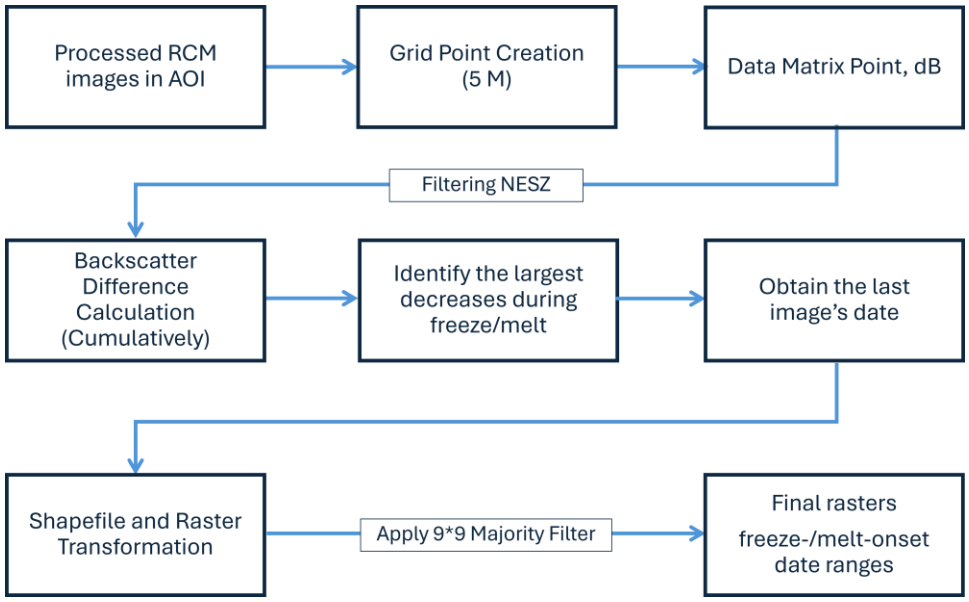


Figure 11. Workflow for Identifying freeze-onset and melt-onset Dates

4.4.3 Polarimetric Parameter Analysis

Polarimetric parameter analysis plays an important role in this research, as it helps to better understand the physical properties of lake ice. By using polarimetric parameters from RCM data, valuable insights into surface scattering patterns were obtained, which are key to distinguishing between different ice stages. In this study, data from the 2023 freeze-up period and the 2024 melt season were analyzed to examine changes in four parameters and their connection to lake ice phenology. Both Study Site 1 and Study Site 2 in Kluane Lake were examined, with preprocessing steps detailed in the following section.

4.4.3.1 Preprocess Steps of Polarimetric Parameters Analysis

Between October 2023 and May 2024, 35 and 33 RCM Single Look Complex (SLC) images were acquired for Study sites 1 and 2, respectively (http://www.eodms-sgdot.nrcan-rncan.gc.ca), offering a 5-meter spatial resolution and the average temporal resolution of 8.07 days in compact polarimetry. The largest gap between acquisitions is 32 days which occurred from October 11, 2023, to November 12, 2023. Several preprocessing steps were undertaken to ensure the accuracy and suitability of the data for polarimetric analysis. First, a multilooking process was applied to the raw RCM images to reduce speckle noise by averaging adjacent pixels. This was followed by radiometric calibration to ensure that the radar backscatter values accurately reflected surface characteristics. During this process, the data was saved as complex output, preserving both phase and amplitude information essential for polarimetric analysis. After calibration, CP parameters were calculated to evaluate the scattering mechanisms of the ice surface. Finally, terrain correction was applied using the GETASSE30 Elevation Model to ensure accurate geometric alignment of the images.

4.4.3.2 Overview of Compact Polarimetric Parameters

Compact Polarimetry provides a simplified yet powerful method for radar data analysis by transmitting circularly polarized signals and receiving linear polarizations. Compact polarimetry is particularly useful in applications like environmental monitoring, as it balances between full polarimetry and single/dual polarimetry modes, offering a good compromise between data complexity and coverage (Charbonneau et al., 2010; Dabboor & Shokr, 2021).

Compact polarimetry offers a powerful means of generating various polarimetric parameters that describe the scattering behavior of observed targets. Key among these are the Stokes parameters, which capture the polarization state of the electromagnetic waves. The Stokes vector, S, consists of four

parameters S_0, S_1, S_2, and S_3, which describes the total power of the wave and the distribution of power across different polarization states (Cloude, 2009; Woodhouse, 2012). Stokes parameters are real quantities and are expressed in terms of intensities. These parameters are calculated as follows:

- S_0 represents the total power of the scattered wave and is defined as:

$$S_0 = |E_{RH}|^2 + |E_{RV}|^2 \quad (7)$$

Where E_{RH} and E_{RV} are the right circular transmissions with horizontal and vertical receptions, respectively. This parameter gives the overall intensity of the signal, combining both polarized and unpolarized components.

- S_1 indicates the difference in power between the horizontally and vertically polarized components:

$$S_1 = |E_{RH}|^2 - |E_{RV}|^2 \quad (8)$$

This parameter is essential for identifying the dominant polarization, with positive values showing horizontal polarization dominance.

- S_2 provides information on the correlation between the horizontally and vertically polarized components in terms of phase:

$$S_2 = 2.Re(E_{RH}.E_{RV}^*) \quad (9)$$

Where E_{RV}^* is the complex conjugate of E_{RV}. It quantifies the real part of the correlation between the two polarization states, offering insights into the coherence of the scattering process.

- S_3 captures the phase difference between the horizontal and vertical components, focusing on the imaginary part of the correlation:

$$S_3 = 2.Im(E_{RH}.E_{RV}^*) \quad (10)$$

This parameter is related to the circularity of the polarization and is useful for understanding the scattering mechanism's geometry.

- The intensity of the polarized part of the wave is given by:

$$I_{polarized} = \sqrt{S_1^2 + S_2^2 + S_3^2} \quad (11)$$

- And the total intensity of S_0 is:

$$S_0 = I_{polarized} + I_{unpolarized} = \sqrt{S_1^2 + S_2^2 + S_3^2} + I_{unpolarized} \quad (12)$$

Using these Stokes parameters, additional polarimetric metrics are derived. The Degree of Polarization (DoP) quantifies the fraction of the total scattered signal that remains polarized and provides valuable insights into the scattering mechanisms of different surfaces or media. It is calculated as:

$$DoP = \frac{\sqrt{S_1^2+S_2^2+S_3^2}}{S_0} \quad (13)$$

where DoP values range between 0 and 1. Higher values, closer to 1, indicate highly polarized waves, suggesting coherent scattering from smooth surfaces, such as calm water or flat ice, where radar waves reflect in a specular manner, maintaining the polarization of the transmitted signal (Geldsetzer et al., 2015). In contrast, lower DoP values point to depolarized scattering caused by rough or volumetric scatterers, where multiple reflections and scattering events change the polarization state of the radar signal (Geldsetzer et al., 2015).

Following the degree of polarization, the Degree of Depolarization (DoD) measures how much of the signal is unpolarized after scattering. It is inversely related to DoP and can be expressed as:

$$DoD = 1 - DoP \quad (14)$$

A higher DoD indicates a significant loss of polarization coherence, which is typical for scattering from rough or complex surfaces like vegetation or ice ridges.

The Circular Polarization Ratio (*CPR*) is a key parameter used to assess surface scattering properties and distinguish between different surface textures and materials. It compares the power of right-hand circular polarization (RR) to left-hand circular polarization (RL) and is mathematically defined as:

$$CPR = \sigma\sigma^0_{RR/RL} = \frac{S_0-S_3}{S_0+S_3} \quad (15)$$

CPR is commonly used in radar remote sensing to identify variations in surface roughness. Higher CPR values typically indicate rougher surfaces that scatter more energy in the same circular polarization

as the transmitted wave, while lower values suggest smoother surfaces that scatter energy more uniformly (Charbonneau et al., 2010; Geldsetzer et al., 2015). By analyzing CPR, surface characteristics such as texture, roughness, and dielectric contrasts can be better understood, which is critical in studies of ice, water, and other natural surfaces.

The Relative Phase (δ), between right-hand circular polarization (RH) and left-hand circular polarization (RV) is a valuable parameter in compact polarimetry for understanding dominant scattering mechanisms across different surface conditions. It measures the phase difference between the two received polarizations and is calculated as:

$$\delta = \tan^{-1}\left(\frac{S_3}{S_2}\right) \quad (16)$$

Relative Phase provides insights into changes in scattering mechanisms, including surface roughness and subsurface structure. Unlike parameters such as the CPR or DoP, δ is less influenced by environmental variations or incidence angle changes, making it particularly stable under varying conditions (Charbonneau et al., 2010). This stability makes δ a reliable indicator of underlying ice integrity, helping to characterize internal ice properties rather than surface roughness alone. It is particularly useful for identifying transitions between surface scattering and volume scattering, which are critical for understanding ice phenology events.

The Alpha Angle (α) is a parameter from the Cloude-Pottier decomposition (Cloude & Pottier, 1996), which is widely used in polarimetric SAR data analysis. It is derived from the eigenvalues of the coherency matrix and indicates the type of scattering present (Woodhouse, 2012). The alpha angle typically ranges between 0° and 90° and is calculated as:

$$\alpha = \frac{1}{2}\tan^{-1}\left(\frac{\sqrt{S_1^2+S_2^2}}{\pm S_3}\right) \quad (17)$$

$\alpha \approx 0°$: Low values indicate surface scattering, characterized by single-bounce interactions where the radar signal reflects directly off the surface, such as newly formed ice.

$\alpha \approx 45°$: Intermediate values suggest volume scattering, common in snow-covered ice or rougher ice conditions where the radar waves penetrate and scatter within the ice.

$\alpha \approx 90°$: High values represent double-bounce scattering, which occurs when the radar signal bounces off two surfaces, such as ice ridges, rough ice, or areas with surface irregularities where the radar wave reflects between surfaces.

The Degree of Circularity (χ), measures how much the polarization state of the wave resembles circular polarization, and is calculated as:

$$\chi = 0.5 \tan^{-1}\left(\frac{S_3}{\sqrt{S_1^2+S_2^2}}\right) \quad (18)$$

This parameter typically ranges from -45° to 45°, where values near 0 represent linear polarization, and values near ±45 indicate circular polarization.

The Degree of Ellipticity (ψ) or Polarization Angle, describes the shape of the polarization ellipse.

$$\psi = 0.5 \tan^{-1}\left(\frac{S_2}{S_1}\right) \quad (19)$$

This parameter measures the ellipticity of the polarization, with values closer to 0 indicating linear polarization, and values closer to ±90° indicating elliptical or circular polarization.

The Linear Polarization Ration (*LPR*) shows how circular is the receiving wave and what is the sense of the rotation (left or right), and is calculated as:

$$LPR = \frac{S_0-S_1}{S_0+S_1} \quad (20)$$

Finally, the Conformity Coefficient measures how closely the observed radar backscatter matches a given scattering type, whether it be surface, double-bounce, or volume scattering (Truong-Loi, M.-L et al., 2009). For surface scattering, where the horizontal and vertical backscatters are correlated and the phase difference is close to zero, the Conformity Coefficient tends to be positive, with values close to 1. For double-bounce scattering, where the horizontal and vertical polarizations are out of phase by approximately 180°, the Conformity Coefficient will be negative, approaching -1. For volume scattering, where the horizontal and vertical channels are weakly correlated and scattered randomly, the Conformity Coefficient will have intermediate values close to 0 (Truong-Loi, M.-L et al., 2009).

In this study, we will focus on analyzing the results of a few key CP parameters from Oct 2023 to May 2024 for Kluane Lake, including the Degree of Polarization (DoP), Circular Polarization Ratio (CPR), Relative Phase, and Alpha Angle. These parameters have been selected due to their significance

in understanding the scattering mechanisms of the observed surfaces. The behavior of other CP parameters will be presented in Appendix A for further reference and comparison. This comprehensive approach allows us to focus on the most relevant parameters for lake ice phenology, while still providing supplementary information on other metrics that might enhance our knowledge.

4.4.4 Preprocessing Landsat Images for Land Surface Temperature (LST) Calculation

In this study, Land Surface Temperature (LST) was used to validate the estimated freeze and melt dates derived from RADARSAT Constellation Mission (RCM) data. The LST values were calculated using Landsat 8 and 9 imagery, specifically focusing on the thermal infrared (TIR) bands. The Reference Channel Method was employed, a widely used approach for calculating LST from satellite TIR data. This method is particularly suitable when a single thermal band is used for atmospheric corrections and surface emissivity calculations.

The LST calculation process is a multi-step procedure that ensures the derived temperature values accurately reflect surface conditions in degrees Celsius. The steps include radiometric calibration, atmospheric correction, and emissivity normalization. Each step addresses different aspects of the raw satellite data, accounting for radiometric properties, atmospheric effects, and surface emissivity variations.

4.4.4.1 Radiometric Correction

Radiometric correction transforms raw digital numbers (DN) into Top-of-Atmosphere (TOA) radiance. This process is essential for ensuring the input data accurately reflects the sensor's recorded radiance (Chander et al., 2009).

$$L_\lambda = M_L \cdot Q_{cal} + A_L \quad (21)$$

Where L_λ is TOA spectral radiance (W/m²·sr·μm), M_L is Radiance multiplicative scaling factor (from metadata), Q_{cal} is Quantized and calibrated pixel value (DN), and A_L is radiance additive scaling factor (from metadata). This transformation ensures that the radiance values align with the spectral sensitivity of the satellite sensor.

4.4.4.2 Thermal Atmospheric Correction

Atmospheric correction is performed to remove the effects of atmospheric transmissivity (τ), upwelling radiance (L_{UP}), and downwelling radiance (L_{DOWN}). These corrections ensure that the derived radiance

values accurately represent surface-emitted radiance. The corrected surface radiance (L_{ST}) is calculated using (Jimenez-Munoz & Sobrino, 2010):

$$L_{ST} = \frac{L_{\lambda} - L_{UP}}{\tau} - \frac{(1-\tau)\,.\,L_{DOWN}}{\tau} \quad (22)$$

This step is critical for isolating surface contributions and improving the accuracy of LST retrievals.

4.4.4.3 Brightness Temperature Calculation

After atmospheric correction, brightness temperature TB is calculated using the Planck function. This step assumes the surface behaves as a blackbody emitter (Chander et al., 2009):

$$T_B = \frac{K_2}{\ln\left(\frac{K_1}{L_{ST}} + 1\right)} \quad (23)$$

4.4.4.4 Emissivity Normalization

Surface emissivity (ϵ) represents the efficiency of a surface in emitting thermal energy relative to a perfect blackbody. Emissivity values are derived using the Normalized Difference Vegetation Index (NDVI) or land cover classifications. The normalized emissivity correction is applied to calculate the final LST using:

$$LST_{Corr} = \frac{T_B}{1 + \left(\frac{\lambda T_B}{C_2}\right).ln\epsilon} \quad (24)$$

Where LST_{Corr} is Corrected temperature, λ is the central wavelength of the TIR band (10.9 μm for Band 10), $C_2 = h.c/K$, a constant derived from Planck's law, and ϵ is the surface emissivity (based on NDVI or land cover type). Finally, the corrected temperature in Kelvin is converted to degrees Celsius ($LST_{^\circ C}$) using:

$$LST_{^\circ C} = LST_{Corr} - 273.15 \quad (25)$$

4.5 Results

This study examines the ice conditions in three different lakes using the capabilities of RCM imagery. Each lake was selected for distinct reasons based on its unique characteristics. Kluane Lake was chosen for its large size, Ryan Lake for its small area and significant depth, and Landing Lake as a neighboring lake with a similar surface area but much shallower depth, allowing for a direct comparison with Ryan.

In this study, backscatter intensity and the First Difference method were used to assess freeze-onset and melt-onset conditions. For Kluane Lake, the melt processes in both spring 2023 and spring 2024, as well as the freeze-up process in winter 2023, were analyzed. In contrast, for Ryan and Landing Lakes, only the melt process was examined in spring 2023 due to data availability. Next, compact polarimetric parameters were evaluated and used in the analysis of ice formation and melting periods for Kluane Lake from October 2023 to May 2024.

Finally, lake surface temperature extracted from Landsat-9 imagery was used to provide additional validation for the results. Visual imagery from the Planet platform was also employed as a further validation tool in this study.

4.5.1 Freeze-onset Mapping Results

The freeze-onset map for Kluane Lake, derived from the first difference method using RCM data (Figure 12), illustrates the progression of ice formation across the designated study area during the winter of 2023. The results demonstrate that ice formation primarily initiates in the northern part of the study area, where freezing occurs earlier. Table 3 indicates that approximately 18% of the study area on Kluane froze between November 24 and December 18 and the majority of the study area freezing between Dec 3 and December 18, 2023. A minimal number of pixels indicate freezing between December 18 and January 1; this is likely due to data noise, as these pixels are distributed randomly across the study area without observable patterns.

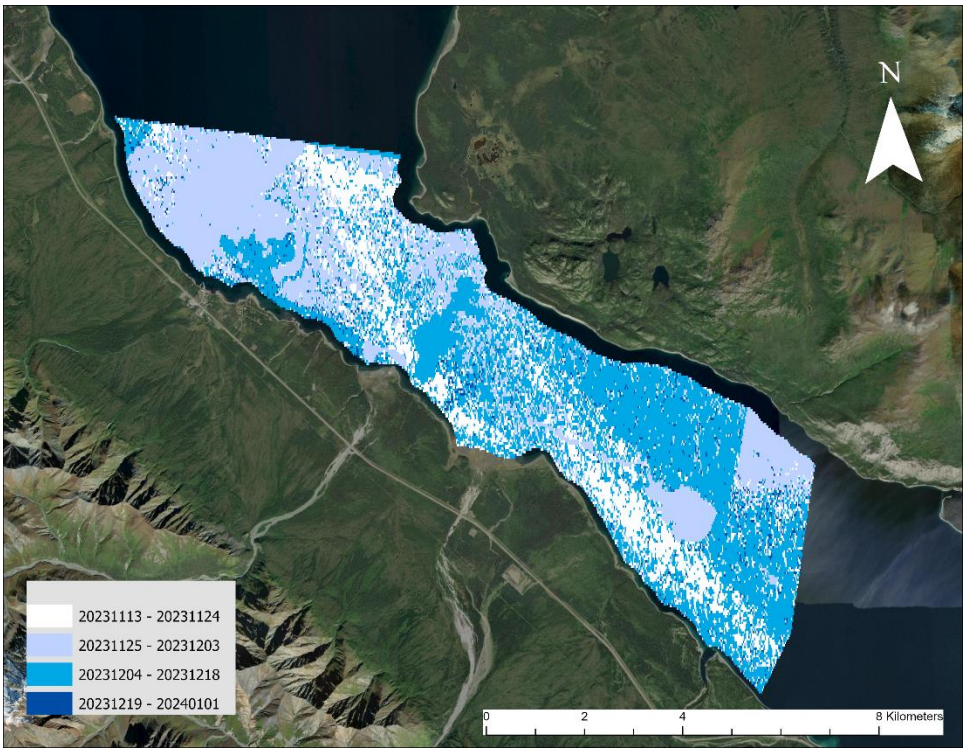


Figure 12. Spatial distribution of freeze-onset dates at Study Site 1 in Kluane Lake determined pixel by pixel using the first difference method during fall and winter 2023.

Table 3. Percentage of frozen pixels at Study Site 1 in Kluane Lake During Winter 2023, based on the first difference method

Freeze-onset interval	% Frozen Pixels
12 Nov 2023 – 24 Nov 2023	18.53
24 Nov 2023 – 3 Dec 2023	29.92
3 Dec 2023 – 18 Dec 2023	48.55
18 Dec 2023 – 1 Jan 2024	2.99

Figure 13 includes a map and two time series illustrating the backscatter intensity changes at Points A and B on Kluane Lake. According to Figure 12, the freeze-onset at Point A occurred between November 24 and December 3, whereas at Point B, it occurred between December 3 and December 18. The time series graphs in Figure 13 indicate that the largest drop in backscatter intensity for Point A was on December 2, and for Point B, it was on December 18.

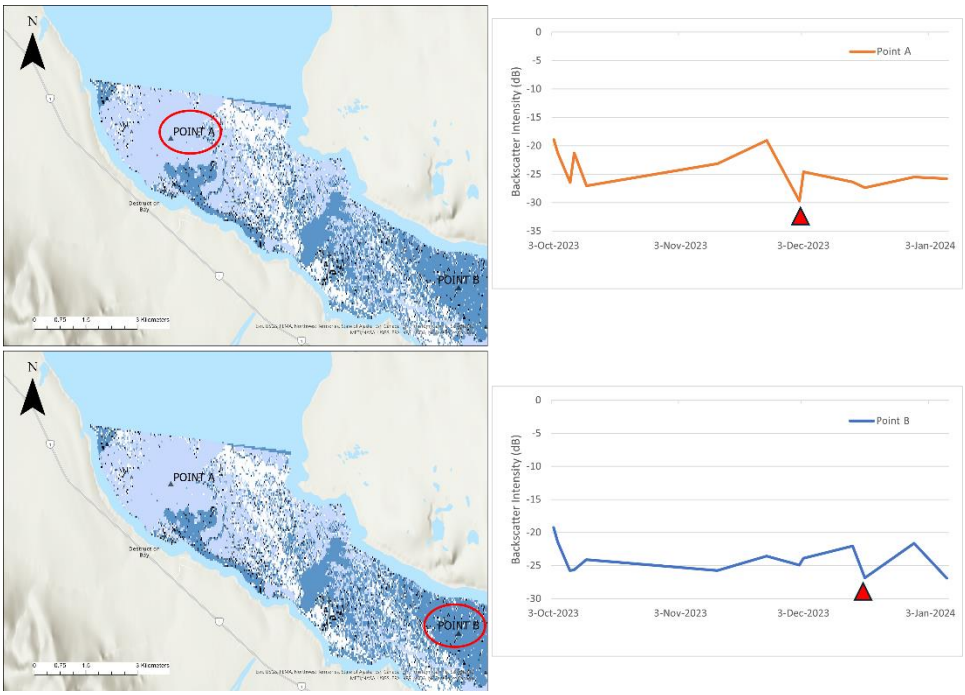


Figure 13. Backscatter variations at Points A and B on Kluane Lake, the map displays the spatial distribution of RCM image pixels over Kluane Lake, highlighting Points A and B. The time series graphs show the backscatter intensity at these points from October 2023 to January 2024.

To validate the accuracy of the retrieved freeze-onset dates, two Landsat-9 images dated November 29, 2023, and December 9, 2023, were analyzed (Figure 14). The Land Surface Temperature (LST) map from November 29 reveals that the surface temperatures of the lake ranged between -2°C and -5°C, while temperatures in the southern part of the lake varied from 0°C to 3°C. These observations are consistent with the freeze-onset patterns derived from the RCM data, confirming the onset of freezing in the colder northern regions first. By December 9, the LST map indicates that the entire study area had reached freezing conditions, with temperatures ranging between -10°C and -1°C. This overall decrease in temperature supports the RCM-derived freeze-onset map, indicating that approximately half of the pixels began freezing between December 3 and December 18.

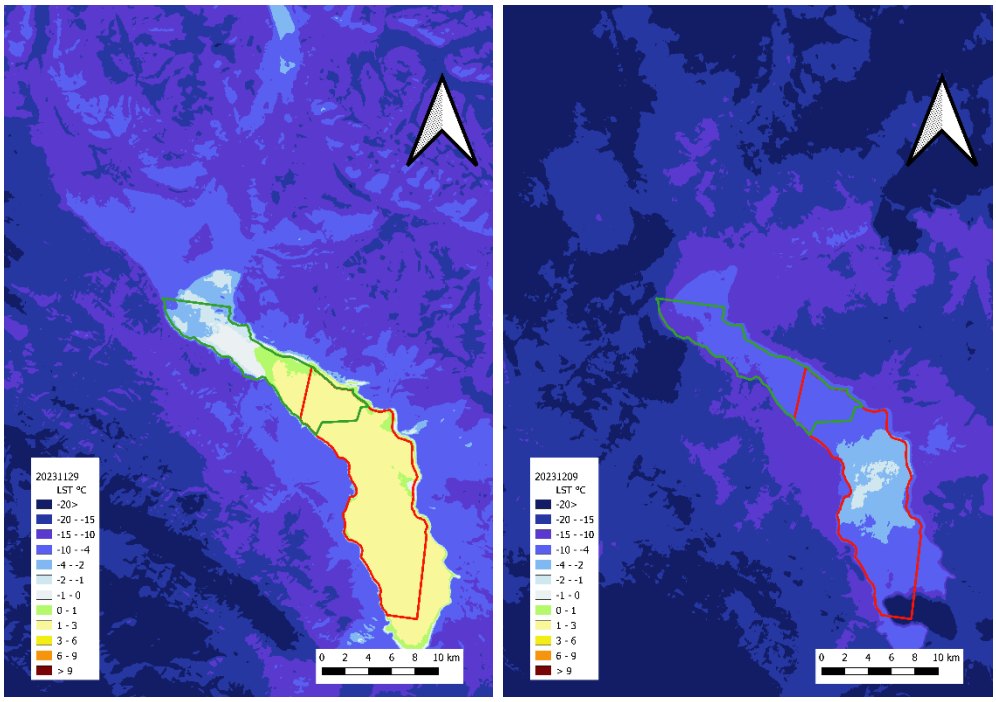


Figure 14. Seasonal Transition in Lake Surface Temperatures. This composite of Landsat-9 thermal band imagery showcases the shift in surface temperatures of Kluane Lake over two dates, November 29 and December 9, 2023. Study Site 1 and Study Site 2 are outlined in green and red, respectively.

4.5.2 Melt-onset Mapping Results

4.5.2.1 Kluane Lake

Figure 15 presents a detailed progression of ice melt dates across Kluane Lake during the spring of 2023, derived from RCM data. The melt-onset distribution map for Kluane Lake indicates a sequential melt pattern that predominantly moves from the northern to the southern parts of the lake. The northern parts of the study area, especially close to the lake's western shore, melt earlier between May 7 and May 15 (41% of the study area). Table 4 shows that a substantial portion of the selected area melts between May 7 and May 19 (78% in total). From April 24 to May 1 7% of pixels exhibit melt onset, which are clustered around shoreline regions and dispersed within other classes, caused by data noise.

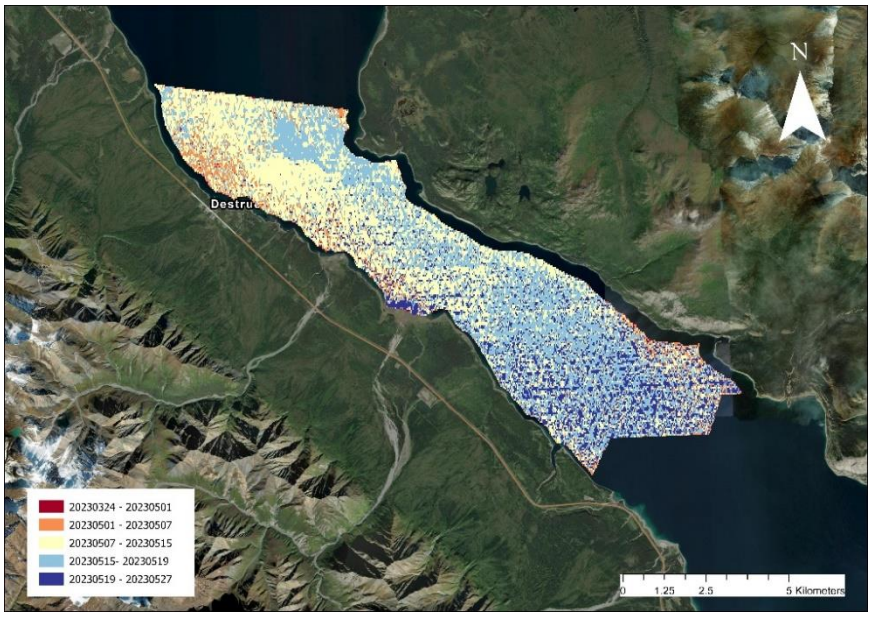


Figure 15. Spatial distribution of melt-onset dates at Study Site 1 in Kluane Lake, determined pixel by pixel using the first difference method for spring 2023

Figure 16 shows a map and two time series illustrating the backscatter intensity changes at Points C and D on Kluane Lake. As shown in Figure 15, melt-onset at Point C occurred between May 7 and May 15, while at Point D, it occurred between May 15 and May 19. These time intervals are supported by two time series in Figure 13 which shows the largest drop in backscatter intensity for Point C on May 7, and for Point D, on May 15.

Table 4. Percentage of melted pixels over spring 2023 for Kluane Lake selected area based on the first difference method

Melt-onset interval	% Melted Pixels
24 Apr 2023 – 7 May 2023	7
7 May 2023 – 15 May 2023	41.07
15 May 2023 – 19 May 2023	36.5
19 May 2023 – 27 May 2023	15.42

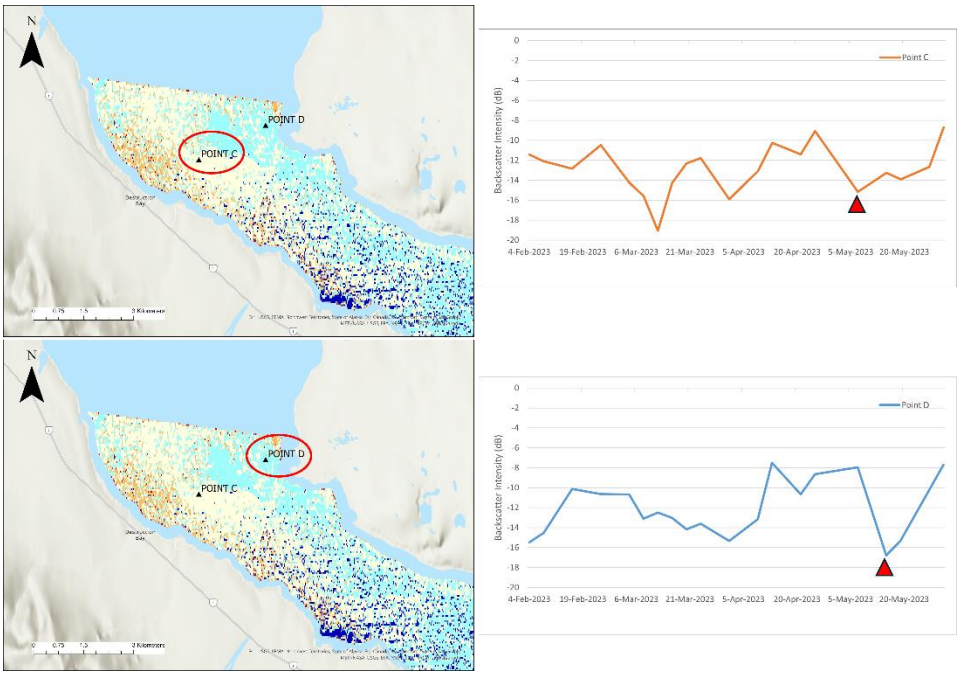


Figure 16. Backscatter variations at Points C and D on Kluane Lake. The map displays the spatial distribution of backscatter intensity at Points A and B on Kluane Lake. The time series graphs illustrate backscatter intensity changes from February to May 2023.

Two sources of validation were used to evaluate the melt-onset dates for Kluane Lake. Firstly, two Landsat images during critical events were analyzed (Figure 17). On April 29, temperatures began to rise, with substantial portions of the selected area between 0 °C and 2 °C, suggesting the start of the melting process. By May 13, temperatures across the lake uniformly increased, indicating most of the lake ice had started melting, supporting RCM data. The RCM images indicate that 85% of the pixels had started melting by May 19, while LST maps show that the entire lake surface uniformly reached the melting point (1~3 °C) by May 13, initiating the ongoing melting process until the lake was ice-free.

Secondly, Planet images from key dates within the melt period were selected for visual inspection (Figure 18). These dates are April 16, May 3, May 11, May 16, May 24, and May 30. The Planet image from April 16 shows Kluane Lake predominantly covered in ice. The ice appears uniform and intact, indicating that the melt process had not significantly commenced by this date. By May 3, slight changes in the ice cover are visible. Small areas, particularly around the western edges of the lake, show initial

signs of melting. Similarly, RCM melt-onset maps show melting from May 1 to May 7 in the northwestern edges of the area.

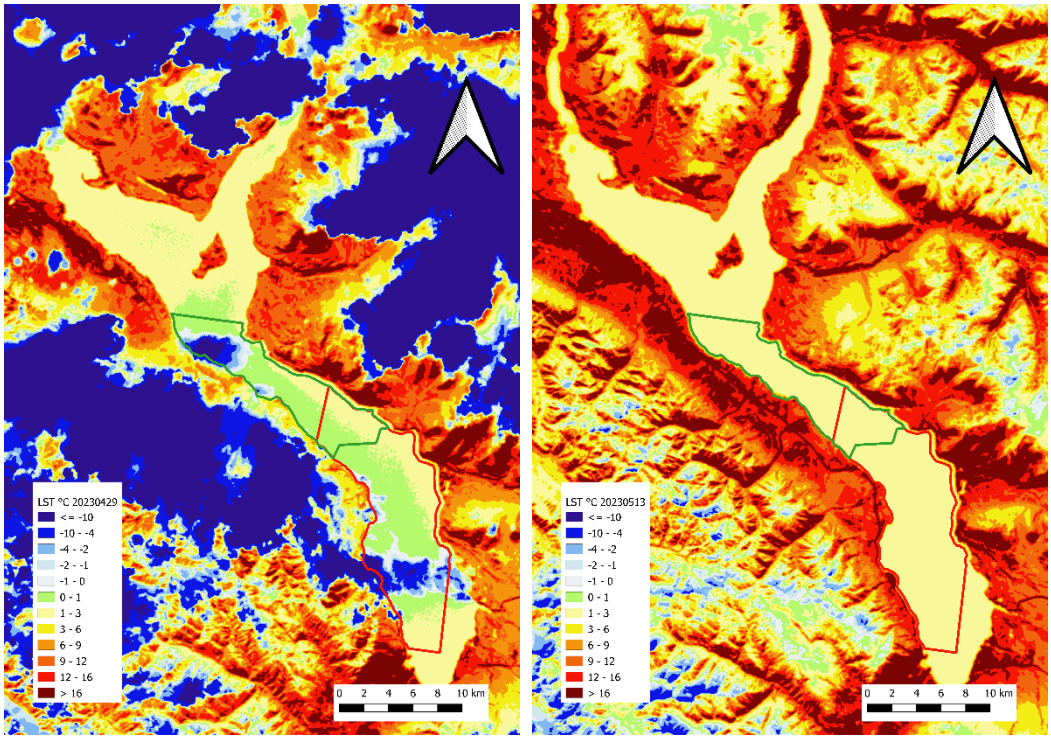
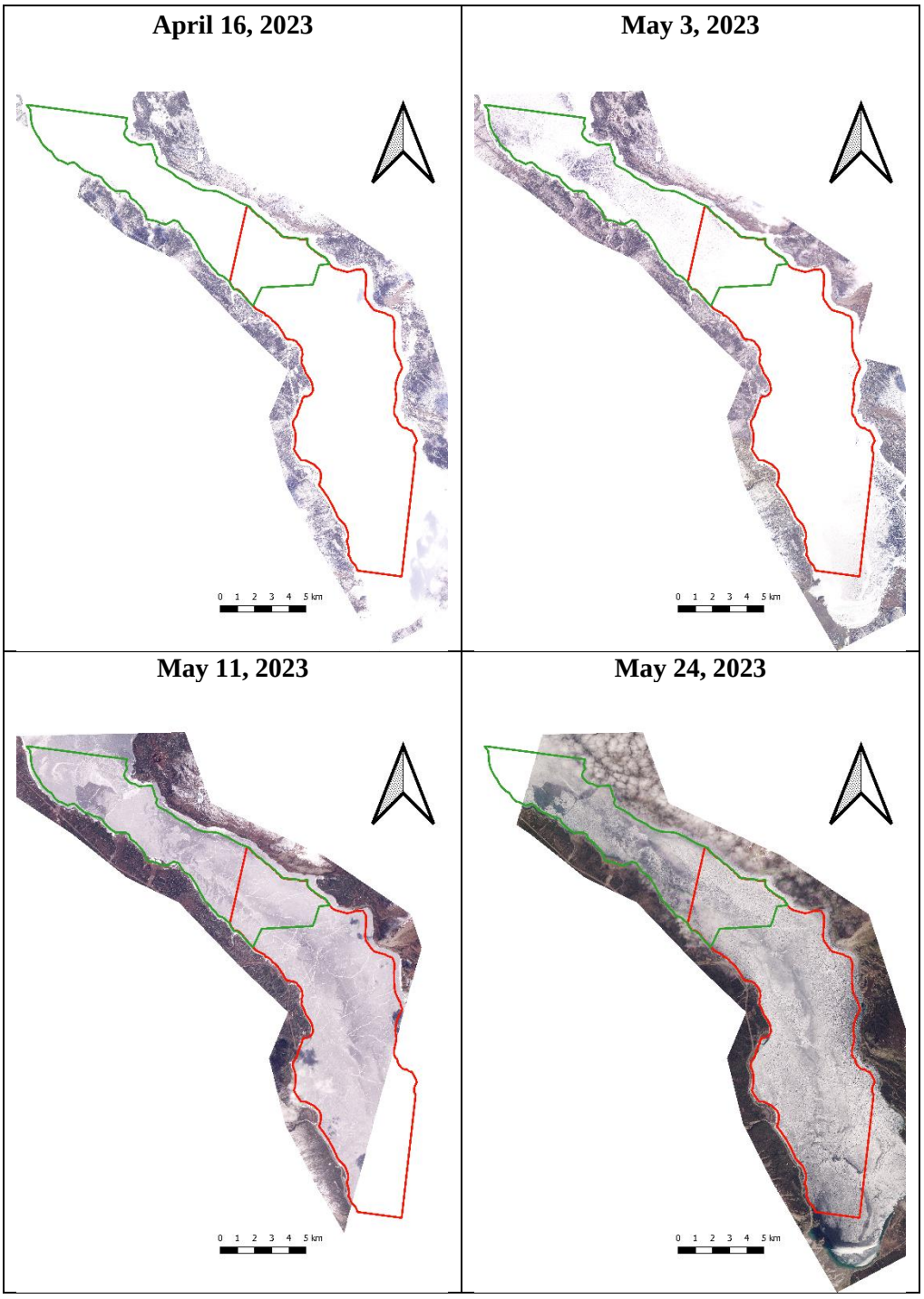


Figure 17. Seasonal Transition in Lake Surface Temperatures. This series of Landsat-9 thermal images documents the progressive warming of Kluane Lake's surface during the spring melt on April 29, and May 13, 2023. Each image vividly captures the increase in temperatures across the lake, highlighting areas of significant warming that contribute to the changing ice cover dynamics during the transition from winter to spring. Study Site 1 and Study Site 2 are outlined in green and red, respectively.


April 16, 2023
May 3, 2023
May 11, 2023
May 24, 2023
0 1 2 3 4 5 km

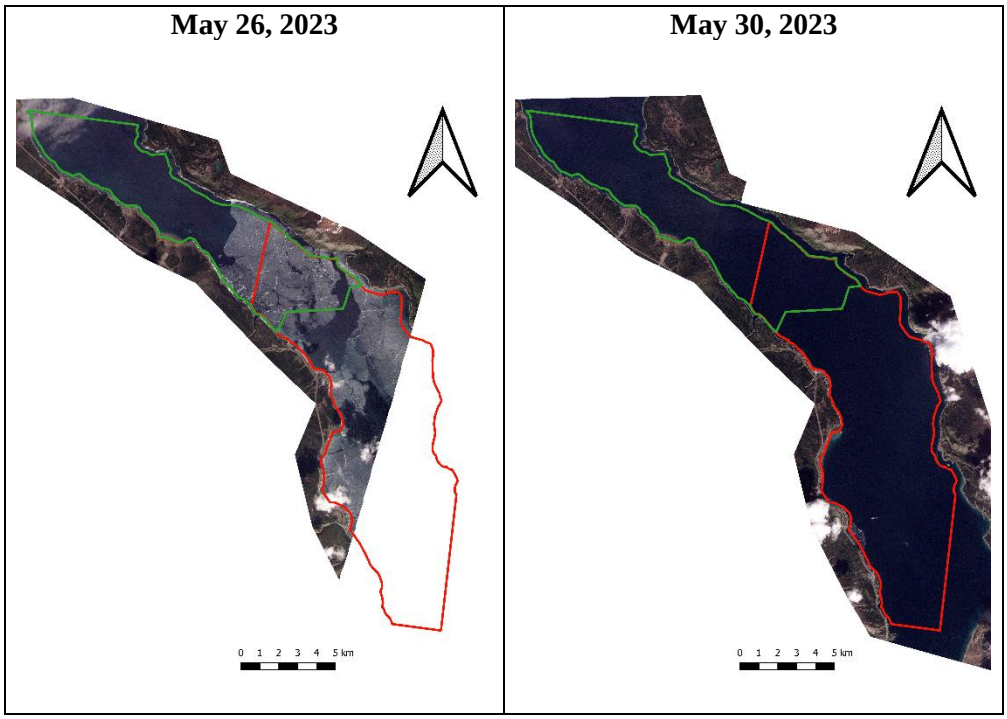


Figure 18. Sequential Planet Images Capturing the Melt Period of Kluane Lake (16 April - 30 May), This series of Planet images illustrates the progression of ice melt on Kluane Lake during the spring of 2023. Starting on 16 April, the lake is predominantly covered in ice. By 3 May, initial melting is observed around the edges. The 11 May image shows more pronounced melting. On 24 May, ice reduction and cracks are evident. By 26 May, the lake is nearly ice-free, with only small ice fragments visible. Finally, on 30 May, Kluane Lake is completely free of ice, marking the end of the melt period. Study Site 1 and Study Site 2 are outlined in green and red, respectively.

Monitoring the melt-onset during the spring of 2024 faced limitations due to the temporal resolution of RCM data. The available dataset consisted of two images from May and a few from April. Using these, the first difference algorithm identified a significant drop in backscatter intensity on April 13 (Figure 19), which was interpreted as the major melt-onset date for the lake's surface. This conclusion was based on a single, pronounced drop in backscatter values, suggesting a key transition in the surface properties.

Figure 20 illustrates the lake surface temperature for two critical dates during the spring melt of 2023: April 12 and April 21. On April 12, most areas on the lake surface exhibited temperatures between -

2°C and 0°C, signifying conditions conducive to the initial stages of melting. This temperature range aligns closely with the observation of a significant drop in backscatter intensity on April 13, supporting the interpretation that this date marks the onset of substantial melting. By April 21, the lake surface shows notable progression in the melting process, with significant portions of the lake already above 0°C, signaling ongoing melt in these regions. However, some parts of the lake's surface are still observed at around 0°C, indicating areas where melting is still in progress.

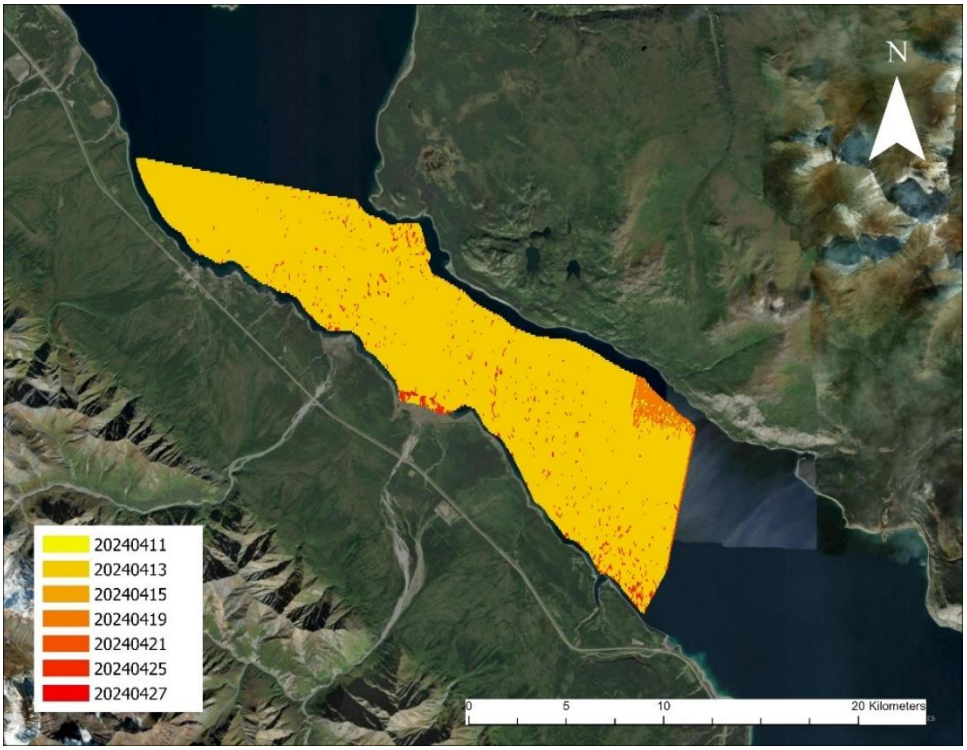


Figure 19. Spatial distribution of melt-onset dates at Study Site 1 in Kluane Lake, determined pixel by pixel using the first difference method for spring 2024.

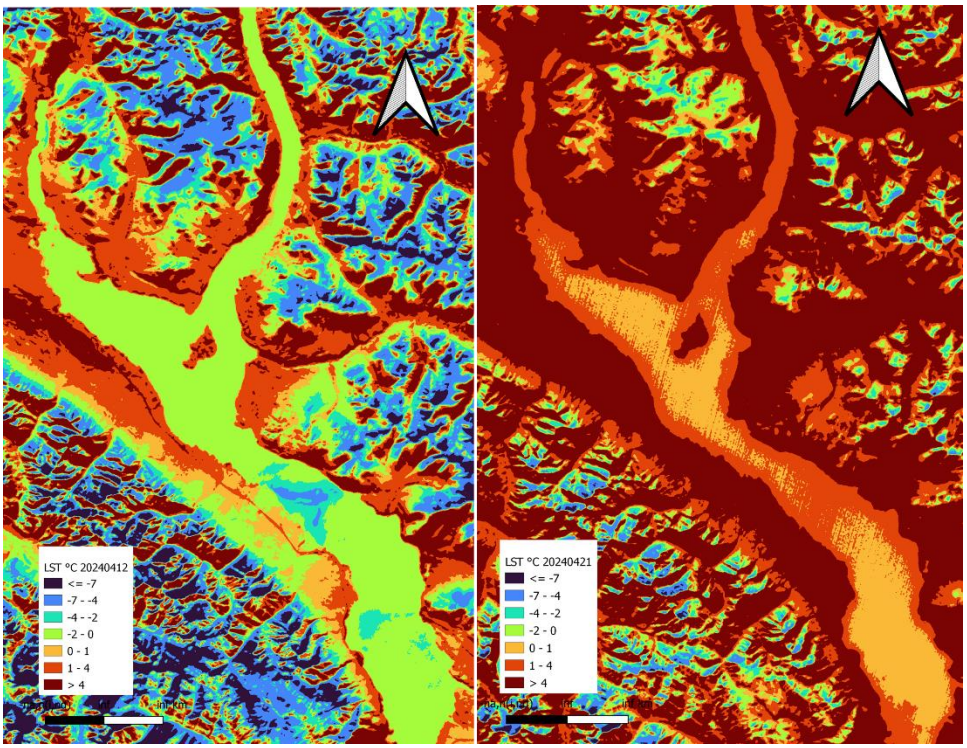


Figure 20. Seasonal Transition in Lake Surface Temperatures during the spring melt on April 12, and April 21, 2023.

4.5.2.2 Ryan and Landing Lakes

Figure 21 depicts the melt-onset dates for Ryan and Landing lakes in the Spring of 2023, derived from the first difference method using RCM data. These lakes differ significantly in depth, with Ryan Lake having a depth of 90 meters and Landing Lake at 4.3 meters. This fundamental difference in depth plays an important role in the patterns of ice melt observed in each lake. Table 5 shows that the shallower Landing Lake melts faster, with most melt events occurring between May 1 and 14 (81.9% of pixels), while Ryan Lake's melt is more gradual and extends into late May. Table 5 shows that melt-onset dates for Ryan Lake span from April 22 to May 31, highlighting the extended melt period due to greater depth.

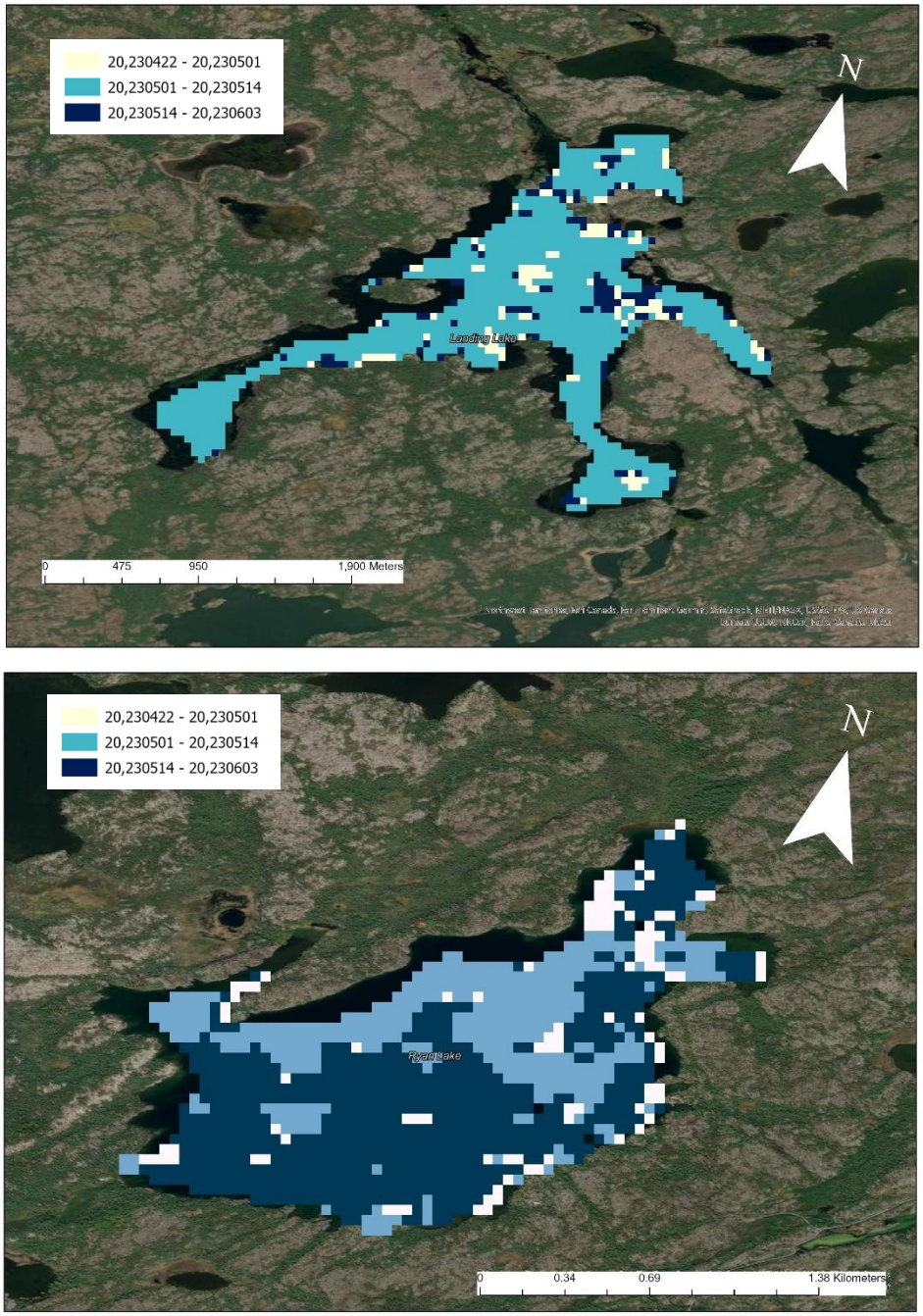


Figure 21. Spatial distribution of melt-onset dates for Landing Lake and Ryan Lake, determined pixel by pixel using the first difference method during spring 2023. The north arrow represents the true north.

Table 5. Percentage of melted pixels over spring 2023 for Landing Lake and Ryan Lake based on the first difference method

Melt-onset interval Landing Lake	%Melted Pixels Landing Lake	Melt-onset interval Ryan Lake	% Melted Pixels Ryan Lake
April 22 – May 1	8.8	April 22 – May 1	8.9
May 1 – May 14	81.9	May 1 – May 14	31.2
May 14 – June 1	9.3	May 14 – June 1	59.2

Monitoring the melt process of Ryan and Landing Lakes comes with challenges, mainly due to the limited number of images and inconsistent gaps between them. This made us rely more on Planet images to identify significant drops in backscatter, unlike the more consistent monitoring of Kluane Lake. For example, a major drop in backscatter for Ryan Lake was observed on April 21, followed by a long gap until the next available image. Because of this, thermal maps and Planet images were crucial in determining the melting period. These additional data sources are necessary to understand changes in backscatter accurately.

Figure 22 includes surface temperatures captured on April 25, May 4, and May 12, 2023, demonstrating the gradual warming of the lakes' surfaces. On April 25, RCM results indicate that the lake is still frozen. Similarly, LST maps in Figure 22 show that on April 25 temperatures were predominantly below freezing (-5 to -20 °C), confirming that the lake is still in a frozen state. On May 4, LST Map Displays temperatures rising above 0 °C, indicating the likelihood of melt-onset. This temperature increase validates the RCM-derived melt-onset dates for Landing Lake from May 1 to May 14. On May 12, the LST map shows widespread temperatures above 7 °C, supporting the RCM data that most of the lake ice has melted by this date. This map also highlights the impact of depth on the delayed melting of lakes, as the average temperature of Ryan Lake is lower than that of Landing Lake. This observation confirms the later melt dates for Ryan Lake compared to Landing Lake.

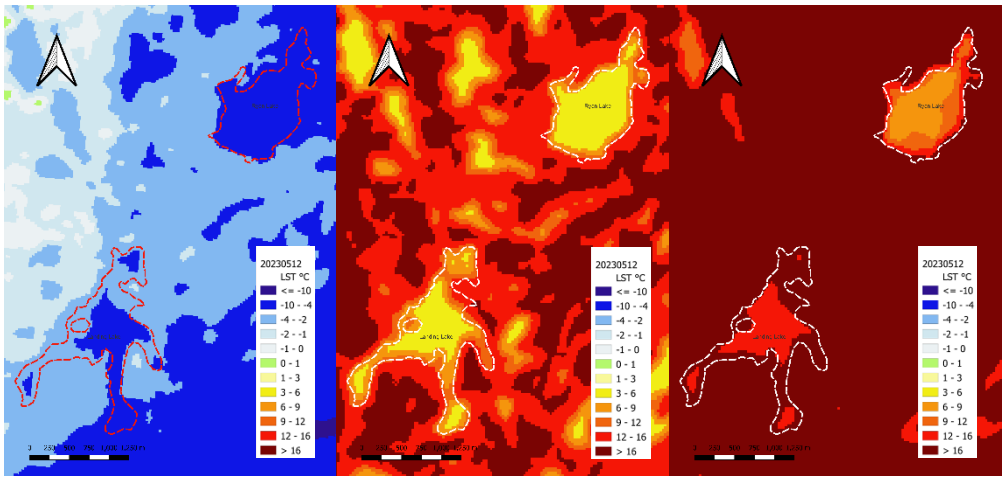


Figure 22. Temporal Variation in Land Surface Temperatures. This series of Landsat-9 thermal band images captures the changing surface temperatures of Ryan and Lading lakes on three different dates—April 25, May 4, and May 12, 2023. The maps depict the gradual warming of the lake's surface as spring progresses, highlighting significant thermal shifts that impact the spring thaw.

Figure 23 illustrates the transition from fully ice-covered lakes on April 24 to a completely ice-free state by May 16. On April 24, Planet image shows the lakes entirely covered in ice, validating the RCM results that the melt process has not started. Initial signs of melting appear on May 3 and May 4, especially across Landing Lake, supporting the melt-onset time interval in Table 5. By May 7 Planet image shows open water at Landing Lake and fragmented ice at Ryan Lake, validating the RCM data indicating later melt-onset dates for Ryan Lake. For both Landing and Ryan Lakes, the RCM results indicate later melt-onset dates. This delay is attributed to the lack of image acquisition during critical melt events, which prevents the precise identification of the initial melting periods.

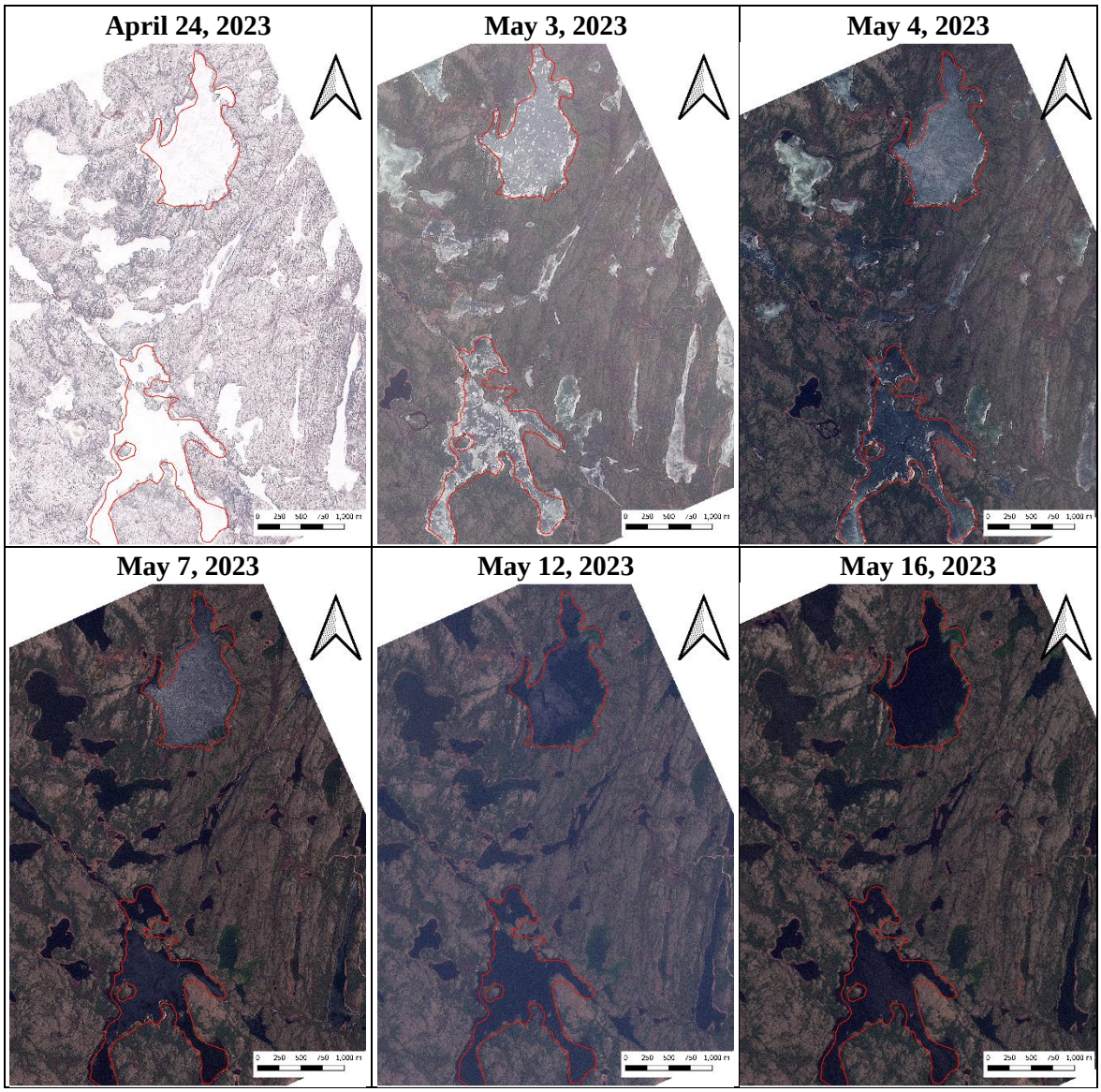


Figure 23. Spring melt progression captured by Planet images over Ryan Lake and Landing Lake from April 24 to May 16, 2023.

4.5.3 Observed Trends in Compact Polarimetric (CP) Parameters During Ice Formation and Melting

The selected Compact Polarimetric (CP) parameters for interpreting the lake ice cycle—Degree of Polarization (DoP), Circular Polarization Ratio (CPR), Relative Phase, and Alpha Angle—were calculated for Study Sites 1 and 2 in Kluane Lake. These parameters were analyzed in detail, and their

results are presented using boxplots, which effectively visualize the distribution of the data over time. Boxplots are particularly suited for this purpose as they highlight key statistical features, including the interquartile range (IQR), which represents the spread of the central 50% of the data.

The IQR serves as a robust measure of variability, focusing on the middle portion of the data while minimizing the influence of outliers and extremes. This allows for a clearer interpretation of narrowing trends in the CP parameters, which are linked to key ice phenology events such as freeze-onset and melt-onset. Detailed discussions of these results are provided in the following sections, while plots of other CP parameters can be found in Appendix A.

4.5.3.1 Results of Degree of Polarization (DoP)

The Degree of Polarization (DoP) quantifies the proportion of the total scattered signal that is polarized, offering valuable information on the homogeneity of the lake ice surface and changes in surface conditions over the ice cycle. Figure 24 and Figure 25 present the seasonal cycle of DoP values at two study sites in Kluane Lake, illustrating how these values fluctuate in response to changing surface conditions and temperature. At the beginning of the monitoring period (October-November 2023), DoP values remain relatively low, hovering around 0.5 or less.

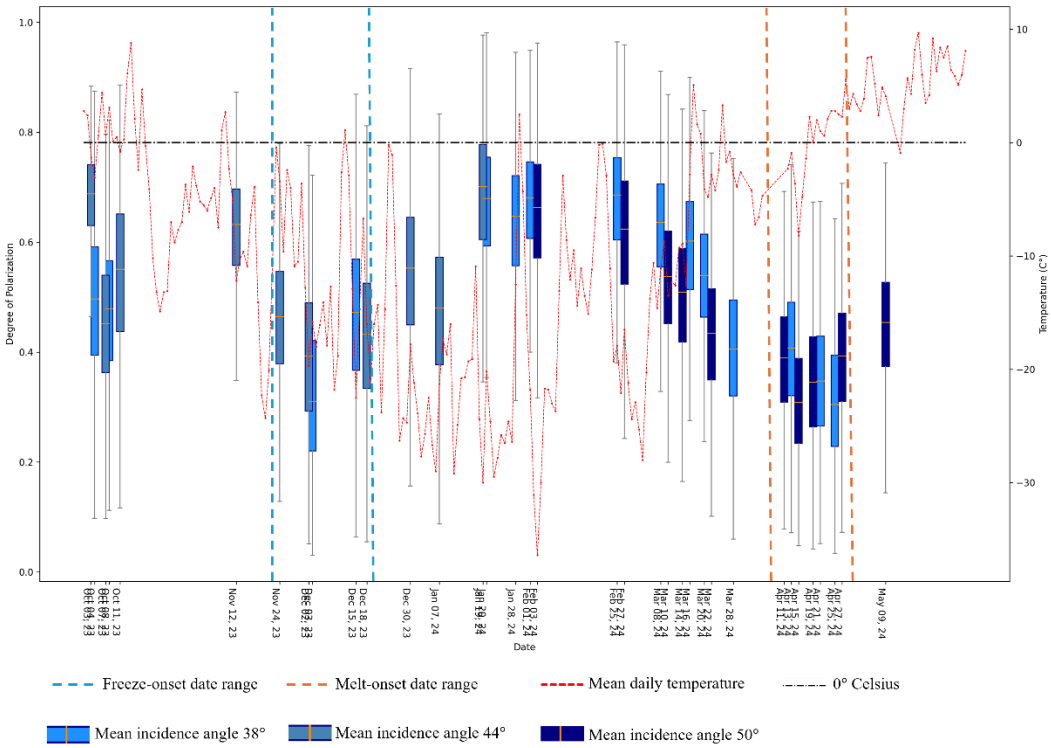


Figure 24. Whisker plot of DoP values at Kluane Lake, Site 1 (October 2023–May 2024), shown across three incidence angles (38°, 44°, 50°) with mean daily temperatures (red dashed line), a 0°C reference line (black dash-dot), and freeze/melt-onset periods marked by vertical dashed lines.

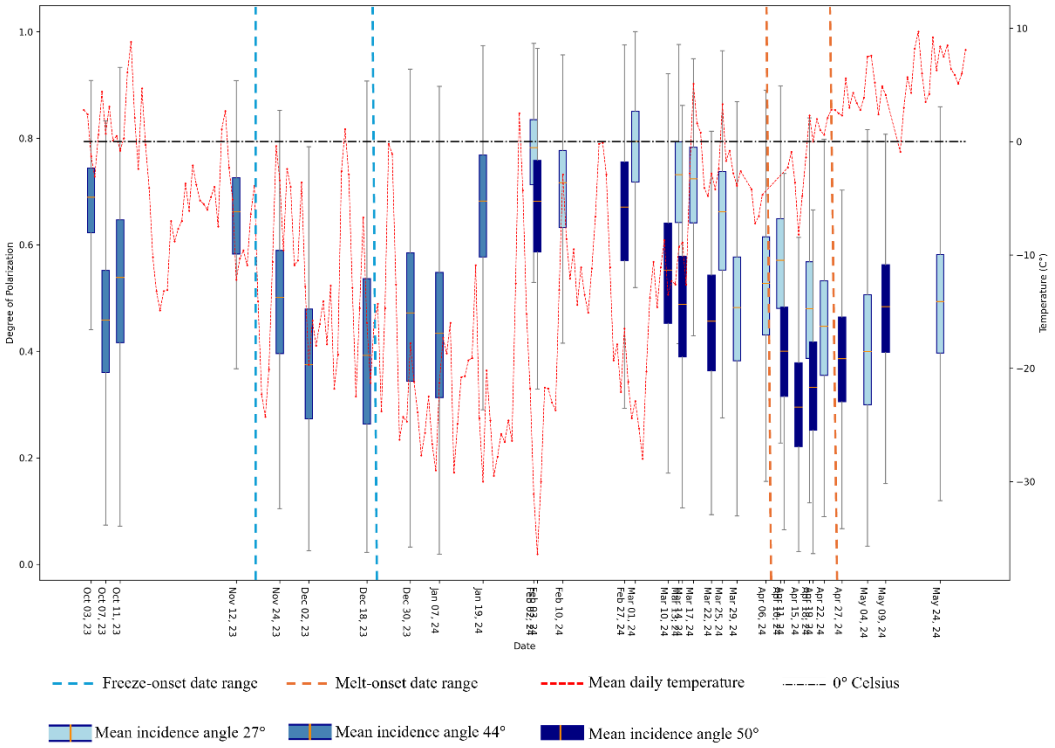


Figure 25. Whisker plot of DoP values at Kluane Lake, Site 2 (October 2023–May 2024), shown across three incidence angles (27°, 44°, 50°) with mean daily temperatures (red dashed line), a 0°C reference line (black dash-dot), and freeze/melt-onset periods marked by vertical dashed lines.

As temperatures drop and ice begins to form, DoP values start to increase. However, the radar signal continues to interact with heterogeneous conditions—a mixture of water and newly forming ice—leading to variability in polarization states and fluctuations in DoP values. During the mid-winter months, the DoP values show a general increase for both incidence angle ranges, with the median values reaching around 0.6 to 0.8 for the lower incidence angles (25°) and about 0.5 to 0.7 for the higher incidence angles (44°–50°).

In the melt-onset period starting around March 2024 and extending to May 2024, temperatures frequently rise above 0°C, signaling the transition to melting conditions. During this phase, DoP values begin to decline, particularly by May 2024, where values range from 0.4 to 0.6 at lower incidence angles and even lower at higher angles.

4.5.3.2 Results of Circular Polarization Ratio (CPR)

The Circular Polarization Ratio (CPR) compares the backscatter power in right-hand and left-hand circular polarizations, helping to assess surface roughness and distinguish between smooth and rough ice surfaces during different ice formation stages. This study used CPR to monitor the ice formation and melting phases in Kluane Lake. Figure 26 and Figure 28 display whisker plots of CPR values for each study site, while Figure 30 presents Planet satellite images capturing key dates throughout the ice cycle.

During the pre-freeze stage (October to November 2023), CPR values in the whisker plots are tightly clustered, with small boxes indicating consistent, ice-free conditions across the lake's surface. As temperatures begin to drop below 0°C, the CPR values start to show increased spread, reflecting a more variable surface made up of both ice and water.

In mid-winter (January to March), CPR values become lower and more consistent, with smaller whisker boxes indicating a stable, frozen surface. The decrease in CPR values corresponds to a thicker, more uniform ice or snow-covered ice surface. The narrowing IQR values during this period (Figure 27 and Figure 29) further confirm the stabilization in CPR values, reflecting reduced variability in scattering properties. The Planet imagery (Figure 30, Top-Right and Bottom-Left) also captures the homogeneity of the ice/snow cover during mid-winter, illustrating a consolidated ice surface on the lake.

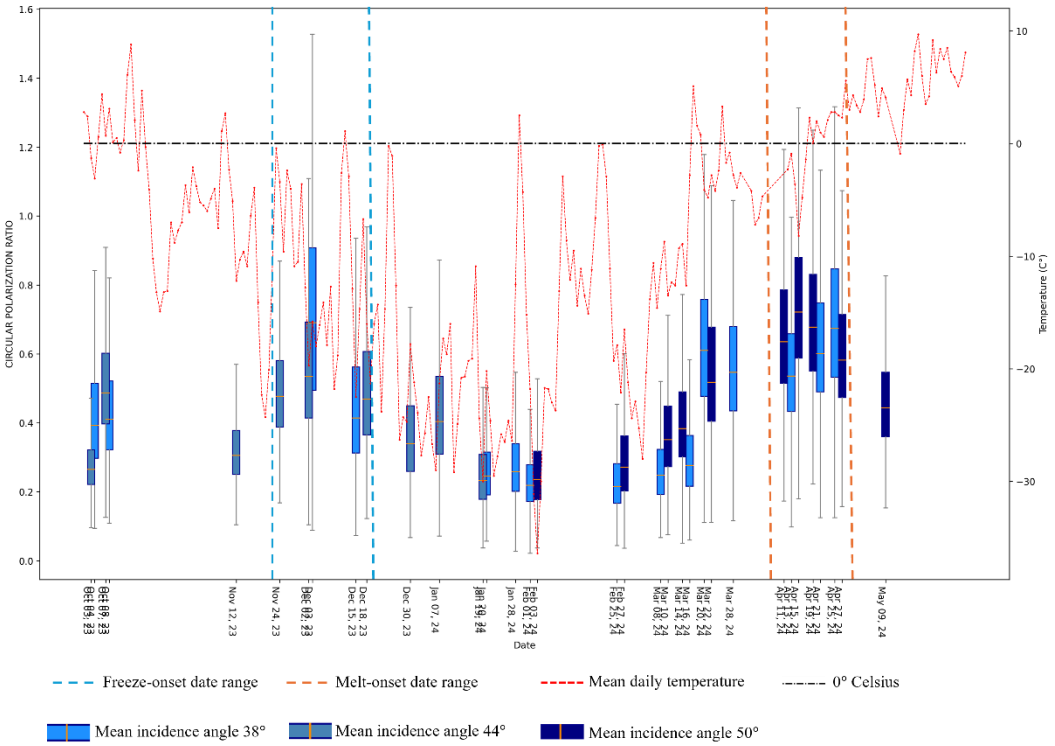


Figure 26. CPR values at Kluane Lake, Site 1 (October 2023–May 2024), shown for incidence angles of 38°, 44°, and 50°, with mean daily temperature (red dashed line) and freeze/melt-onset periods marked by vertical dashed lines.

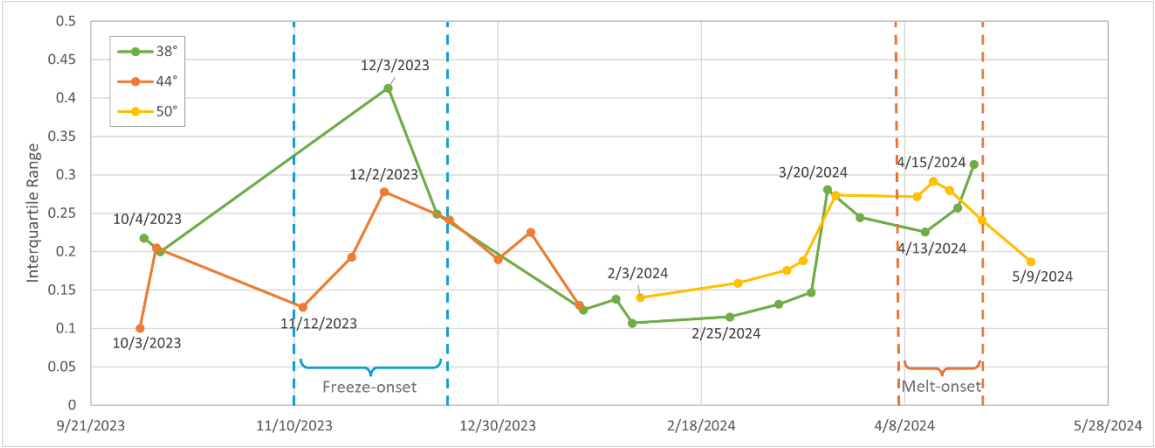


Figure 27. Temporal variation of the interquartile range (IQR) for the CPR at Kluane Lake, Site 1 (October 2023–May 2024), calculated across three incidence angles (38°, 44°, and 50°).

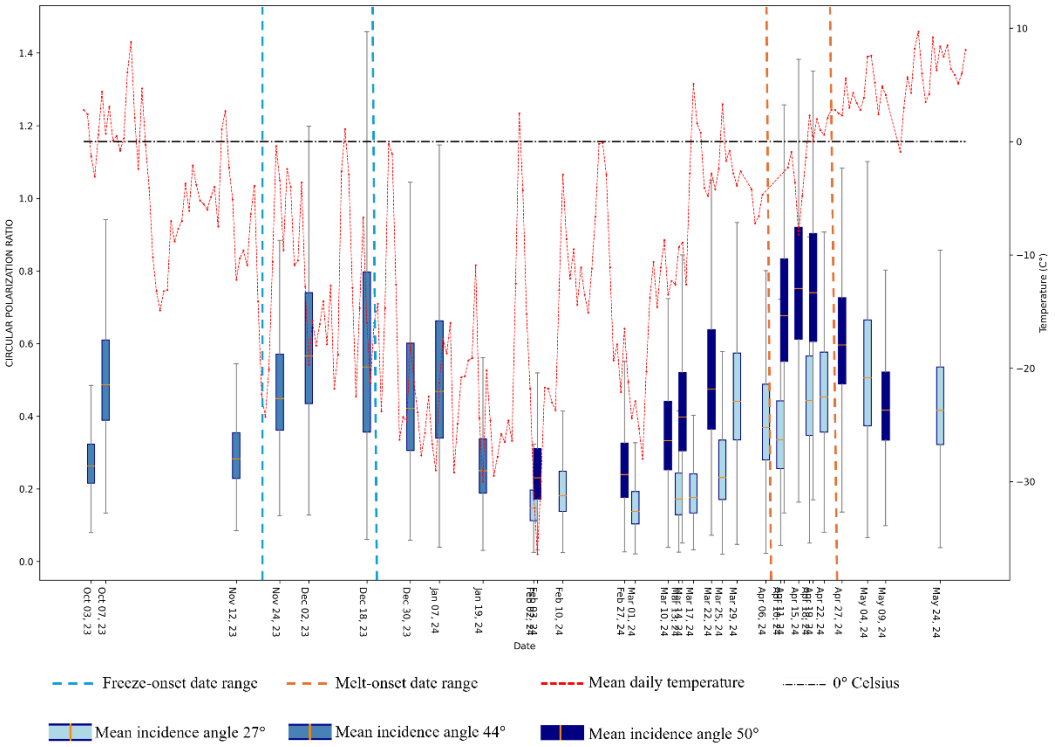


Figure 28. CPR values at Kluane Lake, Site 2 (October 2023–May 2024), shown for incidence angles of 27°, 44°, and 50°, with mean daily temperature (red dashed line) and freeze/melt-onset periods marked by vertical dashed lines.

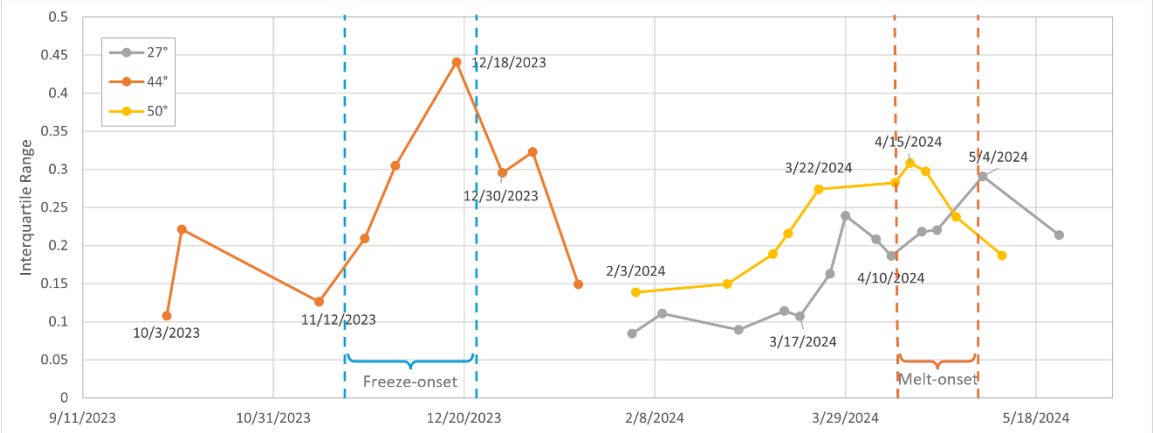


Figure 29. Temporal variation of the interquartile range (IQR) for the CPR at Kluane Lake, Site 2 (October 2023–May 2024), calculated across three incidence angles (27°, 44°, and 50°).

As temperatures rise above 0°C, marking the melt-onset period, CPR values increase and become more variable, with larger whisker boxes indicating a diverse mix of surface conditions. This increase is attributed to melting ice and the formation of meltwater on the ice surface, which introduces rougher textures and scattered reflections. Figure 30 (Bottom-Right) shows the lake beginning to break up, with visible cracks and open water patches that explain the elevated CPR values.

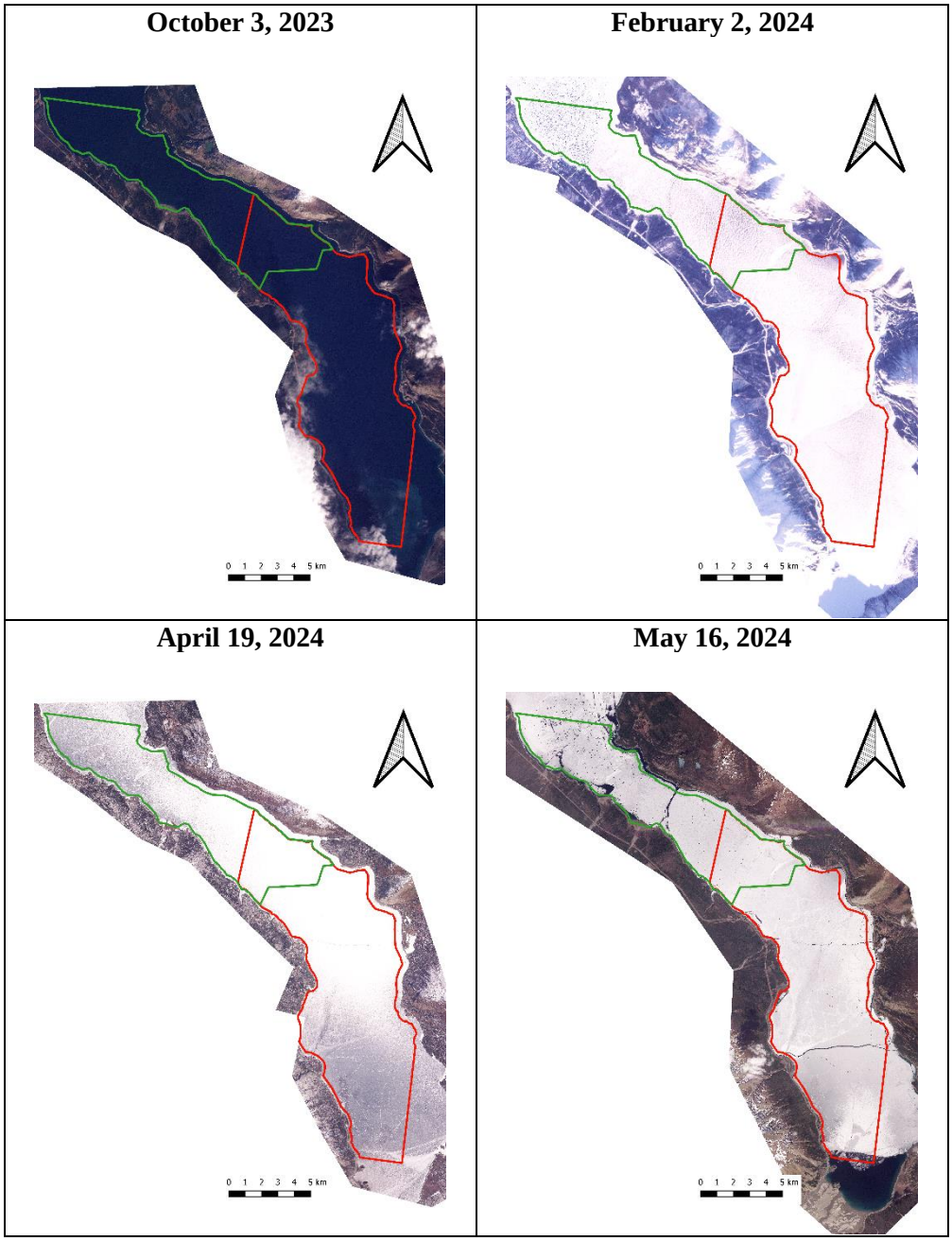


Figure 30. Planet satellite imagery of Study Site 2, Kluane Lake captured on key dates during the ice formation and melting periods. October 3, 2023, showing an ice-free lake surface prior to freeze-up; February 2, 2024, displaying the lake in mid-winter with full ice cover; April 19, 2024, illustrating the lake during late winter; and May 16, 2024, showing the onset of ice melt with visible cracks and open water patches. Study Site 1 and Study Site 2 are outlined in green and red, respectively.

Figure 31 and Figure 32 visually illustrate the temporal and spatial variability of CPR values across Kluane Lake with lighter colors indicating lower CPR values and darker colors representing higher values. In the pre-freeze stage (October 2023), the lake shows uniformly low CPR values, confirming ice-free conditions. As the freeze-up begins (December 2023), variability increases, with patches of higher CPR indicating areas of ice formation and rougher surfaces. By mid-winter (February 2024), CPR values are relatively low across the lake, reflecting the ice or snow-covered ice surface. Finally, during the melting phase (May 2024), the image shows a mix of high and low CPR values, representing the heterogeneous surface conditions as the ice breaks apart and meltwater forms, exposing smoother areas. Additionally, areas of elevated CPR observed in certain regions may correspond to the formation of ice ridges, where wind-driven compression of ice sheets creates rough, jagged features. Notably, the ice ridge is particularly visible in Figure 30, the 2024-02-02 image, where the elevated CPR values, concentrated in the western part of Study Site 2, highlight its rough surface and complex scattering properties.

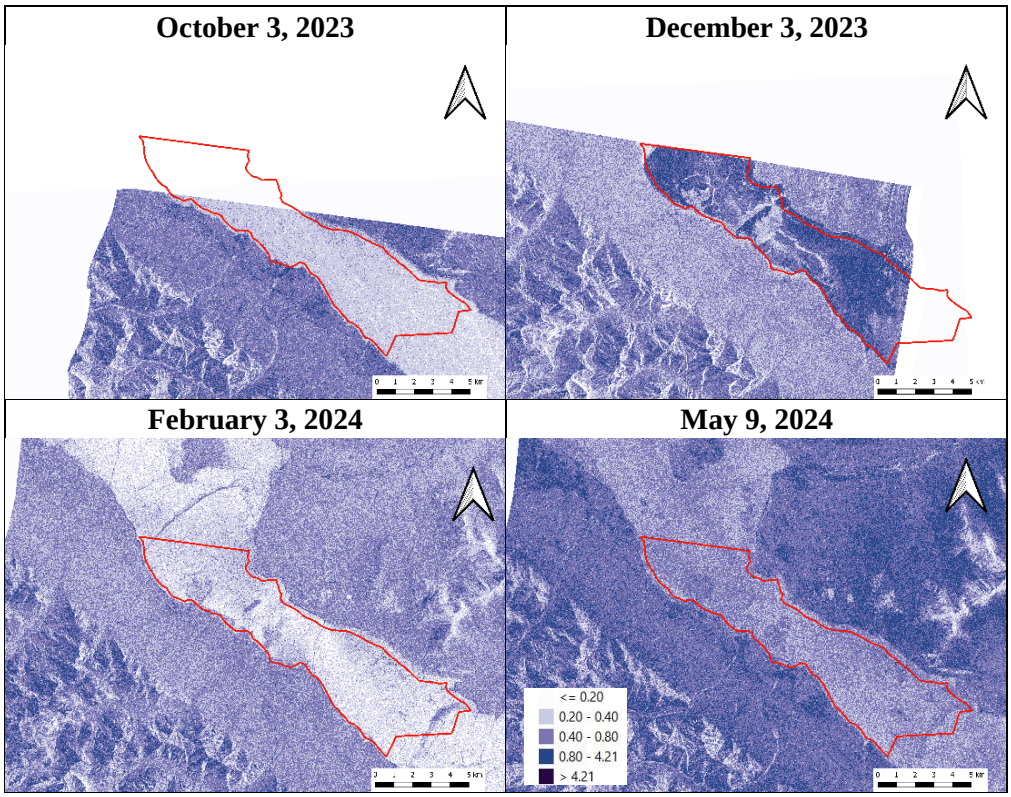


Figure 31. CPR values at Study Site 1, Kluane Lake, for key dates during the ice cycle. Images display CPR values on October 3, 2023, showing ice-free conditions; December 2, 2023, with increased CPR variability during the initial freeze-up phase; February 3, 2024, depicting stable low CPR values during full ice cover; and May 9, 2024, illustrating heterogeneous CPR patterns as ice melt begins, with both high and low values indicating mixed ice-water surfaces.

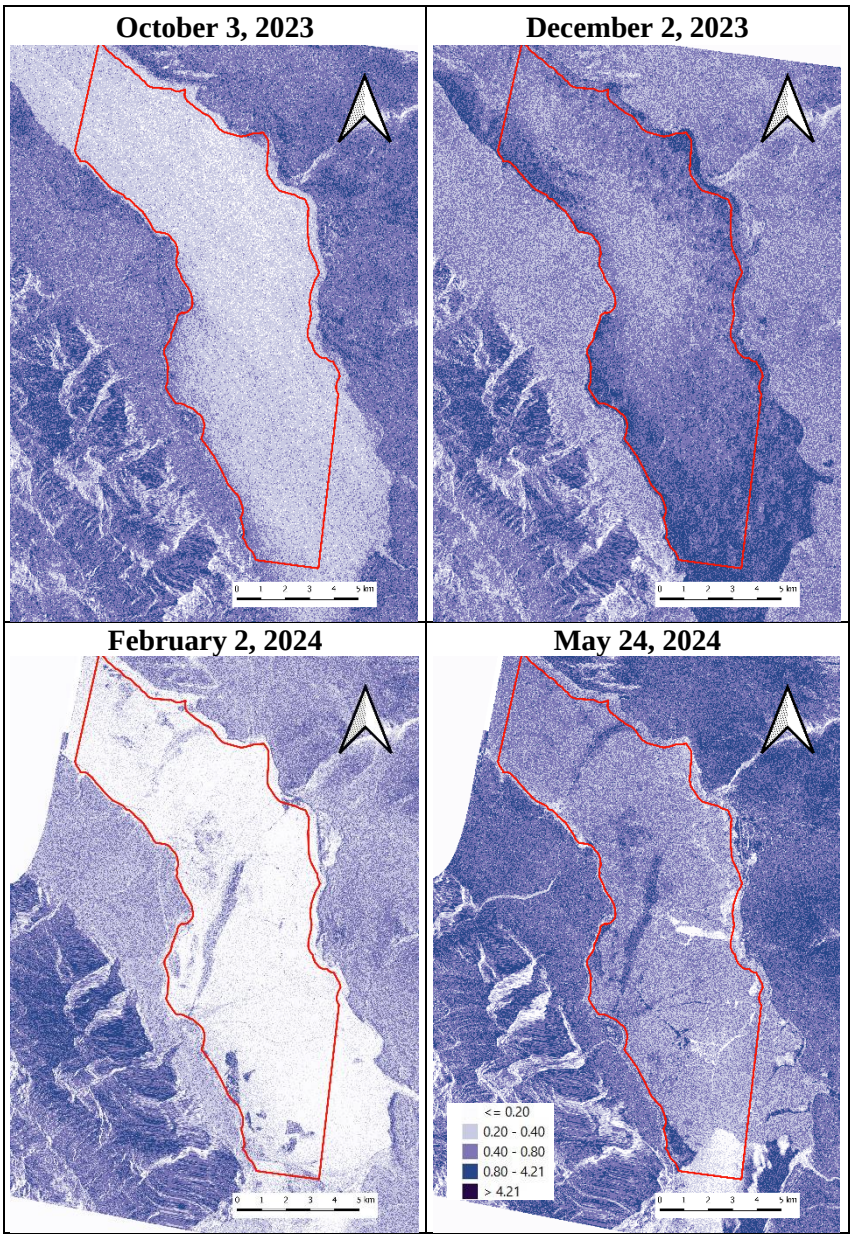


Figure 32. CPR values at Study Site 2, Kluane Lake, for key dates during the ice cycle. October 3, 2023, representing ice-free conditions; December 2, 2023, showing increased CPR variability during the freeze-onset phase; February 2, 2024, depicting relatively low CPR values as the lake is fully frozen, and May 24, 2024, illustrating a mixed pattern of high and low CPR values as ice melt begins, creating heterogeneous surface conditions.

4.5.3.3 Results of Relative Phase ($\boldsymbol{\delta}$)

The Relative Phase (δ) measures the phase difference between right-hand circular polarization (RH) and left-hand circular polarization (RV). It provides insights into the dominant scattering mechanism, particularly useful for identifying transitions between surface and volume scattering in ice phenology. In Figure 33 and Figure 35, the whisker plots of δ values from October 2023 to May 2024 illustrate how these scattering mechanisms shift with seasonal transitions. Throughout the freeze-melt cycle, δ values demonstrate relatively low variability, particularly during mid-winter, where the small boxplot sizes suggest stable, consistent ice cover with minimal internal heterogeneity. This stability is further supported by the narrowing of IQR values in Figure 34 and Figure 36, which indicate reduced variability in δ during mid-winter.

Early in the period (October to November), δ values show more variability, as indicated by larger boxplot spreads. As temperatures drop and ice begins to form in December, δ values become more consistent, with smaller boxplots indicating a homogeneous ice surface. The decreasing IQR values (Figure 34 and Figure 36) further reinforce this stabilization, emphasizing the consolidated ice cover.

In March, as the seasonal melt-onset begins, δ values exhibit increased variability, with larger boxplot sizes reflecting the breakup of ice and the formation of meltwater on the surface. Toward the end of the melting season, just before the ice fully disappears, δ values experience a notable increase in variability, likely due to complex scattering within the layered structure of melting ice and water.

Figure 37 and Figure 38 illustrate the relative phase distribution over Kluane Lake throughout the ice formation and melt period. On October 3, and December 2 when the lake was ice-free, most of the surface exhibited positive δ values, suggesting wind-driven roughness on the open water surface. On February 1 and 2, the uniform blue shading points to a stable, snow-covered ice surface with coherent scattering. By May, the increased presence of darker areas highlights the complex scattering from melting ice and water ponds, reflecting greater surface heterogeneity.

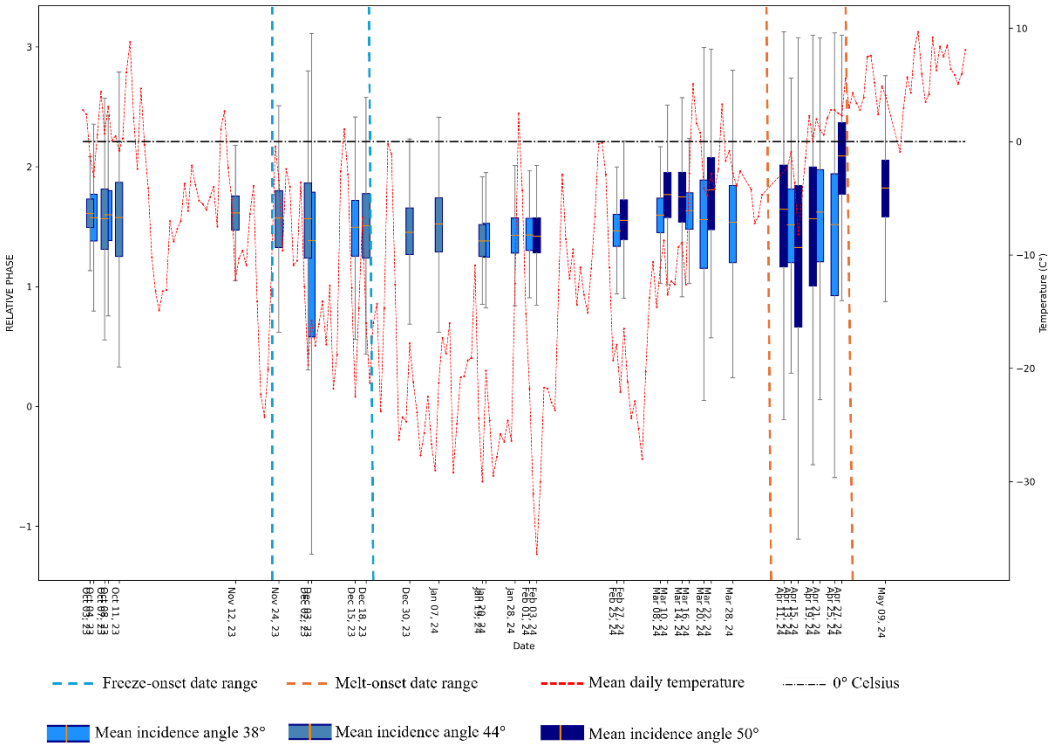


Figure 33. Whisker Plot of Relative Phase Difference (δ) at Study Site 1, Kluane Lake, from October 2023 to May 2024. This plot shows δ values at incidence angles of 38°, 44°, and 50°, overlaid with mean daily temperature (red dashed line) and a 0°C reference line. Freeze-onset and melt-onset periods, calculated using the First Difference method, are marked with vertical dashed lines.

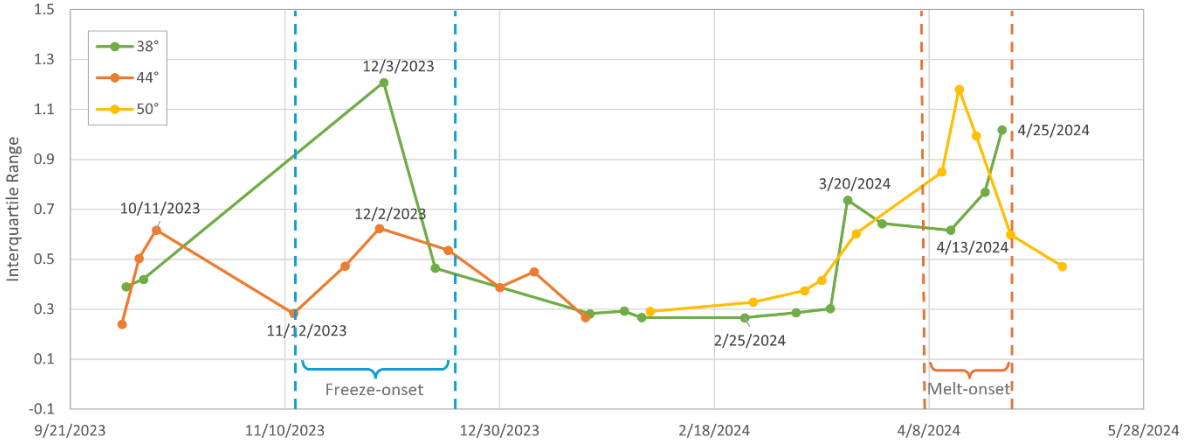


Figure 34.Temporal variation of the interquartile range (IQR) for the Relative Phase at Kluane Lake, Site 1 (October 2023–May 2024), calculated for incidence angles 38°, 44°, and 50°, with vertical dashed lines indicating freeze-onset and melt-onset periods.

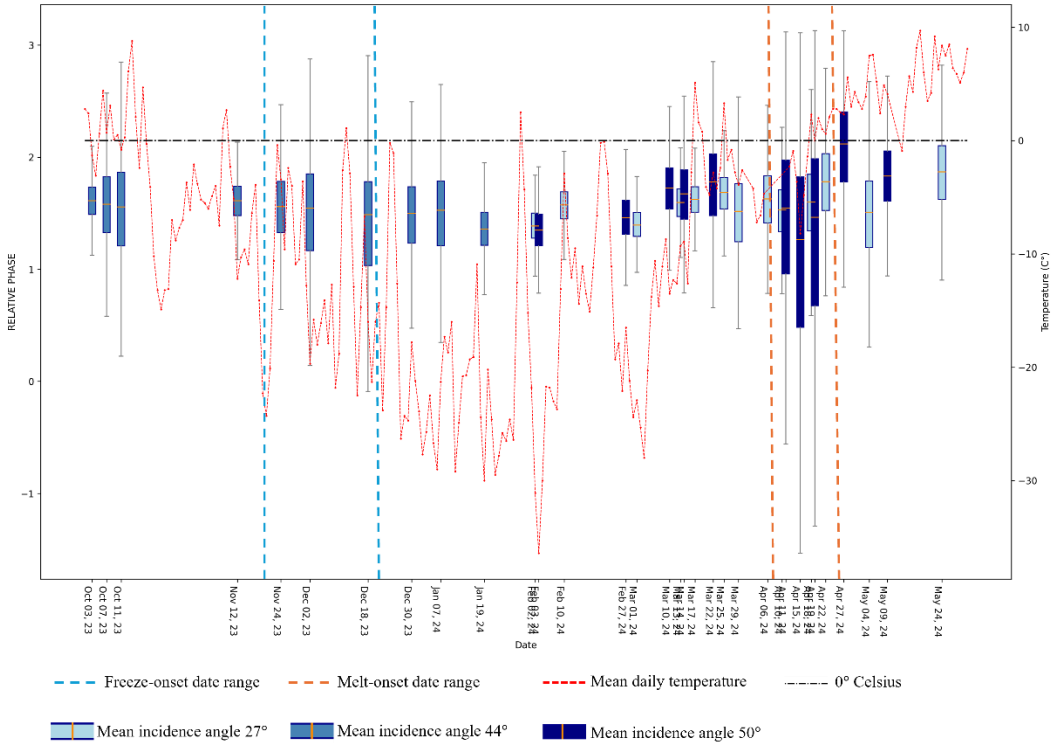


Figure 35. Whisker Plot of Relative Phase Difference (δ) at Study Site 2, Kluane Lake, from October 2023 to May 2024. This plot shows δ values at incidence angles of 27°, 44°, and 50° with mean daily temperature and a 0°C line. Freeze-onset and melt-onset periods, calculated using the First Difference method, are marked with vertical dashed lines.

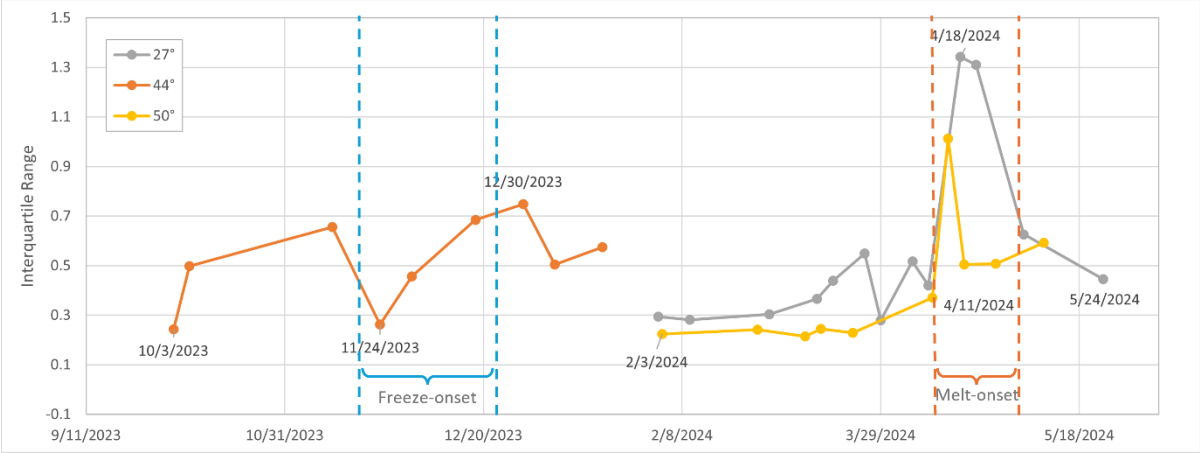


Figure 36. Temporal variation of the interquartile range (IQR) for the Relative Phase at Kluane Lake, Site 2 (October 2023–May 2024), calculated for incidence angles 27°, 44°, and 50°, with vertical dashed lines indicating freeze-onset and melt-onset date range.

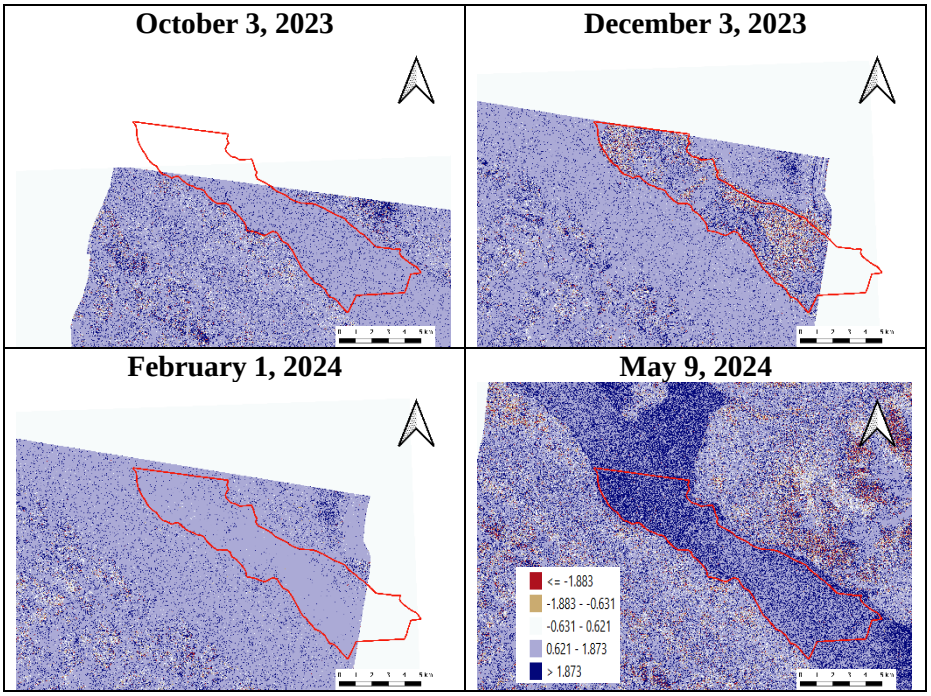


Figure 37. Spatial Distribution of Relative Phase (δ) at Study Site 1, Kluane Lake, from October 2023 to May 2024.

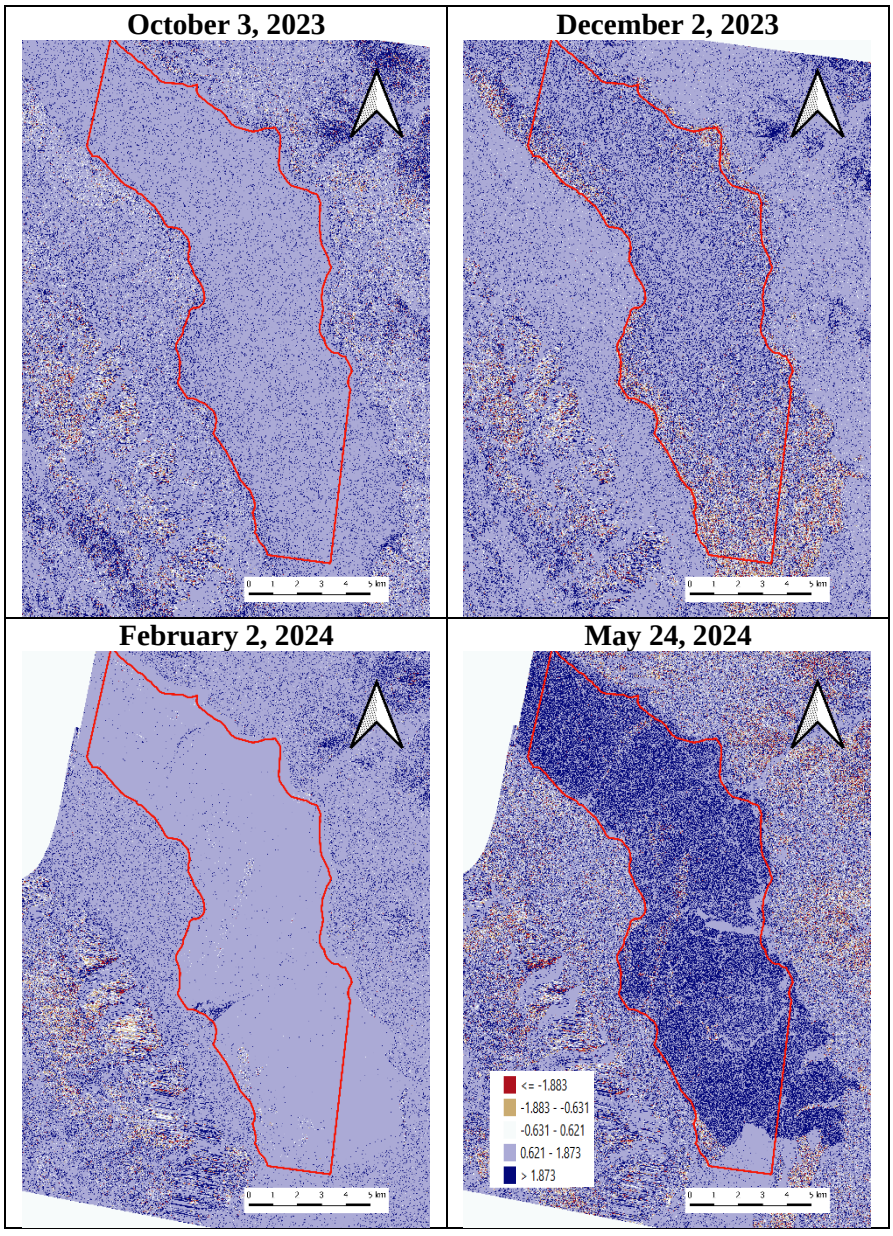


Figure 38. Spatial Distribution of Relative Phase (δ) at Study Site 2, Kluane Lake, from October 2023 to May 2024.

4.5.3.4 Results of Alpha Angle

The Alpha Angle represents the scattering type of the target and helps classify the dominant scattering mechanism (e.g., surface, volume, or double-bounce scattering) within a pixel. In the case of lake ice

phenology, the alpha parameter helps differentiate between different stages of ice formation, structure, and melting by indicating the predominant scattering mechanism.

Figure 39 and Figure 41 display whisker plots of alpha values from October 2023 to May 2024 for Study Sites 1 and 2. In both plots, alpha values show notable increases during freeze-onset and melt-onset periods, suggesting volume scattering due to mixed layers of ice and water. The increasing IQR values during these periods, as shown in Figure 40 and Figure 42, further highlighting this variability, and reflecting complex scattering in the ice-water system.

During the fully frozen period in mid-winter, alpha values decrease, close to 0° with tighter boxplots indicating a more homogeneous ice cover and stable surface scattering from the ice-water interface. This trend is further supported by decreasing IQR values in Figure 40 and Figure 42, showing reduced variability in alpha values during this period.

.

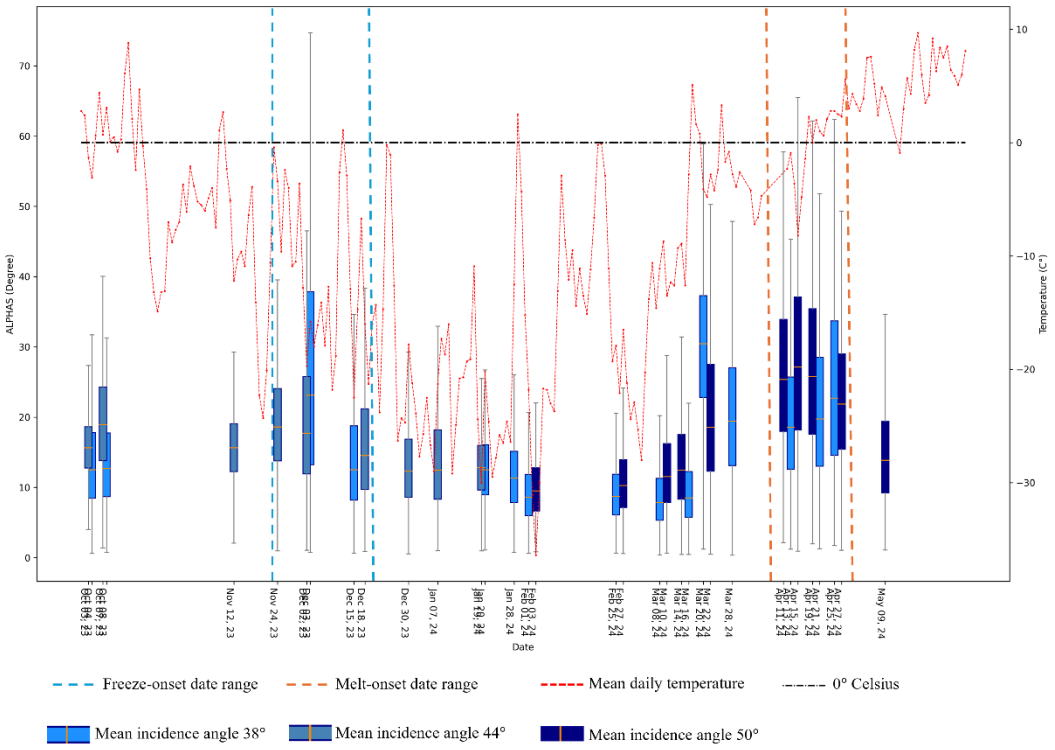


Figure 39. Whisker Plot of Alpha Angle (α) at Study Site 1, Kluane Lake, from October 2023 to May 2024. This plot shows alpha values in degrees across incidence angles (38°, 44°, and 50°),

with mean daily temperature (red dashed line) and a 0°C reference line. Vertical dashed lines mark the freeze-onset and melt-onset date ranges.

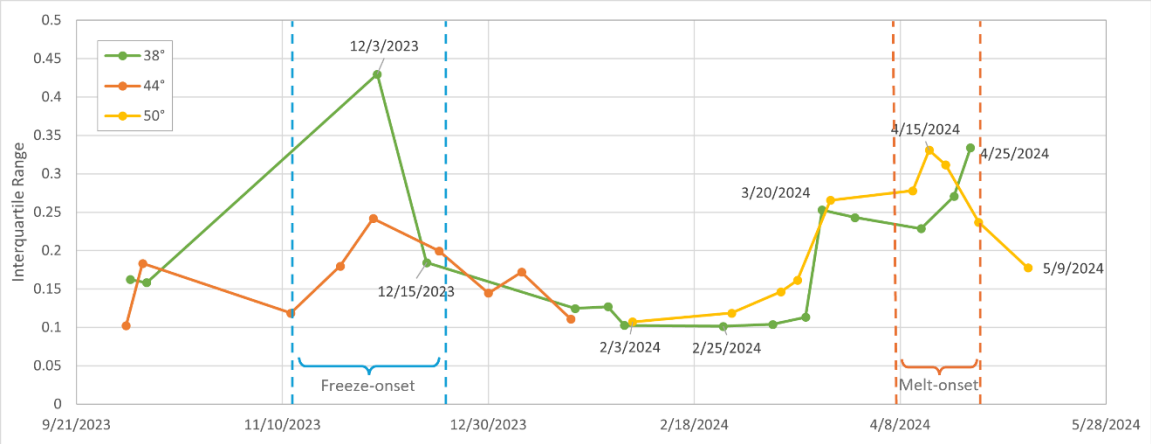


Figure 40. Temporal variation of the interquartile range (IQR) for the Alpha Angle at Kluane Lake, Site 1 (October 2023–May 2024), calculated for incidence angles 38°, 44°, and 50°, with vertical dashed lines indicating freeze-onset and melt-onset date ranges.

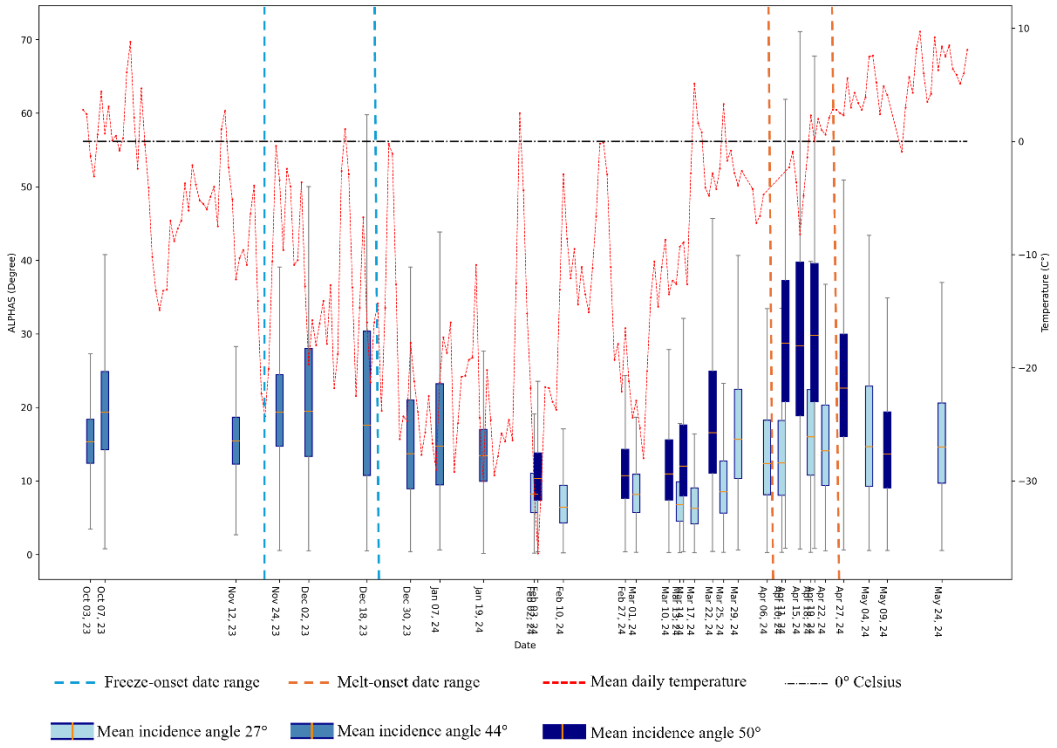


Figure 41. Whisker Plot of Alpha Angle (α) at Study Site 2, Kluane Lake, from October 2023 to May 2024. This plot presents alpha values with incidence angles (27°, 44°, and 50°), mean daily temperature, and freeze/melt-onset date ranges.

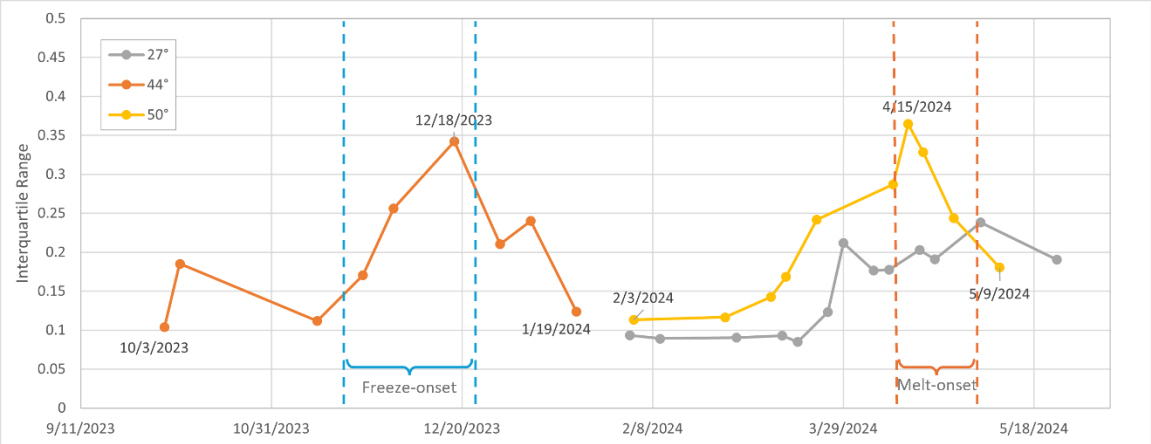


Figure 42. Temporal variation of the interquartile range (IQR) for the Alpha Angle at Kluane Lake, Site 2 (October 2023–May 2024), calculated for incidence angles 27°, 44°, and 50°, with vertical dashed lines indicating freeze-onset and melt-onset date ranges.

Kluane Lake is a relatively large lake, so it is expected that different lake areas will exhibit different behaviors. Figure 43 (Study Site 1) and Figure 44 (Study Site 2) depict alpha values across Kluane Lake on key dates.

- October 3 & 4, 2023: Alpha values are low and near zero values, consistent with calm open water conditions, this is also reflected in the backscatter of this region in early October acquisitions (-25 dB).
- December 2 to December 18, 2023: As temperatures drop and ice formation begins, alpha values increase, indicating volume scattering, particularly in the southern lake areas where skim ice is broken up and stacked due to strong southerly sustained wind gusts.
- February 2 & 3, 2024: During peak winter, when the lake is fully frozen, alpha values drop to near zero, reflecting surface bounce interactions. Backscatter during this period has increased since the lake has frozen (-10 dB). The combination of higher backscatter and evidence of surface bounce with minimal variability is consistent with single-bounce interactions with the ice-water interface (Atwood et al., 2015). The uniformity of the surface is also evident in Figure 30.

- April 19 & 21, 2024: Alpha values rise again with the onset of melting, indicating increased volume scattering as meltwater begins to pool on the ice surface and incorporate into the snowpack.
- May 24, 2024: Near the end of the melting period, alpha values slightly decrease, showing a shift towards a more randomly oriented surface as the ice layer diminishes.

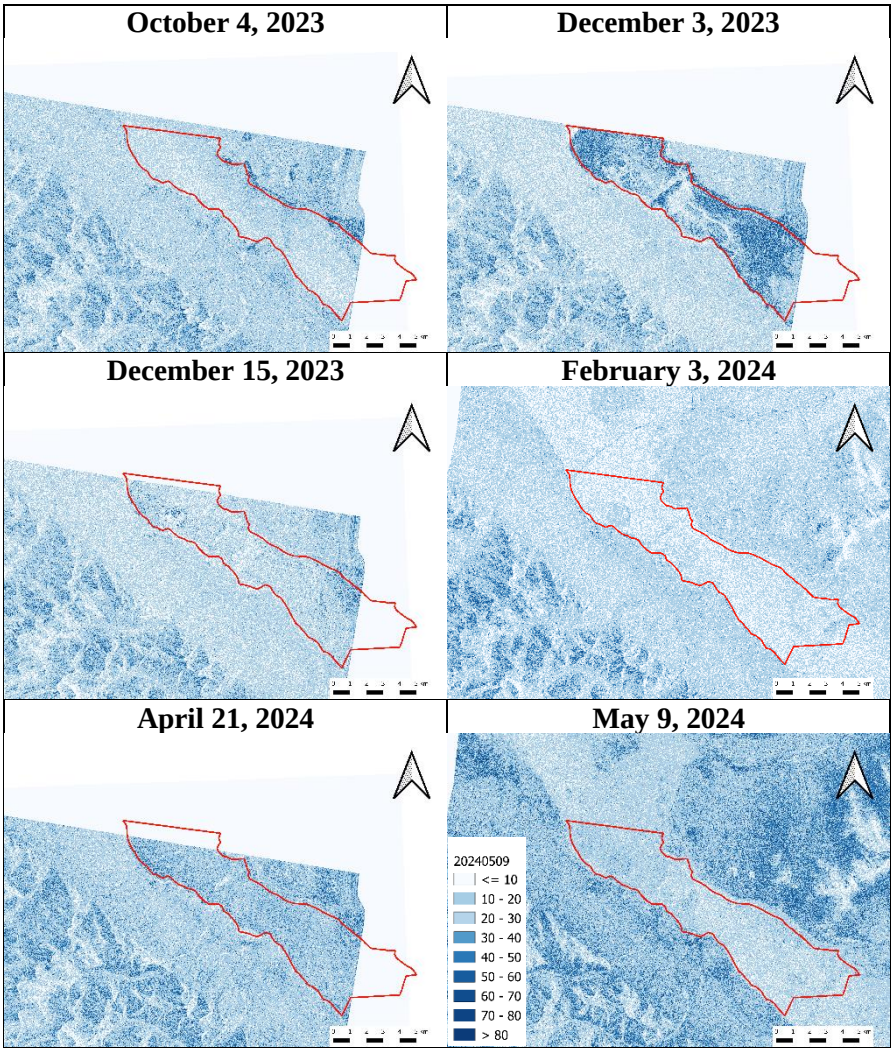


Figure 43. Alpha Angle Values in Degree for Study Site 1, Kluane Lake, from October 2023 to May 2024.

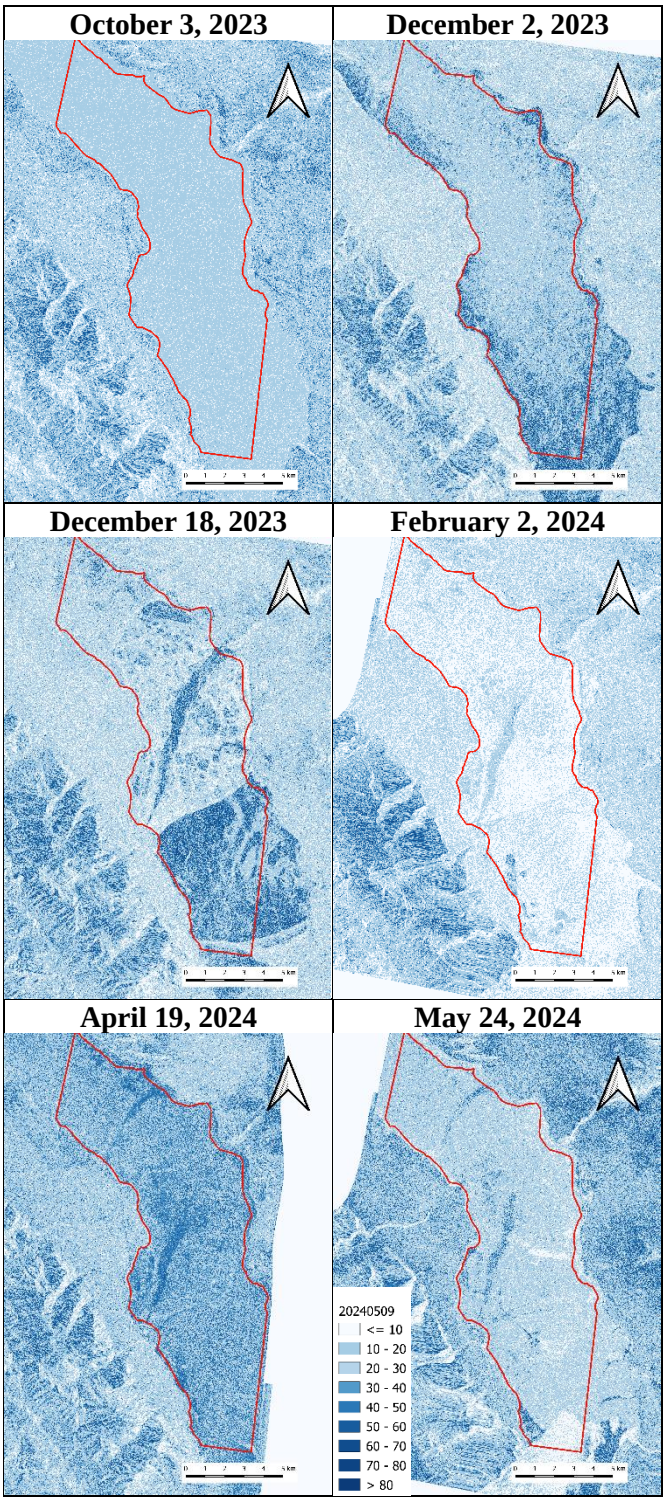


Figure 44. Alpha Values in Degrees for Study Site 2, Kluane Lake, from October 2023 to May 2024.

4.6 Discussion

The monitoring of lake ice phenology in this study, employing the first difference method for analyzing backscatter data alongside Compact Polarimetric (CP) parameter analysis, demonstrates the application of RADARSAT Constellation Mission (RCM) data for monitoring freeze and melt cycles in sub-Arctic lakes. These results align with and expand upon previous research in SAR-based lake ice monitoring (Murfitt & Duguay, 2020; Surdu et al., 2015), showcasing the robustness of RCM data in capturing phenological events through SAR backscatter changes and polarimetric parameters.

4.6.1 Backscatter Analysis and Phenological Event Detection

The first difference method applied to CP RCM SAR acquisitions, proved effective in identifying freeze-onset and melt-onset events across the study sites. The backscatter trends displayed distinct patterns during these periods, with sharp decreases observed at melt-onset and steady declines during freeze-onset. These trends align with established findings in lake ice phenology, demonstrating consistency with studies by Geldsetzer et al. (2010) and Murfitt et al. (2018), which have shown similar backscatter evolution during freeze-up and break-up periods. The sensitivity of SAR backscatter to surface conditions, as demonstrated in this study, underscores its utility in capturing rapid transitions in lake ice states, particularly during dynamic freeze-up and break-up periods.

Wind dynamics also play a critical role in lake ice formation and distribution (M. Jeffries et al., 2013), as highlighted by the case of Kluane Lake. The predominant southerly winds influence ice behavior significantly, pushing newly formed ice from the southern regions towards the northern parts of the lake. This wind-driven redistribution can delay the complete freeze-over of the southern areas, illustrating how local meteorological factors interact with ice formation processes. Such interactions emphasize the complex relationship between environmental factors and lake ice phenology.

By examining the freeze-onset and melt-onset maps (Figure 12 and Figure 15), a clear spatial pattern emerges: the northern section of the selected area, which froze earlier in the season, also experienced earlier thawing. This spatial variability highlights the consistent seasonal pattern and the importance of considering local conditions in lake ice studies.

The comparison of melt-onset maps from 2023 and 2024 (Figure 15 and Figure 19), underscores the importance of temporal resolution in lake ice monitoring. The analysis of spring 2023, benefiting from a dataset with more frequent acquisitions, enabled the algorithm to track consecutive drops in

backscatter intensity with greater precision, providing a more detailed and continuous representation of the melt progression. In contrast, the limited temporal coverage in 2024 may have hindered the detection of additional events, such as potential refreeze events following the initial melt-onset. These findings highlight the critical value of higher temporal resolution data for accurately capturing transitional events during melt seasons.

4.6.2 Compact Polarimetric Parameters and Surface Conditions

The use of Compact Polarimetric (CP) SAR at Kluane Lake provides valuable insights into lake ice phenology, capturing both surface and subsurface changes across freeze-up, mid-winter, and melt-onset phases. These findings align with studies that demonstrate the utility of CP SAR in tracking seasonal transitions in cryospheric environments (Charbonneau et al., 2010; Dabboor & Shokr, 2021). By applying CP SAR to a freshwater lake system, this study builds on earlier research highlighting the sensitivity of polarimetric parameters to changes in surface roughness, ice-water interfaces, and internal ice properties (Geldsetzer et al., 2015).

Degree of Polarization (DoP)

The degree of polarization (DoP) effectively captures variations in surface roughness and homogeneity across different lake ice phenology phases, providing key insights into the evolving ice conditions at Kluane Lake. As shown in Figure 24 and Figure 25, lower and more variable DoP values during the early freeze-up period correspond to open water conditions, driven by daily temperatures above freezing. The roughness of wind-driven waves leads to depolarization, particularly at higher incidence angles. This behavior aligns with C-band radar observations reported by Geldsetzer and van der Sanden (2013), who noted that open water surfaces produce increased backscatter variability and reduced polarization coherence due to Bragg scattering mechanisms on rough water surfaces.

During the mid-winter period, DoP values remain consistently high, indicating a smooth, homogeneous ice surface typical of consolidated ice cover. This stability suggests minimal surface roughness, reflecting a uniform dielectric profile across the ice, as previously noted by Geldsetzer et al. (2015), who associated high DoP values with stable ice structures.

As ice begins to melt during the melt-onset phase, DoP values drop significantly, highlighting the formation of liquid water inclusions and rougher surface textures. This increased depolarization is attributed to the dielectric contrast between ice and water, which amplifies the radar interaction with

the surface. Similar trends have been observed in sea ice studies, where melting ice leads to a mix of volume scattering and surface roughness effects, resulting in lower DoP values (Dabboor & Shokr, 2021).

DoP values also provide insight into how reflectance varies with incidence angles across different surface types. As shown in Figure 1, the reflectivity of different surfaces shows varying sensitivity to incidence angles. For instance, at an ice/water interface, reflectivity remains relatively unchanged with variations in the angle, whereas on a snow/ice-covered surface, reflectivity decreases significantly as the angle increases. This characteristic is crucial for interpreting DoP behavior across different phases of lake ice phenology.

The whisker plot in Figure 25 further illustrates this relationship. On May 9 and May 24, 2024, despite variations in incidence angles, DoP values remain similar, indicating that the surface is predominantly an ice/water interface during this period. In contrast, between February and April 2024, a step change in DoP values is observed, corresponding to variations in incidence angle, suggesting the presence of a snow/ice surface. This trend underscores the role of dielectric properties and incidence angles in shaping polarization response, highlighting their influence on radar backscatter behavior.

Circular Polarization Ratio

The circular polarization ratio emerged as a valuable metric for tracking surface roughness during freeze-onset and melt-onset phases. The lower yet variable CPR values observed in Figure 26 and Figure 28 during the early period indicate open water surfaces, as further confirmed by Planet imagery showing an ice-free lake in Figure 30 (Top-Left).

As ice begins to form, CPR values increase, reflecting the development of rough, mixed ice structures with ice-water layers. This behavior aligns with Campbell (2012), who demonstrated that higher CPR values result from multiple scattering mechanisms on rough surfaces, including cracks and partially frozen layers. Additionally, Raney et al. (2021) highlighted the effectiveness of CPR in detecting heterogeneous surfaces during transitional phases when volume and surface scattering mechanisms coexist.

During the mid-winter period, CPR values stabilize and decrease, reflecting the thickening and consolidation of ice, with reduced variability indicating a stable ice cover and fewer surface changes. The stabilization of CPR values during mid-winter can be linked to the growth of larger, well-oriented

ice crystals through the process of geometric selection (Shumskii, 1964). As ice crystals with preferential orientations replace less stable crystals, the ice cover becomes more homogeneous, reducing surface roughness and the potential for volume scattering. This process is also evident in the narrowing of the interquartile range (IQR) in CPR values (Figure 27and Figure 29) during mid-winter. The growth of larger, columnar ice crystals further reduces the dielectric variability within the ice. The decrease in dielectric variability results in more consistent radar backscatter and lower CPR variability.

During the melt-onset phase, CPR values rise again as the ice surface transitions from a stable, consolidated state to a more dynamic, water-saturated structure. The formation of cracks, air pockets, and liquid inclusions within the melting ice introduces dielectric heterogeneity, which enhances volume scattering (Carte, 1961). These physical changes amplify radar backscatter in the same circular polarization and explain the observed increase in CPR values during this period. Additionally, surface meltwater and wet snow contribute to elevated CPR readings by increasing surface roughness and promoting the formation of secondary ice layers like snow ice and congealed frazil slush, which enhance scattering complexity during melt (Michel & Ramseier, 1971). Studies on river ice breakup by Geldsetzer et al. (2024) similarly found that CPR, is particularly sensitive to surface changes during thaw periods, reinforcing the relevance of CPR as a reliable indicator of melt onset.

The sensitivity of CPR to incidence angle further influences its effectiveness in ice monitoring. As discussed by Zhang et al., (2016), CPR values tend to increase with increasing incidence angle, especially when examining thinner ice layers. This effect is most prominent at lower angles, where CPR is more responsive to small variations in surface conditions, making it especially useful for capturing the early stages of ice formation (Zhang et al., 2016). CPR values at Kluane Lake were analyzed across incidence angles of 38°, 44°, and 50° at Study Site 1, and 27°, 44°, and 50° at Study Site 2, demonstrating this sensitivity. The same trend is presented in Figure 26 and Figure 28, where on closely related dates, the CPR values are often higher for larger incidence angles.

Relative Phase (δ)

The Relative Phase (δ) offered stable and reliable insights into scattering mechanisms during lake ice transitions. Compared to CPR and DoP, δ values demonstrated lower variability across environmental and angular conditions, making it a robust indicator of stable ice cover. Figure 33 and Figure 35 show a mix of small and medium boxplots in the early period, reflecting variations in surface roughness caused by wind-driven waves on open water. During windy conditions, δ values exhibit

greater variability due to more complex scattering, whereas calm conditions result in smaller boxplots, indicating uniform scattering.

The type of scattering mechanism associated with δ values varies depending on the phase difference between the right-hand (RH) and left-hand (RV) circular polarizations. Surface scattering typically occurs when the phase difference between the RH and RV components is near zero, which is common over smooth surfaces, such as newly formed ice during freeze-up (Cloude & Pottier, 1996). In contrast, a positive phase difference (RH leading RV) indicates volume scattering, which is often observed over snow-covered ice or wet areas, where radar signals penetrate into the medium. This volume scattering increases when highly dielectric materials, such as water, are present, further enhancing radar interactions. On the other hand, negative δ values (RV leading RH) suggest double-bounce scattering, which typically occurs when radar waves reflect off vertical structures, such as ice ridges or cracks (Ballester-Berman & Lopez-Sanchez, 2012). However, in this study, double-bounce scattering was not dominant within the analyzed region.

In mid-winter, δ values displayed minimal variability, with reduced IQR values indicating a stable ice cover under consistent freezing conditions. This stability arises from the consolidated ice surface and uniform dielectric properties, which minimize changes in surface roughness and scattering complexity. These characteristics align with findings by Charbonneau et al. (2010) and Geldsetzer & Van Der Sanden (2013), which associate low phase variability with stable subsurface integrity.

In transitional phases, such as freeze-onset and melt-onset, δ values remain positive but exhibit increased variability due to changes in surface conditions. During the spring melt, rising liquid water content increases the dielectric permittivity, enhancing radar backscatter and altering phase characteristics. This can lead to pronounced fluctuations in δ, with occasional shifts toward extreme values near π or –π, reflecting the dynamic nature of melting ice and water interfaces.

The overall stability of δ during mid-winter, contrasted with its variability during freeze-onset and melt-onset, underscores its effectiveness as a parameter for monitoring lake ice conditions. Its ability to remain consistent across environmental and angular variations further highlights its value in characterizing ice phenology events.

Alpha Angle (α)

The Alpha Angle (α) values offered insights into scattering shifts during freeze-onset, mid-winter stability, and melt-onset phases, helping to distinguish between surface and volume scattering. Throughout mid-winter, α demonstrated lower values and narrower interquartile ranges, corresponding to a consolidated ice structure with minimal variability in scattering mechanisms. Geldsetzer et al. (2015) observed similar behavior over stable ice covers, where reduced surface roughness and minimal subsurface inclusions resulted in lower alpha values and diminished volume scattering.

During freeze-onset and melt-onset, higher α values indicated volume scattering, suggesting a more complex, heterogeneous structure. During the melt season, when the snowpack increases in moisture and much of the signal is scattered and attenuated within the snowpack during the transition from pendular to funicular snow melt, the alpha values increase towards 45° which is more analogous to volume scatter. The classification of polarimetric parameters by Geldsetzer et al. (2024) further supports the relevance of α in ice monitoring. In their study of river ice breakup, α was categorized as a parameter sensitive to polarization differences and potentially linked to resonant Bragg scattering. It was shown to respond to variations in surface roughness and polarization, reflecting complex scattering conditions during transitional phases.

The α analysis further confirms the absence of double-bounce scattering across all dates, as shown in Figure 39 and Figure 41. This absence is consistent with findings from recent studies (Gunn et al., 2018; Gunn, 2015), which highlight that the roughness of the ice-water boundary plays a dominant role in backscatter, even without vertically aligned tubular bubbles or planar interfaces that typically support double-bounce scattering. The lack of pronounced double-bounce signals in the polarimetric parameter results for Kluane Lake suggests that surface and volume scattering mechanisms are the primary contributors to radar backscatter during the observed phases.

The sensitivity of Alpha to environmental conditions, such as incidence angle, is also notable. Lower incidence angles emphasize surface scattering, while higher angles enhance volume scattering. This trend is particularly evident in Figure 41, especially between the narrow incidence angle of 27° and the wider angle of 50°. This makes Alpha a critical parameter for interpreting ice phenology events under varying observational conditions.

4.6.3 Limitations

Although RCM provides frequent revisit times over certain areas, the temporal resolution remains limited in some areas due to standard coverage maps. This can result in large gaps during critical periods of rapid ice transitions, particularly during freeze-onset. For instance, phenological events in Kluane Lake may have been more precisely tracked with higher temporal resolution, as temporal gaps can lead to interpolation errors when determining the exact timing of freeze and melt events. Previous studies (Murfitt & Duguay, 2020) have noted that high temporal resolution is essential for accurately capturing dynamic lake ice processes, and thus, incorporating data from other SAR missions could enhance temporal coverage.

This study utilized Landsat-9 and Planet imagery for validation; however, these sources have their own limitations, including lower revisit rates and cloud cover constraints, which can restrict their utility during certain phenological periods. The absence of high-resolution, high-frequency optical data may constrain the validation accuracy of SAR-derived freeze and melt dates. Incorporating additional data sources, in-situ observations, or ground-based measurements could improve the accuracy of the validation process.

4.7 – Conclusion

This study used two methods, the First Difference algorithm and Compact Polarimetric (CP) parameter analysis with RADARSAT Constellation Mission (RCM) data, to monitor lake ice changes, with a focus on Kluane Lake as the main site. The integration of these methods provided a comprehensive view of freeze-onset and melt-onset patterns and further insights into surface scattering mechanisms.

The First Difference method relies on temporal shifts in backscatter intensity from RADARSAT Constellation Mission (RCM) data to identify key phenological events, such as freeze-onset and melt-onset. At Kluane Lake, freeze-onset and melt-onset periods were mapped based on significant drops in backscatter intensity. Freeze-onset was observed to progress from north to south, beginning in late November and concluding by mid-December 2023. Similarly, the melt-onset period, starting in the northern part of the lake continued southward throughout May.

In Ryan and Landing Lakes, the First Difference method revealed the influence of lake depth on melting patterns, with Ryan Lake, being deeper, experiencing a prolonged melt process extending into late May, while the shallow Landing Lake melted earlier. Validation using Landsat-9 and Planet

imagery confirmed the freeze and melt timelines, particularly at Kluane Lake, where changes in surface temperatures confirmed RCM-derived observations.

The CP parameter analysis provided additional insights into lake ice dynamics, offering a more detailed understanding of surface and subsurface characteristics compared to the First Difference method. RCM images from October 2023 to May 2024 were analyzed for four key parameters: Degree of Polarization (DoP), Circular Polarization Ratio (CPR), Relative Phase, and Alpha Angle. Each parameter contributed unique insights into surface and subsurface conditions. The most commonly observed pattern among all CP parameters was the stabilization of values during mid-winter, consistently indicating minimal surface roughness and a coherent, solid or snow-covered ice surface.

DoP values were used to assess surface roughness, with higher values indicating smoother ice surfaces in mid-winter and lower values corresponding to open water or melting phases. CPR tracked surface texture, with high values during freeze-up and break-up phases reflecting increased surface roughness and low values indicating stable ice cover. Relative Phase showed low variability during mid-winter highlighting its ability to characterize stable ice cover, while increased variability during freeze-onset and melt-onset captured transitions in ice structure, such as wind-driven roughness and meltwater infiltration. Alpha Angle differentiated scattering types, showing higher values during freeze and melt periods due to volume scattering and lower values during mid-winter when solid ice dominated.

Chapter 5
Conclusion

5.1 Overall Summary

This study explored the use of RADARSAT Constellation Mission (RCM) compact polarimetric (CP) data to monitor lake ice phenology in three sub-Arctic lakes in Canada, focusing on Kluane Lake as the primary site. By employing the first difference method and CP parameter analysis, this research identified freeze-onset and melt-onset periods while also capturing detailed surface and subsurface dynamics. The first difference method effectively mapped phenological events, with validation from Landsat thermal imagery and Planet data demonstrating strong agreement.

CP parameter analysis provided additional insights into ice behavior throughout the seasonal cycle. DoP and CPR proved sensitive to surface roughness, capturing transitions during freeze-up and melt-onset. Relative Phase and Alpha Angle highlighted changes in scattering mechanisms, offering a nuanced understanding of subsurface conditions. A key observation across all parameters was the stabilization of CP parameter values during mid-winter, reflecting minimal surface roughness and a cohesive, solid ice cover. These findings underscore the utility of compact polarimetry in enhancing the accuracy and depth of lake ice monitoring.

5.2 Limitations

One of the primary challenges in this study was the temporal resolution of RCM data. Although the RCM constellation is designed to capture images every four days, this temporal resolution was not consistently maintained across all regions due to standard coverage maps. The inconsistency in image acquisition during critical periods of freezing or thawing posed a significant challenge, as it could lead to missed opportunities for capturing key backscatter changes, thereby affecting the accuracy of phenological event detection. This issue is particularly important for smaller lakes. Due to their smaller surface area, they are more rapidly influenced by environmental factors such as wind, radiation, and temperature fluctuations. This can result in multiple freeze-thaw cycles within a short period. To accurately monitor these changes, it is crucial to have high temporal resolution imagery.

The second limitation of this research was the challenges associated with using meteorological data from the Kluane Lake Research Station weather station to validate the freeze-onset and melt-onset dates

extracted across Kluane Lake. While climate data was available, it was incomplete for the critical periods of freeze and melt analyzed in this study. Additionally, the meteorological data from Burwash Landing weather station was insufficient to force thermodynamic lake ice models due to missing key variables, such as cloud cover. These data limitations restricted the ability to fully validate the extracted dates, though they do not reduce the broader applicability of the results.

Despite the high spatial resolution of the RCM data used in this study, with resolutions of 5 m and 16 m, the accuracy is somewhat limited. The backscatter behavior in adjacent pixels shows discrepancies, which reduces the precision of the method, particularly for smaller lakes such as Landing and Ryan Lakes.

5.3 Future Directions

To overcome the temporal resolution restriction of RCM images, future research might integrate and enhance RCM images with multiple remote sensing platforms, such as optical, thermal, and other SAR sensors, providing a more comprehensive perspective of lake ice dynamics. Combining these different types of data can help fill temporal gaps and offer cross-validation to improve the robustness of phenological event detection.

Ground-based measurements and observations can supplement satellite data, resulting in higher resolution and more frequent monitoring. Automated weather stations and time-lapse cameras placed around the research lakes can provide useful in-situ data for validating and improving satellite observations. Such data could also improve understanding of localized climatic influences on lake ice dynamics.

Since the results of this study for Kluane Lake were more reliable compared to Ryan and Landing Lakes. An algorithm for smaller lakes may be adapted and improved to give more precise modeling of the freeze and melt processes in these smaller bodies of water. These efforts could address the unique dynamics of smaller lakes, where spatial resolution and localized environmental factors often present challenges.

Future studies could benefit from incorporating RR (Right Circular Transmit, Right Circular Receive) and RL (Right Circular Transmit, Left Circular Receive) polarizations to enhance lake ice monitoring by capturing unique scattering mechanisms during critical phases of ice formation and decay. These circular polarizations provide valuable insights into the dielectric and structural changes

in the ice, particularly during freeze-onset and melt-onset, when complex scattering mechanisms dominate.

RR polarization, with its sensitivity to coherent volume scattering, is well-suited for detecting stable and uniform ice layers. During freeze-onset, RR can help identify areas of consistent ice growth by detecting coherent scattering from vertically elongated ice crystals that grow downward into the water column (Michel & Ramseier, 1971). This is especially useful in distinguishing between newly formed thin ice and more stable, thicker ice layers, improving the accuracy of ice thickness measurements and stability assessments.

RL polarization, on the other hand, excels at capturing depolarization caused by heterogeneous and transitional ice conditions. During freeze-onset, the initial formation of ice involves the development of primary ice crystals with randomly oriented c-axes, leading to significant variations in the dielectric properties of the ice (Shumskii, 1964). These random orientations increase radar signal depolarization, which RL can effectively detect, allowing researchers to monitor the early stages of ice formation and identify transitions from open water to ice cover.

During melt-onset, RL polarization is particularly valuable in detecting changes caused by the infiltration of meltwater into the snowpack and the formation of slush layers. As meltwater percolates through the snowpack, it transitions from pendular to funicular phases, creating a highly variable dielectric environment that increases radar depolarization (Bengtsson, 1986). The formation of snow ice, characterized by a granular texture and numerous air bubbles, further enhances depolarization. Snow ice most commonly forms when snow cover on thin ice decompresses the ice, causing water to flood the surface through cracks or holes, leading to slush formation that subsequently freezes (Schwarz et al., 1986). Additionally, rain or melting snow can cause slush formation within the lower layers of the snowpack, contributing to snow ice development. These features increase depolarization and enhance cross-polarization signals due to the complex scattering caused by spherical bubbles and slush layers (Murfitt & Duguay, 2021; Gunn et al., 2017) . RL polarization can detect these structural complexities, highlighting areas where melt/refreeze cycles are occurring and providing critical insights into melt progression.

Further exploration of CP parameters, particularly their sensitivity to incidence angle and environmental conditions, could significantly enhance their application in cryospheric studies. Incidence angle influences CP parameters such as Circular Polarization Ratio (CPR) and Degree of

Polarization (DoP). Lower incidence angles amplify surface roughness effects, making them suitable for detecting subtle changes during transitional periods, while higher angles highlight volume scattering and subsurface features. Systematic investigation of how these parameters respond to different incidence angles and surface conditions could improve understanding of their capabilities and limitations.

Similarly, environmental factors, such as wind, snow cover, and the presence of meltwater, introduce variability in CP parameter values. For example, wind-driven roughness on open water surfaces can affect DoP and Relative Phase values, while snow cover alters scattering mechanisms, influencing Alpha Angle and CPR. Understanding how these environmental conditions interact with radar signals could refine the interpretation of CP parameter trends across different stages of the ice cycle. By addressing these aspects, future research could optimize the use of CP parameters to better capture the complex interactions between ice, water, and atmospheric processes in polar and sub-Arctic regions.

Furthermore, CP parameters can enhance understanding of ice evolution, improve environmental monitoring, and support applications like ice road safety. Future research could explore using the minimum variability of CP parameters during mid-winter as a measure for assessing ice road safety. By systematically investigating these periods of stability, it may be possible to develop predictive tools for evaluating ice road conditions and mitigating risks for northern communities reliant on such infrastructure.

References

Adams, W. P. (1976). Field determination of the densities of lake ice sheets. *Limnology and Oceanography*, *21*(4), 602–608.

Adrian, R., Hessen, D. O., Blenckner, T., Hillebrand, H., Hilt, S., Jeppesen, E., Livingstone, D. M., & Trolle, D. (2016). Environmental Impacts—Lake Ecosystems. In M. Quante & F. Colijn (Eds.), *North Sea Region Climate Change Assessment* (pp. 315–340). Springer International Publishing. https://doi.org/10.1007/978-3-319-39745-0_10

Ashton, G. D. (1986). *River and Lake Ice Engineering*. Water Resources Publication. https://books.google.ca/books?hl=en&lr=&id=xglYVjAsnt8C&oi=fnd&pg=PR11&ots=JVEuB9MGYF&sig=fhNj3ohVAmSXKvk-idI4ghZJzus&redir_esc=y#v=onepage&q&f=false

Asselstine, C., Beaudry, C., Drummond, R., Kabanak, K., & Taylor, S. (2013). *LAKE TROUT AND LAKE WHITEFISH POPULATION ASSESSMENT KLUANE LAKE 2013 Yukon Fish and Wildlife Branch TR-14-04*.

Atwood, D. K., Gunn, G. E., Roussi, C., Wu, J., Duguay, C., & Sarabandi, K. (2015). Microwave Backscatter From Arctic Lake Ice and Polarimetric Implications. *IEEE Transactions on Geoscience and Remote Sensing*, *53*(11), 5972–5982. https://doi.org/10.1109/TGRS.2015.2429917

Ballester-Berman, J. D., & Lopez-Sanchez, J. M. (2012). Time Series of Hybrid-Polarity Parameters Over Agricultural Crops. *IEEE Geoscience and Remote Sensing Letters*, *9*(1), 139–143. https://doi.org/10.1109/LGRS.2011.2162312

Bengtsson, L. (1986). Spatial Variability of Lake Ice Covers. *Geografiska Annaler: Series A, Physical Geography*, *68*(1–2), 113–121. https://doi.org/10.1080/04353676.1986.11880164

Brown, L. C., & Duguay, C. R. (2010). The response and role of ice cover in lake-climate interactions. *Progress in Physical Geography: Earth and Environment*, *34*(5), 671–704. https://doi.org/10.1177/0309133310375653

Brown, L. C., & Duguay, C. R. (2012). Modelling Lake Ice Phenology with an Examination of Satellite-Detected Subgrid Cell Variability. *Advances in Meteorology*, *2012*, 1–19. https://doi.org/10.1155/2012/529064

Campbell, B. A. (2012). High circular polarization ratios in radar scattering from geologic targets. *Journal of Geophysical Research: Planets*, *117*(E6), 2012JE004061. https://doi.org/10.1029/2012JE004061

Carte, A. (1961). Air Bubbles in Ice. *Proceedings of the Physical Society*, *77*, 757. https://doi.org/10.1088/0370-1328/77/3/327

Chander, G., Markham, B. L., & Helder, D. L. (2009). Summary of current radiometric calibration coefficients for Landsat MSS, TM, ETM+, and EO-1 ALI sensors. *Remote Sensing of Environment*, *113*(5), 893–903. https://doi.org/10.1016/j.rse.2009.01.007

Charbonneau, F. J., Brisco, B., Raney, R. K., McNairn, H., Liu, C., Vachon, P. W., Shang, J., DeAbreu, R., Champagne, C., Merzouki, A., & Geldsetzer, T. (2010). Compact polarimetry overview and applications assessment. *Canadian Journal of Remote Sensing*, *36*(sup2), S298–S315. https://doi.org/10.5589/m10-062

Cloude, S. (2009). *Polarisation: Applications in Remote Sensing*. Oxford University Press. https://doi.org/10.1093/acprof:oso/9780199569731.001.0001

Cloude, S. R. & Pottier, E. (1996). A review of target decomposition theorems in radar polarimetry. *IEEE Transactions on Geoscience and Remote Sensing*, *34*(2), 498–518. https://doi.org/10.1109/36.485127

Curry, J. A., Schramm, J. L., & Ebert, E. E. (1993). Impact of clouds on the surface radiation balance of the Arctic Ocean. *Meteorology and Atmospheric Physics*, *51*, 197–217.

Dabboor, M., & Shokr, M. (2021). Sensitivity of Compact Polarimetric SAR Parameters to Modeled Lake Ice Growth. *IEEE Transactions on Geoscience and Remote Sensing*, *59*(12), 9953–9967. https://doi.org/10.1109/TGRS.2021.3050754

Debye, P. (1929). Polar molecules, the chemical catalog company. *Inc., New York*, *89*.

Duguay, C. R., Bernier, M., Gauthier, Y., & Kouraev, A. (2014). Remote sensing of lake and river ice. In M. Tedesco (Ed.), *Remote Sensing of the Cryosphere* (pp. 273–306). John Wiley & Sons, Ltd. https://doi.org/10.1002/9781118368909.ch12

Duguay, C. R., Bernier, M., Gauthier, Y., & Kouraev, A. (2015). Remote sensing of lake and river ice. In M. Tedesco (Ed.), *Remote Sensing of the Cryosphere* (1st ed., pp. 273–306). Wiley. https://doi.org/10.1002/9781118368909.ch12

Duguay, C. R., Flato, G. M., Jeffries, M. O., Ménard, P., Morris, K., & Rouse, W. R. (2003). Ice-cover variability on shallow lakes at high latitudes: Model simulations and observations. *Hydrological Processes*, *17*(17), 3465–3483. https://doi.org/10.1002/hyp.1394

Duguay, C. R., Prowse, T. D., Bonsal, B. R., Brown, R. D., Lacroix, M. P., & Ménard, P. (2006). Recent trends in Canadian lake ice cover. *Hydrological Processes*, *20*(4), 781–801. https://doi.org/10.1002/hyp.6131

Duguay, C. R., Pultz, T. J., Lafleur, P. M., & Drai, D. (2002). RADARSAT backscatter characteristics of ice growing on shallow sub-Arctic lakes, Churchill, Manitoba, Canada. *Hydrological Processes*, *16*(8), 1631–1644. https://doi.org/10.1002/hyp.1026

Ellison, W. J., Lamkaouchi, K., & Moreau, J.-M. (1996). Water: A dielectric reference. *Journal of Molecular Liquids*, *68*(2–3), 171–279. https://doi.org/10.1016/0167-7322(96)00926-9

Evans, S. (1965). Dielectric Properties of Ice and Snow–a Review. *Journal of Glaciology*, *5*(42), 773–792. https://doi.org/10.3189/S0022143000018840

Geldsetzer, T., Arkett, M., Zagon, T., Charbonneau, F., Yackel, J. J., & Scharien, R. K. (2015). All-Season Compact-Polarimetry C-band SAR Observations of Sea Ice. *Canadian Journal of Remote Sensing*, *41*(5), 485–504. https://doi.org/10.1080/07038992.2015.1120661

Geldsetzer, T., Sanden, J. V. D., & Brisco, B. (2010). Monitoring lake ice during spring melt using RADARSAT-2 SAR. *Canadian Journal of Remote Sensing*, *36*(sup2), S391–S400. https://doi.org/10.5589/m11-001

Geldsetzer, T., Svacina, N., Tolszczuk-Leclerc, S., & Van Der Sanden, J. (2024). River ice breakup classification using dual- (HH&HV) or compact-polarization RADARSAT Constellation Mission data. *Remote Sensing of Environment*, *312*, 114313. https://doi.org/10.1016/j.rse.2024.114313

Geldsetzer, T., & Van Der Sanden, J. J. (2013). Identification of polarimetric and nonpolarimetric C-band SAR parameters for application in the monitoring of lake ice freeze-up. *Canadian Journal of Remote Sensing*, *39*(3), 263–275. https://doi.org/10.5589/m13-033

Golden, D. M., Audet, C., & Smith, M. A. (Peggy). (2015). "Blue-ice": Framing climate change and reframing climate change adaptation from the indigenous peoples' perspective in the northern boreal forest of Ontario, Canada. *Climate and Development*, *7*(5), 401–413. https://doi.org/10.1080/17565529.2014.966048

Gunn, G., Duguay, C., Derksen, C., Clausi, D., & Toose, P. (2017). Investigating the Influence of Variable Freshwater Ice Types on Passive and Active Microwave Observations. *Remote Sensing*, *9*(12), 1242. https://doi.org/10.3390/rs9121242

Gunn, G. E. (2015). *Re-evaluating Scattering Mechanisms in Snow-Covered Freshwater Lake Ice Containing Bubbles Using Polarimetric Ground-based and Spaceborne Radar Data*.

Gunn, G. E., Duguay, C. R., Atwood, D. K., King, J., & Toose, P. (2018). Observing Scattering Mechanisms of Bubbled Freshwater Lake Ice Using Polarimetric RADARSAT-2 (C-Band) and UW-Scat (X- and Ku-Bands). *IEEE Transactions on Geoscience and Remote Sensing*, *56*(5), 2887–2903. https://doi.org/10.1109/TGRS.2017.2786158

Hall, D. K., Fagre, D. B., Klasner, F. L., Linebaugh, G. H., & Liston, G. E. (1994). Analysis of ERS 1 synthetic aperture radar data of frozen lakes in northern Montana and implications for climate studies. *Journal of Geophysical Research*, *99*, 22473–22482.

Heron, R., & Woo, M.-K. (1994). Decay of a High Arctic lake-ice cover: Observations and modelling. *Journal of Glaciology*, *40*(135), 283–292. https://doi.org/10.3189/S0022143000007371

Hewitt, B. (2019). Effects of climate change on lake ice freeze up across the Northern Hemisphere: Historical patterns and future predictions.

Hoekstra, M., Jiang, M., Clausi, D. A., & Duguay, C. (2020). Lake Ice-Water Classification of RADARSAT-2 Images by Integrating IRGS Segmentation with Pixel-Based Random Forest Labeling. *Remote Sensing*, *12*(9), 1425. https://doi.org/10.3390/rs12091425

Howell, S. E. L., Brown, L. C., Kang, K.-K., & Duguay, C. R. (2009). Variability in ice phenology on Great Bear Lake and Great Slave Lake, Northwest Territories, Canada, from SeaWinds/QuikSCAT: 2000–2006. *Remote Sensing of Environment*, *113*(4), 816–834. https://doi.org/10.1016/j.rse.2008.12.007

Howell, S. E. L., Scharien, R. K., Landy, J., & Brady, M. (2020). Spring melt pond fraction in the Canadian Arctic Archipelago predicted from RADARSAT-2. *The Cryosphere*, *14*(12), 4675–4686. https://doi.org/10.5194/tc-14-4675-2020

Jeffries, M., Morris, K., & Kozlenko, N. (2013). Ice Characteristics and Processes, and Remote Sensing of Frozen Rivers and Lakes. In C. R. Duguay & A. Pietroniro (Eds.), *Geophysical Monograph Series* (pp. 63–90). American Geophysical Union. https://doi.org/10.1029/163GM05

Jeffries, M., Morris, K., & Liston, G. E. (1996). A Method To Determine Lake Depth and Water Availability on the North Slope of Alaska with Spaceborne Imaging Radar and Numerical Ice Growth Modelling. *ARCTIC*, *49*(4), 367–374. https://doi.org/10.14430/arctic1212

Jeffries, M., Morris, K., Weeks, W., & Wakabayashi, H. (1994). Structural and stratigraphie features and ERS 1 synthetic aperture radar backscatter characteristics of ice growing on shallow lakes in NW Alaska, winter 1991–1992. *Journal of Geophysical Research Atmospheres*, *99*. https://doi.org/10.1029/94JC01479

Jeffries, M. O., Morris, K., & Kozlenko, N. (2013). Ice Characteristics and Processes, and Remote Sensing of Frozen Rivers and Lakes. In C. R. Duguay & A. Pietroniro (Eds.), *Geophysical Monograph Series* (pp. 63–90). American Geophysical Union. https://doi.org/10.1029/163GM05

Jimenez-Munoz, J. C., & Sobrino, J. A. (2010). A Single-Channel Algorithm for Land-Surface Temperature Retrieval From ASTER Data. *IEEE Geoscience and Remote Sensing Letters*, *7*(1), 176–179. https://doi.org/10.1109/LGRS.2009.2029534

Kincaid, D. W., Adair, E. C., Joung, D., Stockwell, J. D., & Schroth, A. W. (2022). Ice cover and thaw events influence nitrogen partitioning and concentration in two shallow eutrophic lakes. *Biogeochemistry*, *157*(1), 15–29. https://doi.org/10.1007/s10533-021-00872-x

Knoll, L. B., Sharma, S., Denfeld, B. A., Flaim, G., Hori, Y., Magnuson, J. J., Straile, D., & Weyhenmeyer, G. A. (2019). Consequences of lake and river ice loss on cultural ecosystem services. *Limnology and Oceanography Letters*, *4*(5), 119–131. https://doi.org/10.1002/lol2.10116

Lenormand, F., Duguay, C. R., & Gauthier, R. (2002). Development of a historical ice database for the study of climate change in Canada. *Hydrological Processes*, *16*(18), 3707–3722. https://doi.org/10.1002/hyp.1235

Lopez, L. S., Hewitt, B. A., & Sharma, S. (2019). Reaching a breaking point: How is climate change influencing the timing of ice breakup in lakes across the northern hemisphere? *Limnology and Oceanography*, *64*(6), 2621–2631. https://doi.org/10.1002/lno.11239

Magnuson, J. J., Robertson, D. M., Benson, B. J., Wynne, R. H., Livingstone, D. M., Arai, T., Assel, R. A., Barry, R. G., Card, V., Kuusisto, E., Granin, N. G., Prowse, T. D., Stewart, K. M., & Vuglinski, V. S. (2000). Historical Trends in Lake and River Ice Cover in the Northern Hemisphere. *Science*, *289*(5485), 1743–1746. https://doi.org/10.1126/science.289.5485.1743

Mahmud, M. S., Geldsetzer, T., Howell, S. E. L., Yackel, J. J., Nandan, V., & Scharien, R. K. (2018). Incidence Angle Dependence of HH-Polarized C- and L-Band Wintertime

Backscatter Over Arctic Sea Ice. *IEEE Transactions on Geoscience and Remote Sensing*, *56*(11), 6686–6698. https://doi.org/10.1109/TGRS.2018.2841343

Ménard, P., Duguay, C. R., Flato, G. M., & Rouse, W. R. (2002). Simulation of ice phenology on Great Slave Lake, Northwest Territories, Canada. *Hydrological Processes*, *16*(18), 3691–3706. https://doi.org/10.1002/hyp.1230

Michel, B., & Ramseier, R. O. (1971). Classification of river and lake ice. *Canadian Geotechnical Journal*, *8*(1), 36–45. https://doi.org/10.1139/t71-004

Mladenova, I. E., Jackson, T. J., Bindlish, R., & Hensley, S. (2013). Incidence Angle Normalization of Radar Backscatter Data. *IEEE Transactions on Geoscience and Remote Sensing*, *51*(3), 1791–1804. https://doi.org/10.1109/TGRS.2012.2205264

Morris, K., Jeffries, M., & Weeks, W. F. (1995). Ice processes and growth history on Arctic and sub-Arctic lakes using ERS-1 SAR data. *Polar Record*, *31*(177), 115–128. https://doi.org/10.1017/S0032247400013619

Mullan, D., Swindles, G., Patterson, T., Galloway, J., Macumber, A., Falck, H., Crossley, L., Chen, J., & Pisaric, M. (2017). Climate change and the long-term viability of the World's busiest heavy haul ice road. *Theoretical and Applied Climatology*, *129*(3–4), 1089–1108. https://doi.org/10.1007/s00704-016-1830-x

Murfitt, J., Brown, L. C., & Howell, S. E. L. (2018). Evaluating RADARSAT-2 for the Monitoring of Lake Ice Phenology Events in Mid-Latitudes. *Remote Sensing*, *10*(10), 1641. https://doi.org/10.3390/rs10101641

Murfitt, J., Duguay, C., Picard, G., & Gunn, G. (2023). Forward modelling of synthetic aperture radar backscatter from lake ice over Canadian Subarctic Lakes. *Remote Sensing of Environment*, *286*, 113424. https://doi.org/10.1016/j.rse.2022.113424

Murfitt, J., & Duguay, C. R. (2020). Assessing the Performance of Methods for Monitoring Ice Phenology of the World's Largest High Arctic Lake Using High-Density Time Series Analysis of Sentinel-1 Data. *Remote Sensing*, *12*(3), 382. https://doi.org/10.3390/rs12030382

Murfitt, J., & Duguay, C. R. (2021). 50 years of lake ice research from active microwave remote sensing: Progress and prospects. *Remote Sensing of Environment*, *264*, 112616. https://doi.org/10.1016/j.rse.2021.112616

Nasonova, S., Scharien, R. K., Geldsetzer, T., Howell, S. E. L., & Power, D. (2018). Optimal Compact Polarimetric Parameters and Texture Features for Discriminating Sea Ice Types during Winter and Advanced Melt. *Canadian Journal of Remote Sensing*, *44*(4), 390–411. https://doi.org/10.1080/07038992.2018.1527683

Planet Team (2022). Planet Application Program Interface: In Space for Life on Earth. San Francisco, CA. https://api.planet.com

Ragotzkie, R. A. (1978). Heat Budgets of Lakes. In A. Lerman (Ed.), *Lakes* (pp. 1–19). Springer New York. https://doi.org/10.1007/978-1-4757-1152-3_1

Raney, R. K. (2007). Hybrid-Polarity SAR Architecture. *IEEE Transactions on Geoscience and Remote Sensing*, *45*(11), 3397–3404. https://doi.org/10.1109/TGRS.2007.895883

Raney, R. K., Brisco, B., Dabboor, M., & Mahdianpari, M. (2021). RADARSAT Constellation Mission's Operational Polarimetric Modes: A User-Driven Radar Architecture. *Canadian Journal of Remote Sensing*, *47*(1), 1–16. https://doi.org/10.1080/07038992.2021.1907566

Rouse, W. R., Blanken, P. D., Eaton, A. K., Petrone, R. M., Schertzer, W. M., & Spence, C. (2000). Energy and water balance of high latitude surfaces. *MAGS: Final Reports and Proceedings, 6th Scientific Workshop for MAGS, 1517*.

Schwarz, J., Frederking, R., Goodman, D. J., Gow, A., Kohnen, H., Reuter, H., Schwerdtfeger, B., & Sinha, N. K. (1986). Ice physics. In *River and Lake Ice Engineering* (pp. 19–85). Water Resources Publications Littleton, CO.

Shumskii, P. A. (1964). *Principles of structural glaciology:(trans, from Russian by David Kraus) New York*. Dover Publications, Inc.

Skrunes, S., Brekke, C., & Eltoft, T. (2012). Oil spill characterization with multi-polarization C- and X-band SAR. *2012 IEEE International Geoscience and Remote Sensing Symposium*, 5117–5120. https://doi.org/10.1109/IGARSS.2012.6352459

Sobrino, J. A., Jiménez-Muñoz, J. C., & Paolini, L. (2004). Land surface temperature retrieval from LANDSAT TM 5. *Remote Sensing of Environment*, *90*(4), 434–440. https://doi.org/10.1016/j.rse.2004.02.003

Spence, C., & Hedstrom, N. (2018). *Hydrometeorological data from Baker Creek Research Watershed, Northwest Territories, Canada*.

Surdu, C., Duguay, C., Pour, H., & Brown, L. (2015). Ice Freeze-up and Break-up Detection of Shallow Lakes in Northern Alaska with Spaceborne SAR. *Remote Sensing*, *7*(5), 6133–6159. https://doi.org/10.3390/rs70506133

Truong-Loi, M.-L, Freeman, A., Dubois-Fernandez, P. C., & Pottier, E. (2009). Estimation of Soil Moisture and Faraday Rotation From Bare Surfaces Using Compact Polarimetry. *IEEE Transactions on Geoscience and Remote Sensing*, *47*(11), 3608–3615. https://doi.org/10.1109/TGRS.2009.2031428

Ulaby, F. T., Moore, R. K., & Fung, A. K. (1986). *Microwave Remote Sensing: Active and Passive, Radar Remote Sensing and Surface Scattering and Emission Theory* (Vol. 2). Addison-Wesley.

Van Der Sanden, J. J., & Geldsetzer, T. (2015). Compact Polarimetry in Support of Lake Ice Breakup Monitoring: Anticipating the RADARSAT Constellation Mission. *Canadian Journal of Remote Sensing*, *41*(5), 440–457. https://doi.org/10.1080/07038992.2015.1104637

Wang, X., & Key, J. R. (2005). Arctic Surface, Cloud, and Radiation Properties Based on the AVHRR Polar Pathfinder Dataset. Part II: Recent Trends. *Journal of Climate*, *18*(14), 2575–2593. https://doi.org/10.1175/JCLI3439.1

Weeks, W. F., Fountain, A. G., Bryan, M. L., & Elachi, C. (1978). Differences in radar return from ice-covered North Slope Lakes. *Journal of Geophysical Research: Oceans*, *83*(C8), 4069–4073. https://doi.org/10.1029/JC083iC08p04069

Weyhenmeyer, G. A., Meili, M., & Livingstone, D. M. (2004). Nonlinear Temperature Response of Lake Ice Breakup. *Geophysical Research Letters*. https://doi.org/10.1029/2004gl019530

Williams, G. P. (1965). Correlating Freeze-Up and Break-Up with Weather Conditions. *Canadian Geotechnical Journal*, *2*(4), 313–326. https://doi.org/10.1139/t65-047

Woodhouse, I. H. (2012). Polarimetric radar imaging: From basics to applications by Jong-Sen Lee and Eric Pottier. *International Journal of Remote Sensing*, *33*(1), 333–334. https://doi.org/10.1080/01431161.2010.519925

Woolway, R. I., Huang, L., Sharma, S., Lee, S., Rodgers, K. B., & Timmermann, A. (2022). Lake Ice Will Be Less Safe for Recreation and Transportation Under Future Warming. *Earth's Future*, *10*(10), e2022EF002907. https://doi.org/10.1029/2022EF002907

Zhang, X., Dierking, W., Zhang, J., Meng, J., & Lang, H. (2016). Retrieval of the thickness of undeformed sea ice from simulated C-band compact polarimetric SAR images. *The Cryosphere*, *10*(4), 1529–1545. https://doi.org/10.5194/tc-10-1529-2016

Appendix A
Compact Polarimetric Whisker Plots

This appendix provides a supplementary analysis of Compact Polarimetric (CP) parameters that were not the primary focus of the main study but offer additional insights into the scattering mechanisms and ice dynamics at Kluane Lake. Whisker plots for these parameters are presented for Study Sites 1 and 2, covering the period from October 2023 to May 2024. These plots serve as a reference for interpreting secondary metrics and exploring trends that might further enhance our understanding of lake ice phenology.

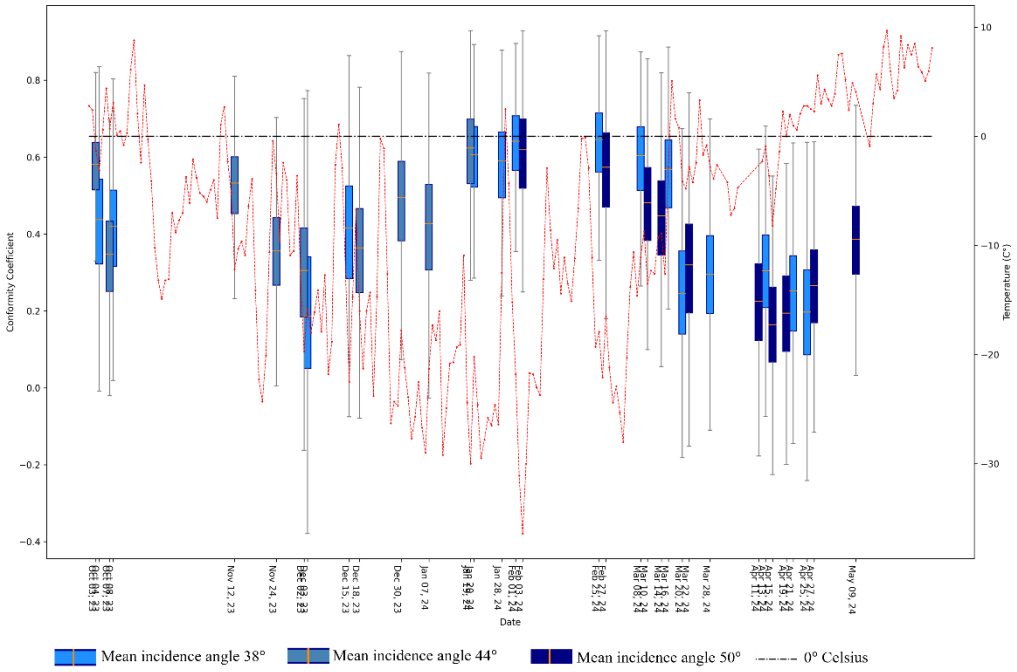


Figure 45. Whisker Plot of Conformity Coefficient at Study Site 1, Kluane Lake, from October 2023 to May 2024.

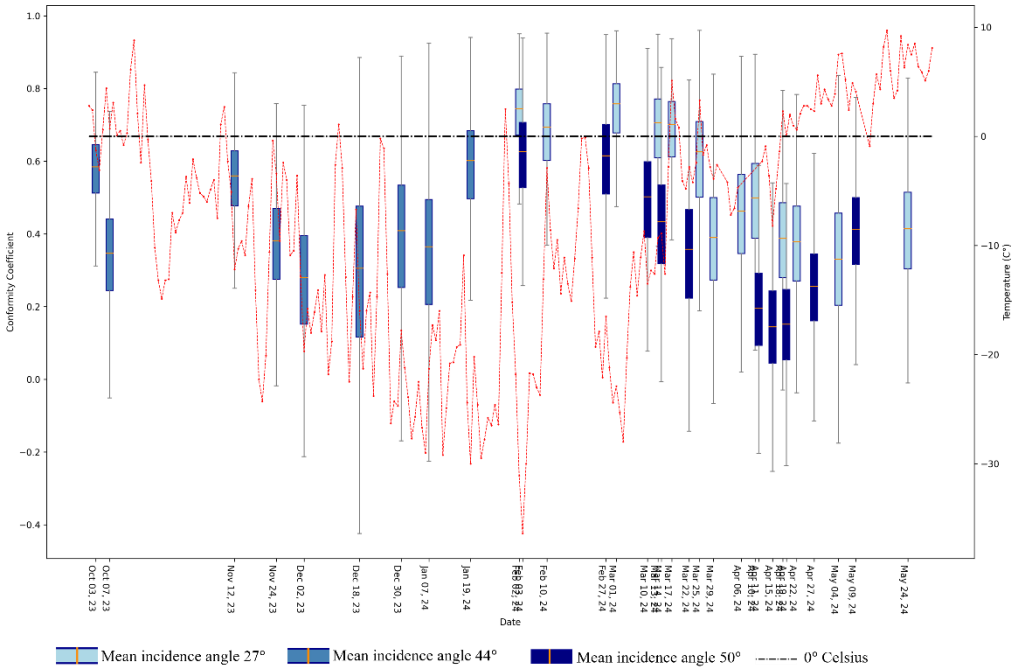


Figure 46. Whisker Plot of Conformity Coefficient at Study Site 2, Kluane Lake, from October 2023 to May 2024.

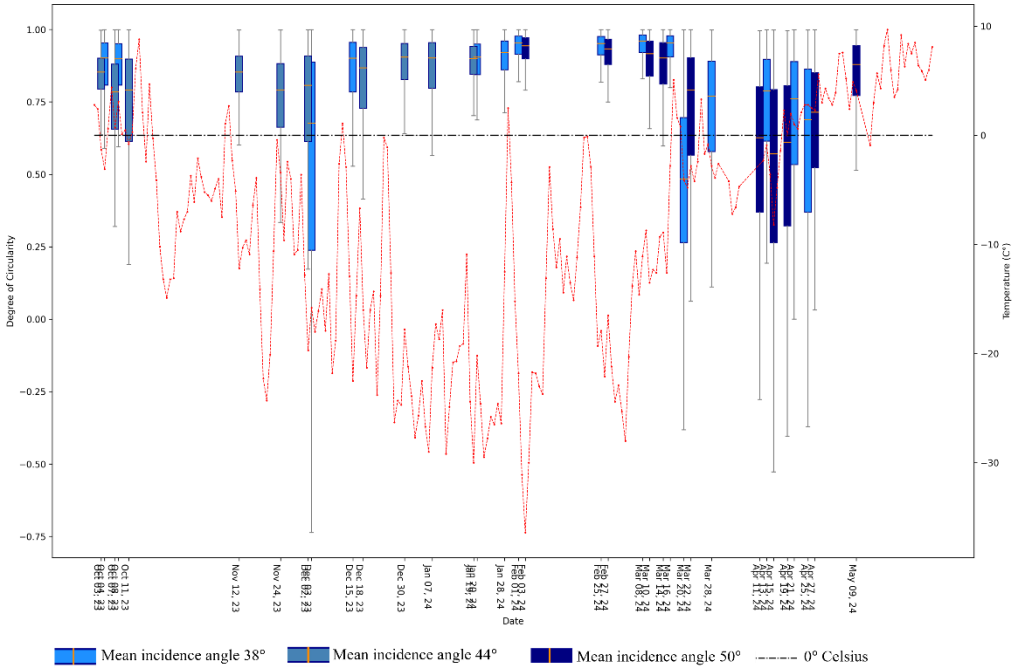


Figure 47. Whisker Plot of Degree of Circularity at Study Site 1, Kluane Lake, from October 2023 to May 2024.

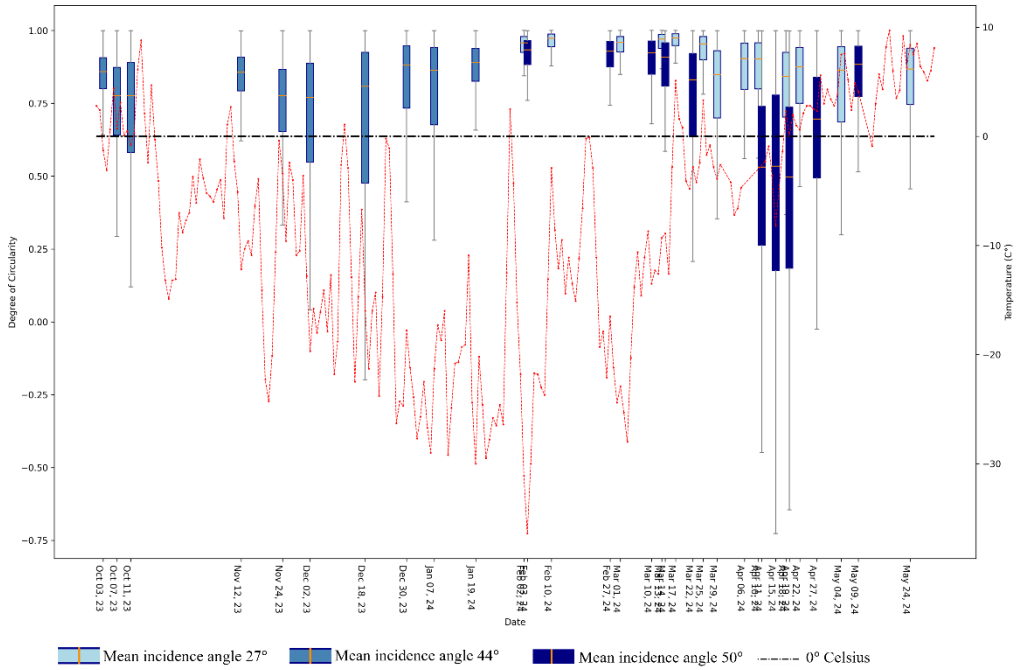


Figure 48. Whisker Plot of Degree of Circularity at Study Site 2, Kluane Lake, from October 2023 to May 2024.

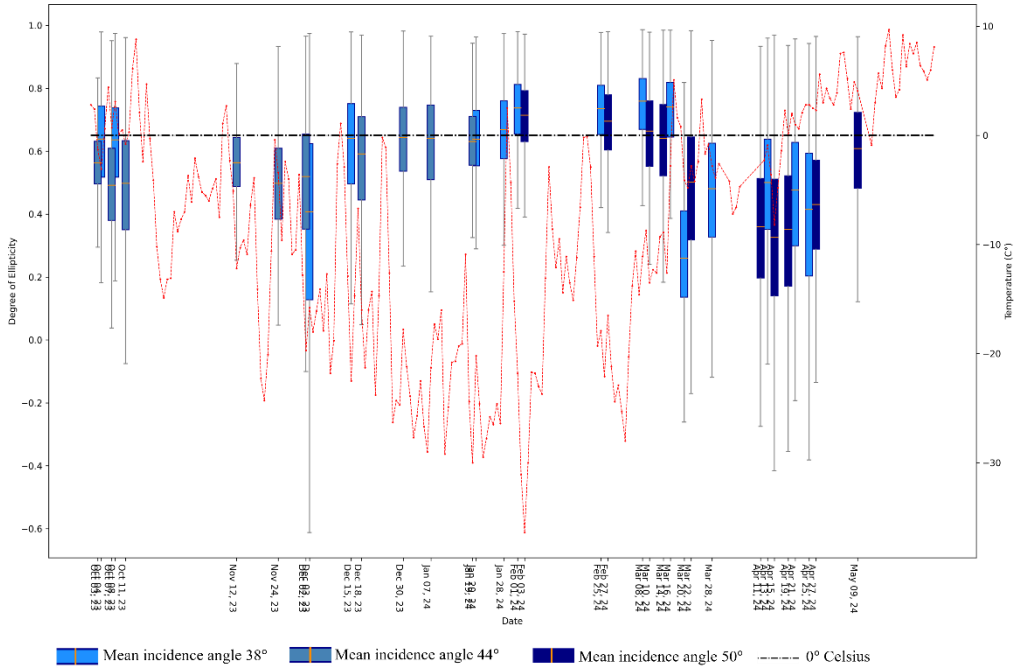


Figure 49. Whisker Plot of Degree of Ellipticity at Study Site 1, Kluane Lake, from October 2023 to May 2024.

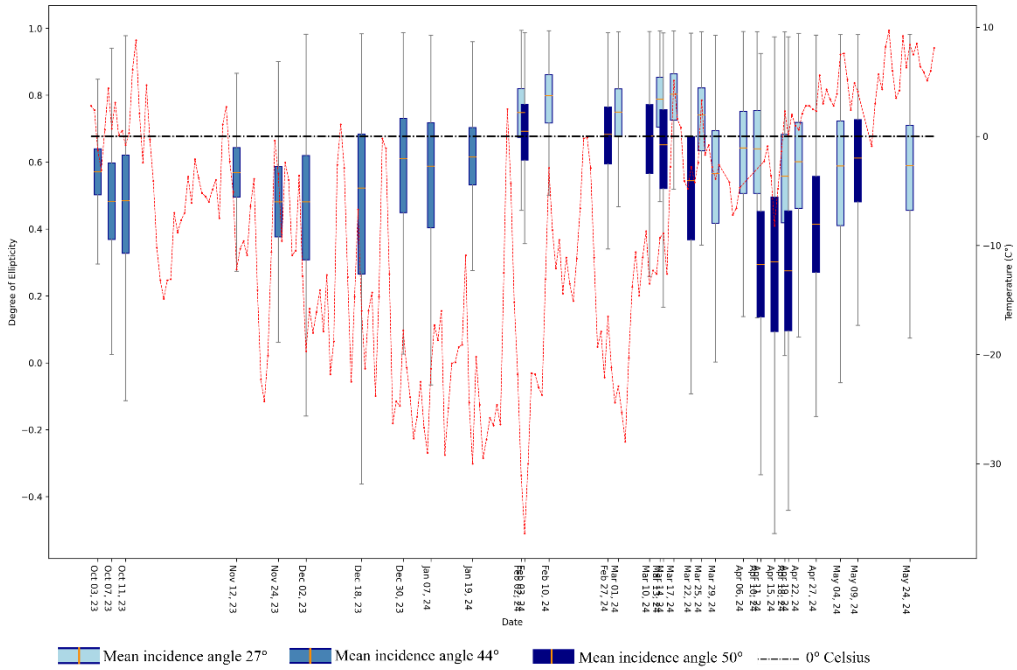


Figure 50. Whisker Plot of Degree of Ellipticity at Study Site 2, Kluane Lake, from October 2023 to May 2024.

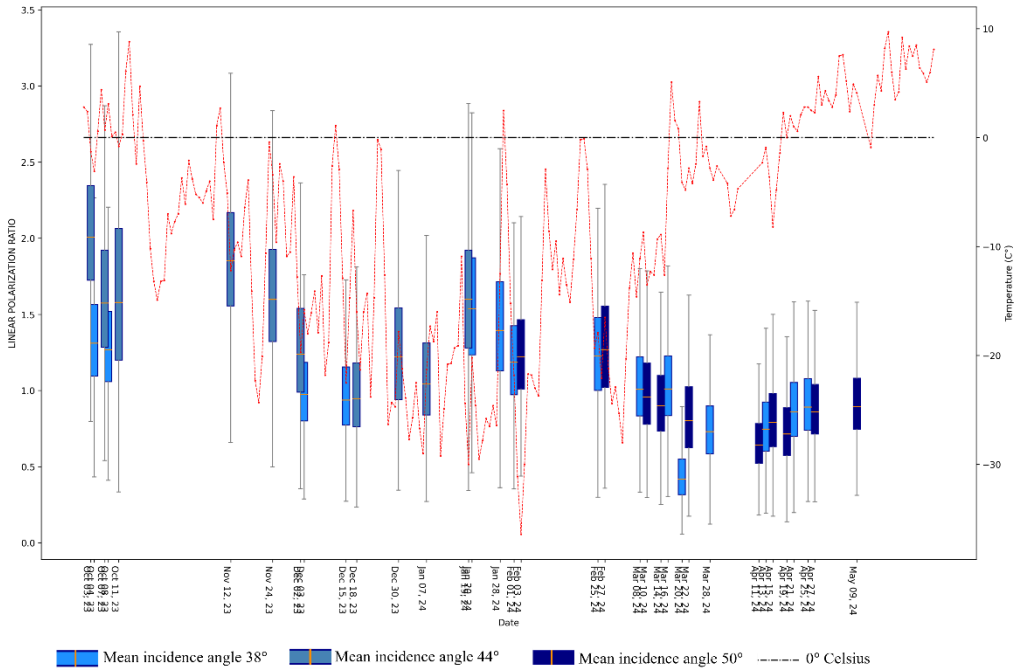


Figure 51. Whisker Plot of Linear Polarization Ratio at Study Site 1, Kluane Lake, from October 2023 to May 2024

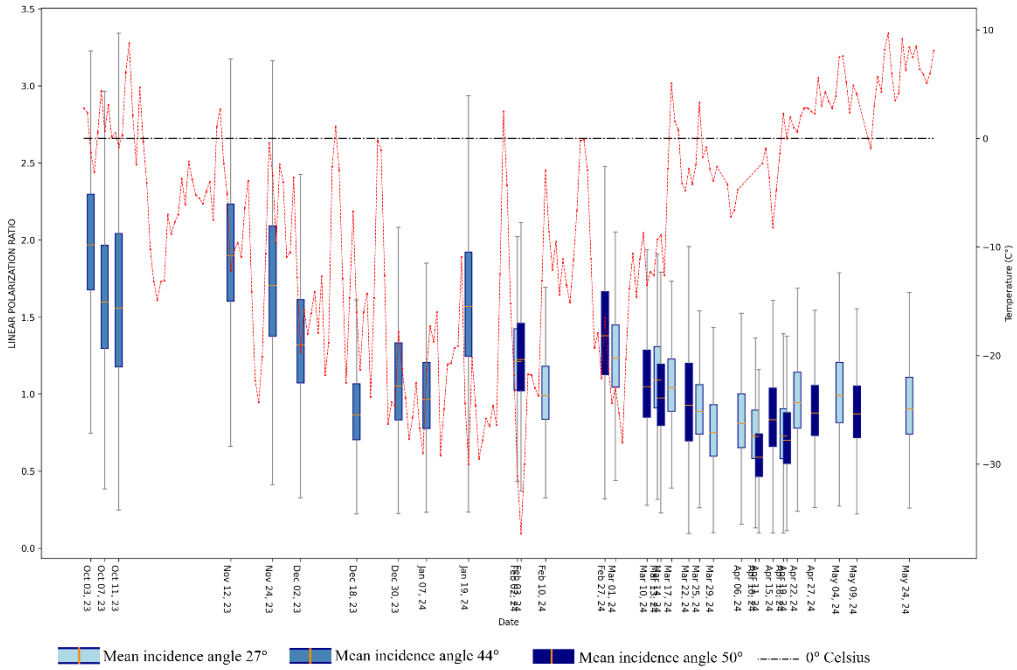


Figure 52. Whisker Plot of Linear Polarization Ratio at Study Site 2, Kluane Lake, from October 2023 to May 2024

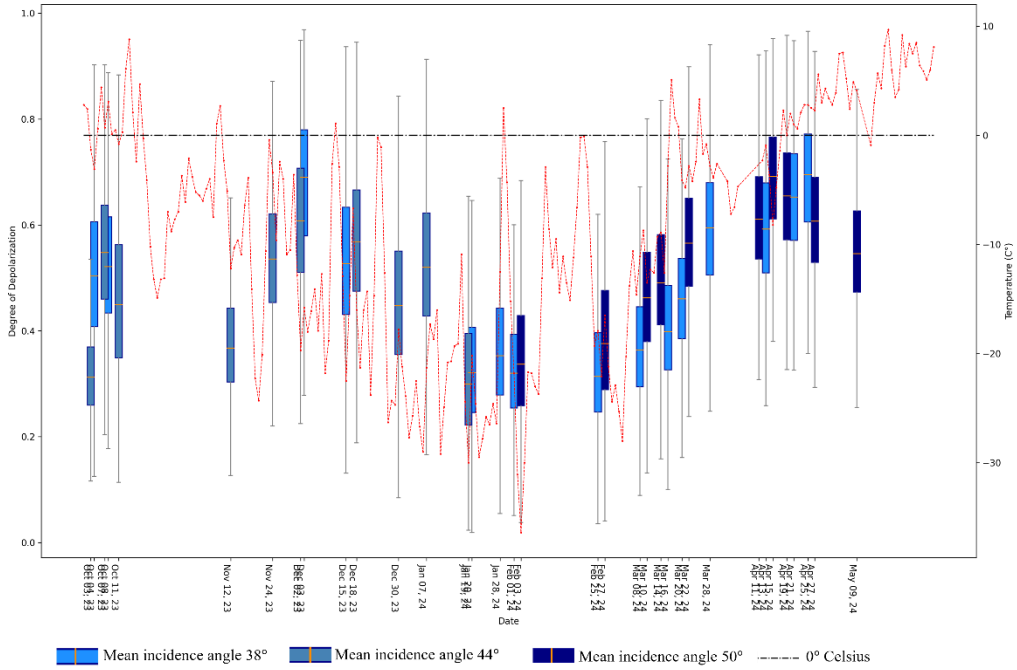


Figure 53. Whisker Plot of Degree of Depolarization at Study Site 1, Kluane Lake, from October 2023 to May 2024.

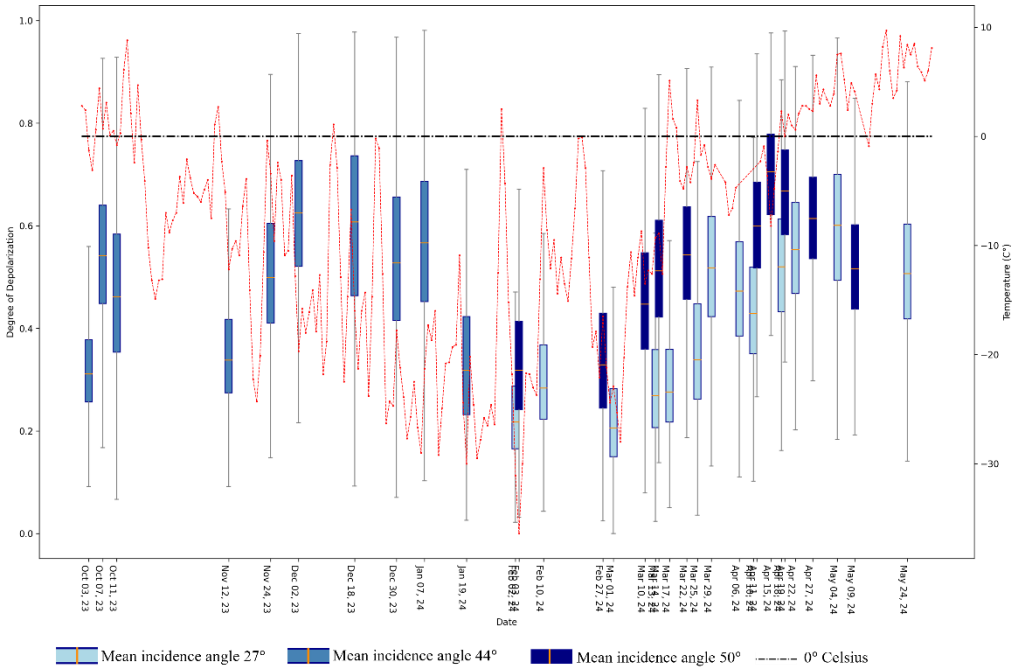


Figure 54. Whisker Plot of Degree of Depolarization at Study Site 2, Kluane Lake, from October 2023 to May 2024.

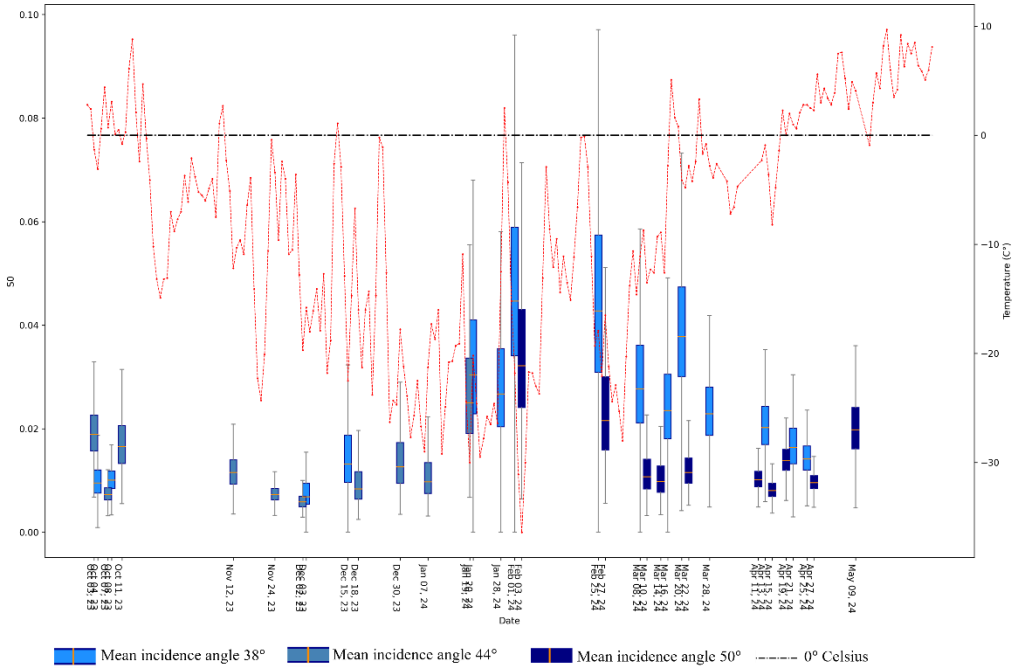


Figure 55. Whisker Plot of S0 at Study Site 1, Kluane Lake, from October 2023 to May 2024.

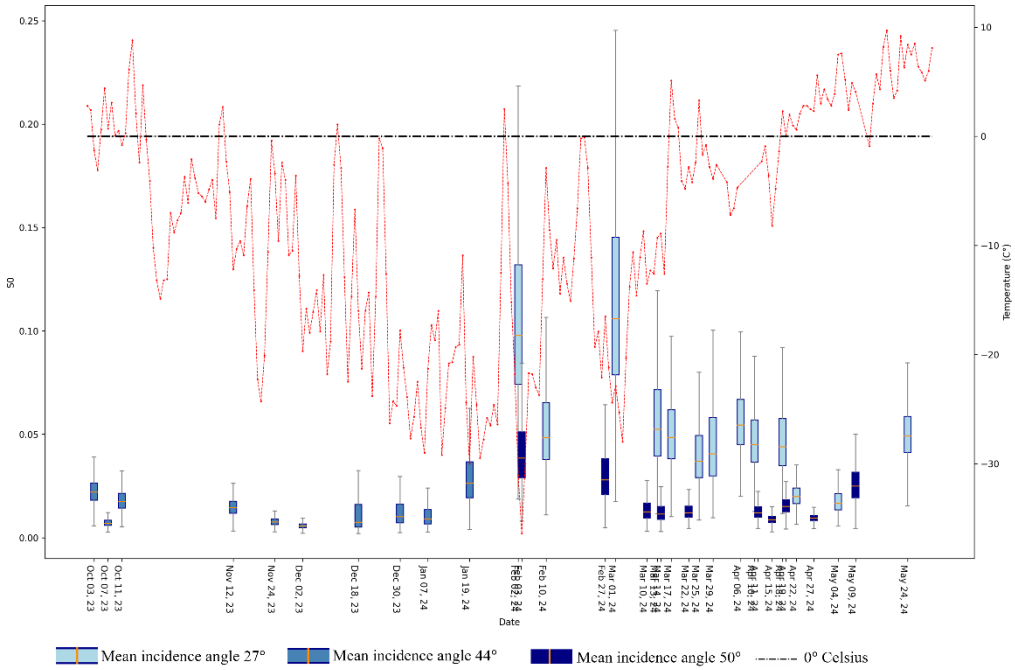


Figure 56. Whisker Plot of Stoke Parameter S0 at Study Site 2, Kluane Lake, from October 2023 to May 2024.

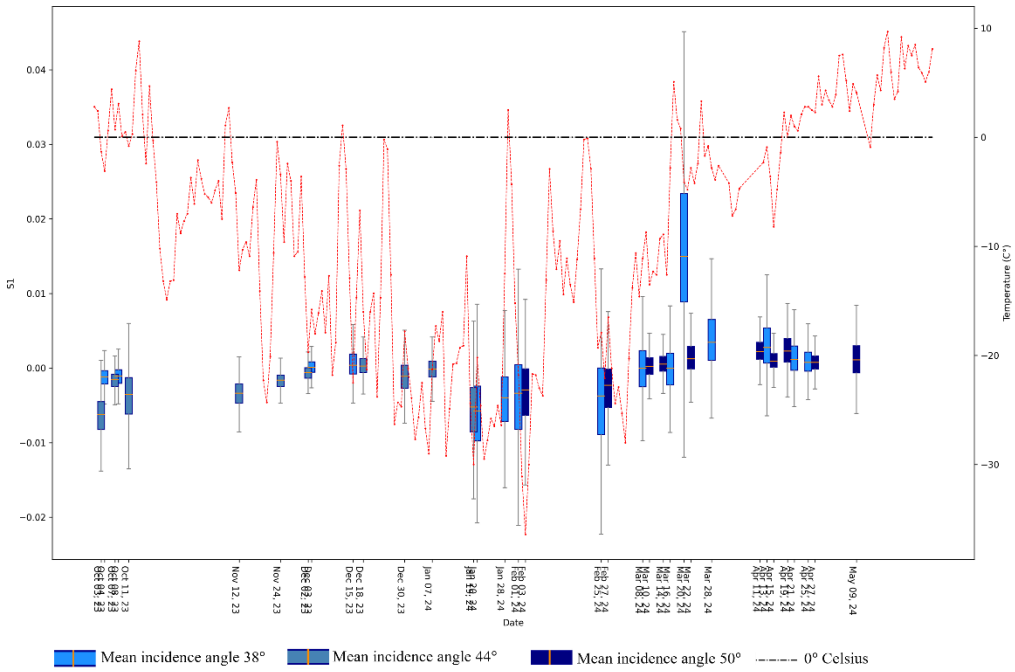


Figure 57. Whisker Plot of Stoke Parameter S1 at Study Site 1, Kluane Lake, from October 2023 to May 2024.

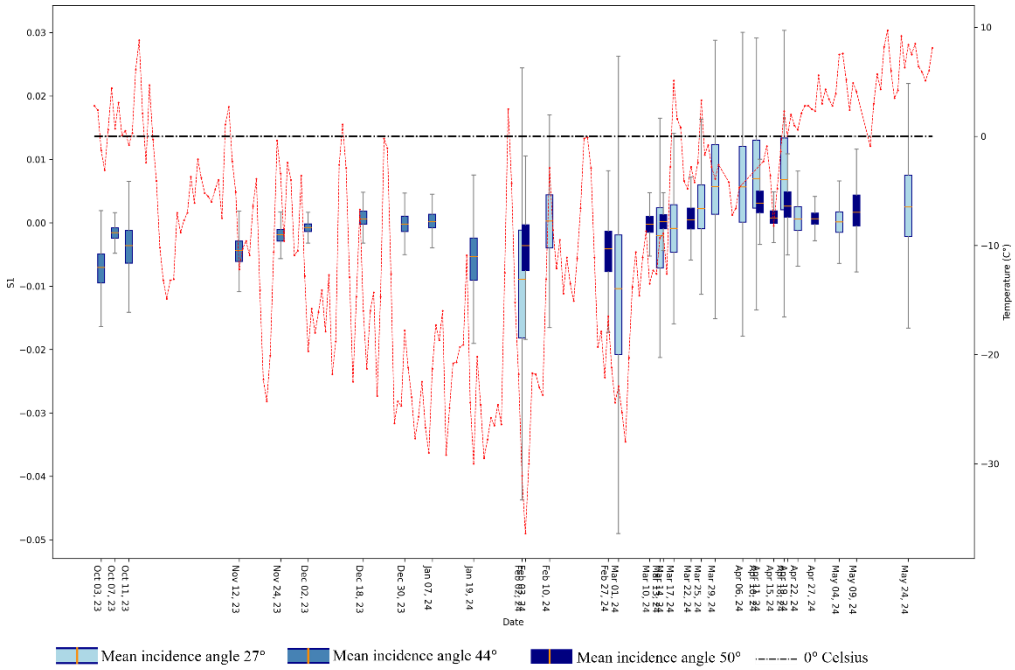


Figure 58. Whisker Plot of Stoke Parameter S1 at Study Site 2, Kluane Lake, from October 2023 to May 2024.

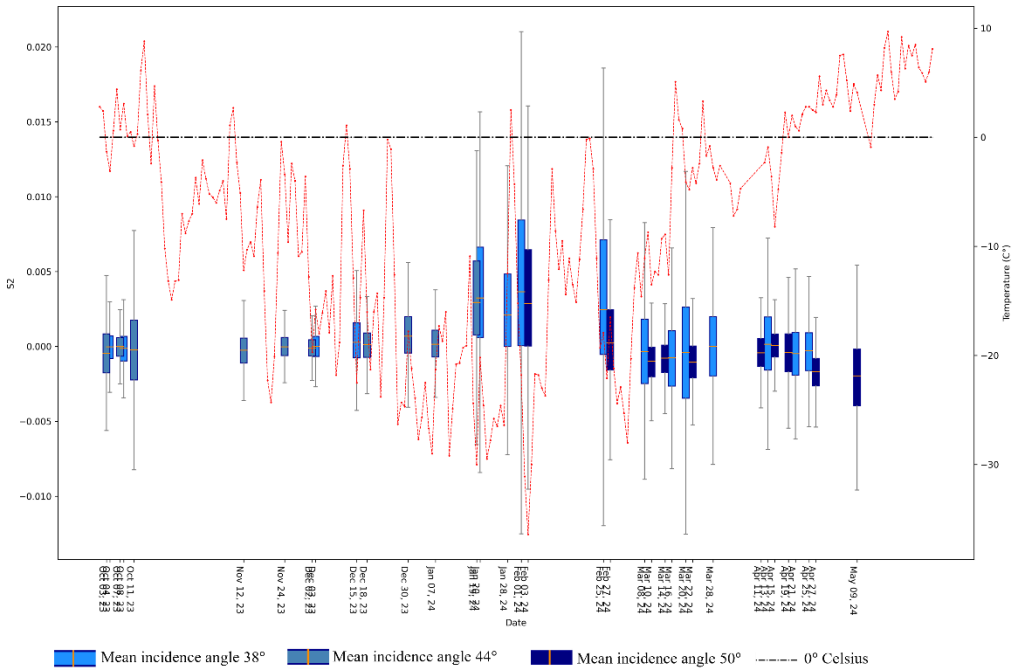


Figure 59. Whisker Plot of Stoke Parameter S2 at Study Site 1, Kluane Lake, from October 2023 to May 2024.

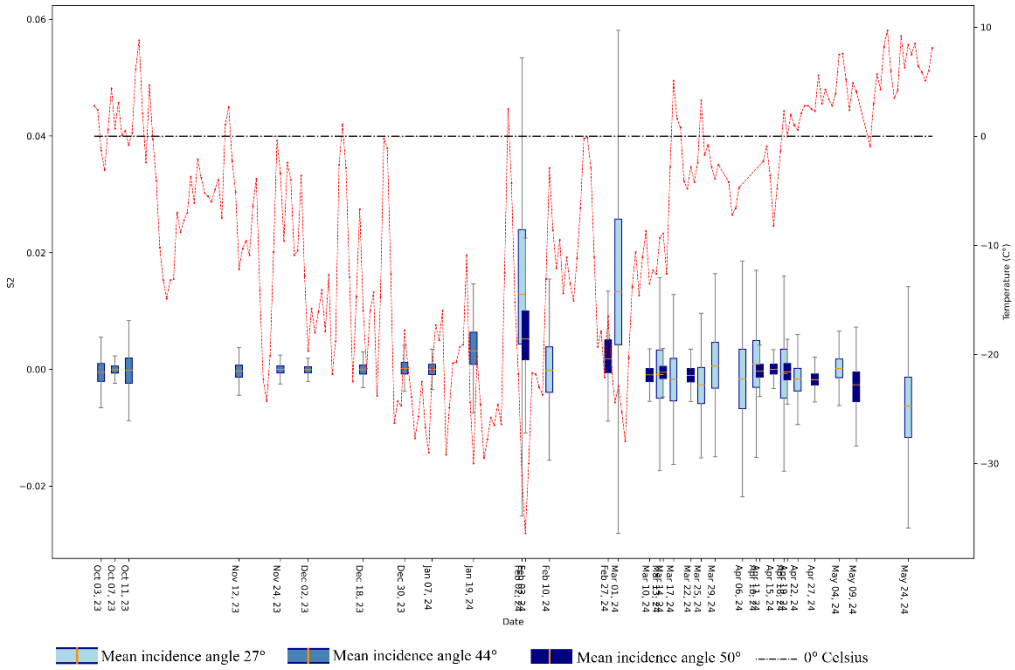


Figure 60. Whisker Plot of Stoke Parameter S2 at Study Site 2, Kluane Lake, from October 2023 to May 2024.

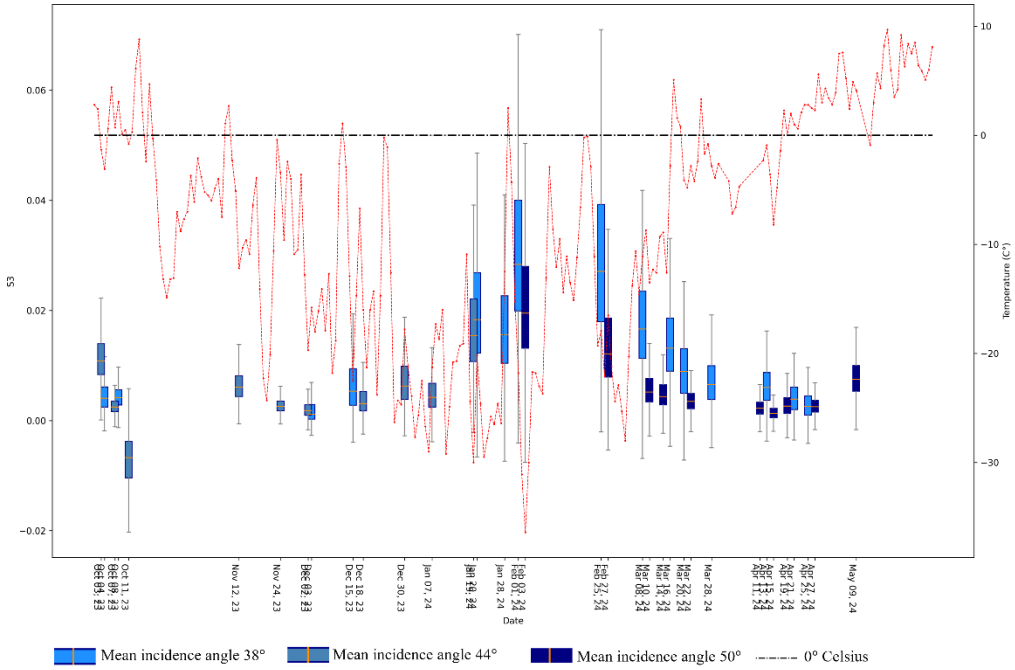


Figure 61. Whisker Plot of Stoke Parameter S3 at Study Site 1, Kluane Lake, from October 2023 to May 2024.

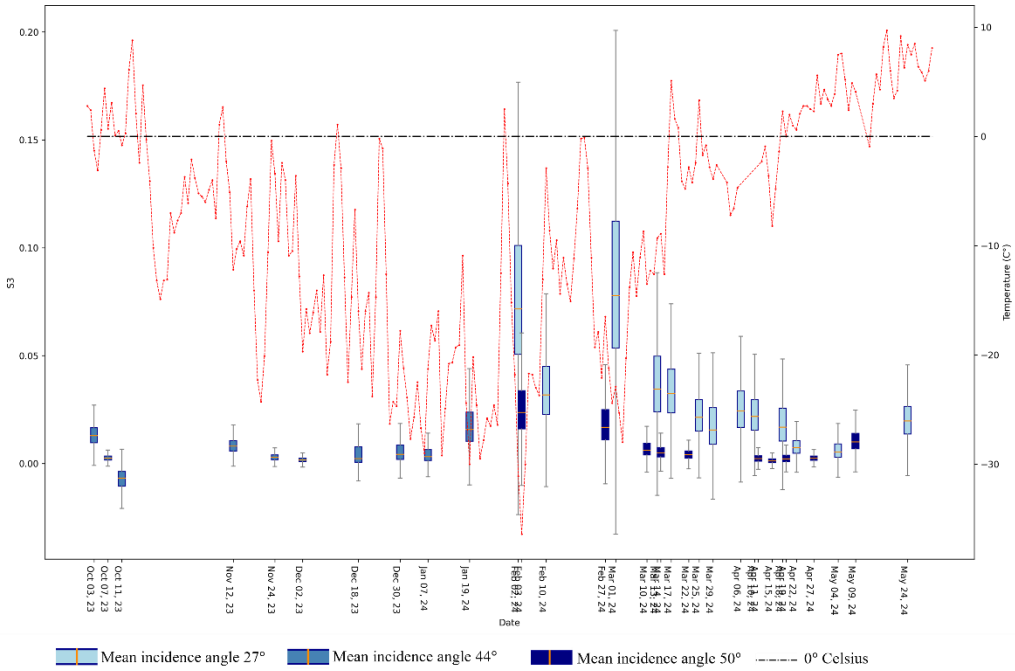


Figure 62. Whisker Plot of Stoke Parameter S3 at Study Site 2, Kluane Lake, from October 2023 to May 2024.